Alma Mater Studiorum - Università di Bologna

DOTTORATO DI RICERCA IN ASTRONOMIA

Ciclo XXI

Settore scientifico di afferenza: Area 02 - Scienze Fisiche

FIS/05 Astronomia e Astrofisica

Laser Guide Star Wavefront Sensors for the EELT

Presentata da: MATTEO LOMBINI

Coordinatore Dottorato   Relatori

Ch.mo Prof. Lauro Moscardini   **Ch.mo Prof. Bruno Marano**

Dott. Emiliano Diolaiti

Esame finale anno 2011

for those I love..

-

Contents

Acknowledgments

Acronyms

AIT	Assembly, Integration and Test
AO	Adaptive Optics
BP	Bi-Prism
BPWS	Bi-Prism Wave Front Sensor
CW	Continuous Wave
DM	Deformable Mirror
EELT	European Extremely Large Telescope
ESO	European Southern Observatory
FA	Focal Aperture
FoV	Field Of View
FP7	Framework Programme 7
FS	Field Stop
FWHM	Full Width Half Maximum
GS	Guide Star
IDL	Interactive Data Language
LA	Lenslet Array
LBT	Large Binocular Telescope
LINC	LBT INterferometric Camera
LGS	Laser Guide Star
MAD	Multi Conjugate Adaptive Optics Demonstrator
MAORY	Multi-Conjugate Adaptive Optics RelaY
MCAO	Multi-Conjugate Adaptive Optics
MMSE	Minimum Mean Square Error
NCPA	Non Common Path Aberration
NGS	Natural Guide Star
NIRVANA	Near-IR/Visible Adaptive INterferometer for Astronomy
OABo	Osservatorio Astronomico di Bologna
OAPd	Osservatorio Astronomico di Padova
ONERA	Office National d'Etudes et de Recherches Aerospatiales

OPD	Optical Path Difference
PoV	Point of View
PS	Pupil Stop
PSD	Power Spectral Density
PSF	Point Spread Function
PWS	Pyramid Wave Front Sensor
QE	Quantum Efficiency
RMS	Root Mean Square
RWFS	Reference Wave Front Sensor
RTC	Real Time Computer
SH	Shack-Hartmann
SLM	Spatial Light Modulator
TMT	Thirty Meter Telescope
TT	Tip-Tilt
UniBo	Università degli Studi di Bologna
VLT	Very Large Telescope
WCoG	Weighted Center of Gravity
WF	Wave Front
WFE	Wave Front Error
WFS	Wave Front Sensor

Introduction

Without the atmosphere, the angular resolution of a telescope, in the visible and NIR bands, is set by the diffraction and increases linearly with the diameter D_{tel} of the telescope, while the atmospheric turbulence limits the angular resolution to never be higher of ∼1arcsec, depending on the site, whatever the telescope diameter is. Besides the capability to detect faint sources is significantly reduced by the turbulence because the PSF is spread over constant angular area and the SNR of a point-source grows only with D_{tel} instead of D_{tel}^2 (Hardy, 1998).

The idea of AO is to use a GS to measure the WF distortion of the astronomical objects light by means of a WFS and to compensate it with a DM placed in the optical path before the science Detector. This has to be done in real time since the shape of the DM has to be adjusted several hundred times per second to track the rapid evolution of the atmosphere. All the big observatories around the world have AO systems that, in the case that a suitable guide star is located close to the interesting scientific targets, deliver diffraction limited images for $\lambda > 1\mu$m, since at longer wavelengths the correction is more effective.

The idea of AO was first proposed in the 1950s (Babcock, 1953), but it was not until the early 1990s that technology was advanced enough to actually build an AO system for astronomy, using a single NGS. A major limitation of these systems is that the science object has to be very close to the NGS, because the correction performance drops rapidly with the angular separation. The corrected area can be increased by the MCAO (Dicke 1975 and Beckers 1988), where several GSs are used to measure the WF in different directions. The distortion from the individual turbulent layers can be isolated and, by placing multiple DMs optically conjugated to the same altitude of these layers, the distortions induced by entire layers can be corrected over the whole FoV. The diameter of the area with useful correction can be increased up to about 2arcmin. Anyway the number of enough bright NGSs for AO is limited and

the sky coverage, that is the fraction of the sky that can be observed taking advantage of the AO correction of the turbulence, is quite low.

A relevant increase to the sky coverage can come from the creation of an artificial GS close to the science object, by projecting a powerful laser onto the sky (Foy & Labeyrie, 1985). At least one NGS is still required to measure the global TT over the telescope aperture, but it can be much fainter and farther away from the science object. The LGSs require lasers with the specific wavelength of 589nm, expensive and difficult to operate. Moreover some issues complicate the LGS WF sensing respect to the NGS one, but the AO performance in terms of correction quality and sky coverage has driven the development of LGS AO systems that at the moment are almost routinely used, for example, at Keck, Gemini North and South telescopes and VLT.

In view of the construction of the EELT the LGSs have become a key aspect related to the science requirement for diffraction limit images over a big fraction of the sky (EELT science cases). Unfortunately some features of the Sodium layer where the LGS are formed have a much bigger impact on the performance of the WFSs for the EELT respect to the 10m class telescopes and they still have to be evaluated in detail.

For the baseline SHWS the current size of the Detectors, with a fast reading rate and low RON, and the return flux from the LGSs do not fulfill the requirements in terms of residual WFE. The time instability of the Sodium layer density and its vertical extension reduce the centroiding algorithms performance and cause some NCPA requiring additional control loops. Accurate studies, by means of analytical and numerical simulations, are being carrying out to mitigate the technological requirements and analyze the contribution of each error source.

The idea of the development of an LGS Prototype, presented in this Thesis, was born in the framework of the Phase A study of the MCAO module for the EELT, MAORY(Diolaiti et al., 2010), lead by OABo. I am part of the group that worked for this project. We proposed the construction of a laboratory Prototype to investigate the LGS WF sensing issues, particularly addressed to the SHWS case. To complete and validate the simulations it was decided to reproduce in the laboratory a SHWS using an extended reference source with the expected LGS features in the EELT case. The intent was to carry out tests with real images to be compared to the simulations that influence the design

and quantify the performance of the LGS WFSs.

The goal of this Thesis is to present a detailed description of the LGS Prototype development, started at the beginning of 2008 and carried out during all my PhD period.

In the first chapter we make a brief introduction of AO and show how the lack of bright NGSs requires the use of LGSs, especially in view of the construction of the EELT.

In chapter 2 we give a short overview of the LGSs, describing the WF sensing issues related to these artificial stars. We expose also two different alternative WFSs, respect to the baseline SHWS, we are investigating. The aim of these studies is to provide more relaxed requirements from the WFSs, especially regarding the Detector size and the laser power. Finally we describe the LGS WF sensing strategy turned out after MAORY phase A study, linking the critical aspects to the LGS features that the Prototype had to simulate.

Chapter 3 contains a complete description of all the phases of the LGS Prototype development, from the conceptual design, through the opto-mechanical design, the AIT, to the tests on the centroiding algorithm performance carried out after its integration. At the end of this chapter some possible upgrades of the opto-mechanics, to improve the Prototype functionalities, are described.

Chapter 1

Adaptive Optics

The turbulence in the atmosphere is the result of mixing of air at different temperatures, which is caused by solar heating during the day. Having a mix of temperatures, the air density is constantly changing in a random fashion, which in turn produces a change in the index of refraction of the air atmosphere, producing degradation in the resolution of the image. The atmospheric turbulence, located mostly in the first 20km of altitude above the ground, distorts the plane WF of the astronomical objects and does not permit the telescope to deliver images with an angular resolution, defined as the minimum angular distance over which two point size objects are distinguished, proportional to its aperture diameter. The turbulence is a stochastic process, so a statistical approach to study its properties is required.

The first model of the WF aberrations induced by the turbulent atmosphere was proposed by Kolmogorov (Tatarski, 1961). This model and all the subsequent ones are function of the refractive index structure function C_N^2, which is a measure of the turbulence strength at different altitudes and depends basically on the quote above the ground (see ad example the Paranal seeing data at Paranal seeing data). Without turbulence, a point size source would be imaged on a Detector as a sharp image with a dimension given by the diffraction limit, while for ground based observations a short exposure image is formed by many speckles having each the dimension of the diffraction limit images and evolving rapidly (figure 1.1 left). The Fried Parameter r_0 is usually used to describe the characteristic spatial extent of the wavefront aberrations and it can be calculated by (Fried, 1965)

$$r_0 = \left[0.423 \left(\frac{2\pi}{\lambda} \right)^2 sec\xi \int C_N^2(h)dh \right]^{-3/5} \tag{1.1}$$
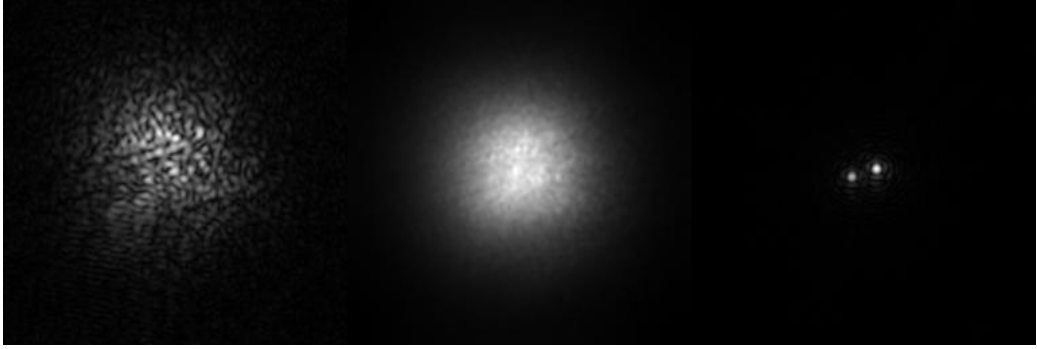
Figure 1.1: Illustrative comparison of the angular resolution of a telescope with a short (left) and long exposure image (middle) in the presence of atmospheric turbulence. At the right a diffraction-limited image shows the presence of two point sources that were below the resolution allowed by the seeing.

where λ is the wavelength, C_n^2 depends on the turbulent layer altitude h and ξ is the Zenith angle. With this definition, r_0 is roughly the diameter of an area within which the variance σ^2 of the WF aberrations is 1 rad^2 (Noll, 1976) and is the characteristic sampling dimension of the aberrated WF over the telescope aperture.

The characteristic time scale for the changes in the WF aberrations is defined as the WF coherence time τ_0, that describes the time after which the variance of the change in the WF amounts to 1 rad^2. Its formula can be written as

$$\tau_0 = 0.057 \left[\lambda^{-2} sec\xi \int C_N^2(h) v_w(h)^{5/3} dh \right]^{-3/5} \tag{1.2}$$

where v_w is the wind velocity at the layer altitude h.

From eq. 1.2 and 1.1 it can be noted that at longer wavelength τ_0 and r_0 increase. A typical value for τ_0 is $\sim$ few milliseconds, for r_0 is $\sim$ 0.1m in the visible Band (central λ=0.5μm) and 0.5m in K-Band (central λ=2.2μm)). If we consider as long exposure an integration time is $\gg$ of τ_0, a long exposure uncorrected image will have the angular dimension $\propto \lambda/r_0$, the well known seeing disk (figure 1.1middle), that represent the limit angular resolution for any telescope with a diameter bigger than r_0 without AO correction.

1.1   Adaptive Optics scheme

The goal of AO is to deliver diffraction limited images (figure 1.1right) to the science instrument by measuring and correcting the aberrated WF at the timescale given by τ_0 and with the resolution set by r_0. The instruments that
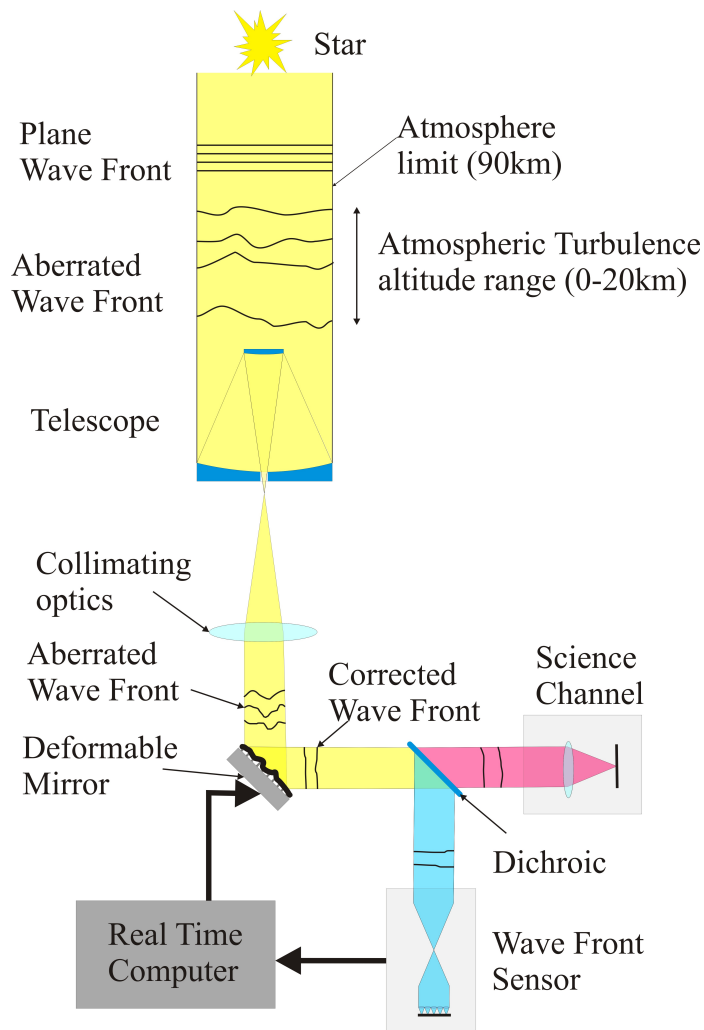
Figure 1.2: Explanation of the AO operating scheme

benefit of the AO correction are usually in the NIR band where it is easier to track the turbulence variation and the pupil has to be sampled by less sub-apertures.

In figure 1.2 the scheme of an close loop AO system is presented. The distorted beam of a GS coming from the telescope is collimated onto a DM placed on the pupil plane image. The light is folded by the DM toward the dichroic where the shorter wavelength light is directed to the WFS while the longer wavelength beam is imaged by the scientific Detector. Usually the light split by the dichroic is at $\lambda \sim 1\mu$m. The WFS measures the shape of the WF so that the RTC can compute the correction to be applied to the incoming beam by means of the DM. The presented AO scheme operates in closed loop since

the WFS measures the residual WF after the correction of the previous cycle, permitting the convergence and the stability of the adaptive correction also in case of non perfect knowledge of all the system characteristics.

1.1.1   Wavefront errors

An AO system can never completely compensate the WF distortions induced by the atmosphere because some residual aberrations will be always present. The residual WF variance σ_{tot}^2 can be divided into several components σ_i^2, according to their respective origins, that are then summed in quadrature since they are considered as independent error sources:

$$\sigma_{tot}^2 = \sum \sigma_i^2 \tag{1.3}$$

The quality of an aberrated imaging system is usually measured by the SR. This quantity is defined as the on-axis intensity in the image of a point source divided by the on-axis intensity of the diffraction limited image taken through the same aperture. For a circular aperture with an aberration function $\phi(\rho, \theta)$, which describes the wavefront distortion as a function of the spherical coordinates (ρ, θ), the SR is given by:

$$S = \frac{1}{\pi^2} \left| \int_0^1 \int_0^{2\pi} \rho \, d\rho \, d\theta \, e^{ik\phi(\rho,\theta)} \right|^2 \tag{1.4}$$

From this equation it is clear that $0 \leq S \leq 1$, S=1 for $\phi = $ constant, S$\ll$1 for strongly varying ϕ. For any given (varying) ϕ the Strehl ratio tends to be higher for longer wavelengths (since $k = 2\pi/\lambda$). If the WF aberrations are not exactly known, using the residual WF variance σ_{tot}^2 the Strehl ratio can be approximated by (Marechal, Born et al., 1999)

$$SR \approx e^{-\sigma_{tot}^2} \tag{1.5}$$

valid when σ_{tot}^2 is smaller than $\sim 2 \; rad^2$ (thus the SR being higher than 15%). In the design of any AO system the Error Budget represents the achievable WFE during the correction loop, decomposed in all the predictable error sources, plus a term of contingency. For each error term there is an allocation with its estimated, or maximum allowed, WFE. Some error sources are quite easily to be calculated during the design phase, as for example the fitting error, that depends on the spacing of the DM actuators or the aberrations caused by the optics.   Other terms can vary between different AO runs

since they depends on the temporary atmospheric conditions and their WFE allocations are calculated for typical site conditions. The WFE related to the GS magnitude drives the sky coverage, which is the fraction of the sky over which the residual WFE is too high respect the AO correction performance required by the scientific instruments.

1.1.2 Wavefront measurement
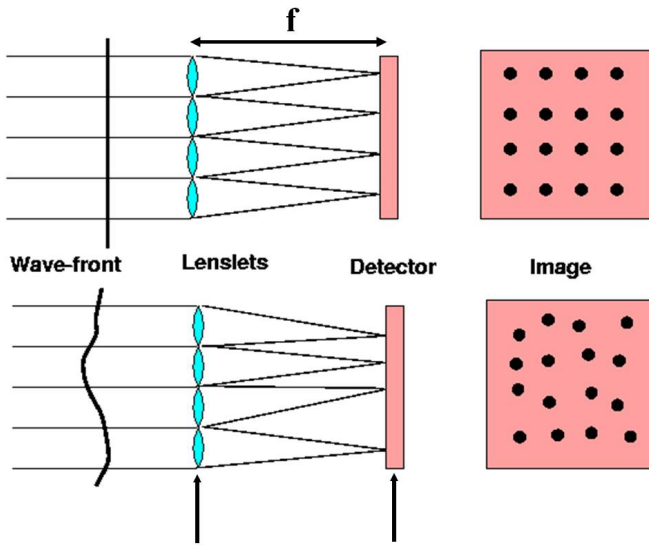
Figure 1.3: Schematic view of SHWS

The SHWS (Shack & Platt (1971), based on a device devised in 1900 by J.Hartmann) is the most diffuse WFS for AO applications. Moreover it appears to be a conservative and reliable choice in case of elongated sources as the LGSs, described in chapter 2, even if some issues related to the Detector size and the photon flux for the EELT case are still under study (section 2.4). The SHWS is the baseline WFS for MAORY (section 1.2.1) and also for the LGS Prototype presented in this thesis. The SHWS is an array of identical (square or hexagonal) lenses, the LA, followed by the Detector in the focal plane of the lenses (figure 1.3). It is placed on a pupil plane, so it measures the same WF arriving to the telescope aperture, possibly degraded by the aberrations produced by the optics that can be characterized during the calibration phase. The size of the lenses of the LA is related the turbulence coherence length r_0 (eq 1.1) of the observing wavelength in the science channel. The telescope

aperture would have the sub-apertures size equal to r_0 if sampled with the same number of sub-apertures. Each lens forms an image of the GS on the Detector. When an incoming WF is plane, all images are located in a regular grid defined by the LA geometry. As soon as the WF is distorted, the images become displaced from their nominal positions and the shifts of the image centroids in two orthogonal directions are proportional to the local average WF slopes over the sub-apertures. The WF is reconstructed from the arrays of measured slopes, up to a constant which is of no importance for imaging. The SHWS measurement noise, calculated in terms of variance per axis, can be derived from the formulas presented below (Rousset, 1999) including the photon, Detector and background noise:

$$\sigma_{ph}^2 = \frac{\pi^2}{2} \frac{1}{n_{ph}} \left(\frac{N_t}{N_d} \right)^2$$

$$\sigma_{RON}^2 = \frac{\pi^2}{3} \frac{\sigma_e^2}{n_{ph}^2} \frac{N_s^4}{N_d^2}$$

$$\sigma_{bkg}^2 = \frac{4\pi^2}{3} \frac{n_{bkg}}{n_{ph}^2} \left(\frac{N_t}{N_d} \right)^2 \tag{1.6}$$

In the above formulas n_{ph} is the number of received photons per sub-aperture per integration time, n_{bkg} the number of background photons over the image, N_t the image FWHM, N_d the sub-aperture diffraction limit FWHM, N_s the number of pixels over the image and σ_e the RON. The terms of eq. 1.6 are then summed and multiplied by $\sqrt{2}$ to retrieve the total OPD error variance. It is evident that n_{ph} has a big impact on the SHWS measurement noise and sets the limiting magnitude of the GS, on the basis of WFE allocation in the Error Budget. For instance, the Keck NGS AO systems requires the GS must be brighter than 14th magnitude and within 30arcsec from the science target (Wizinowich et al., 2006) and similar values are requested also for Gemini North Altair (Gemini website). Of course the spectral type of the star influences its magnitude at a given wavelength.

1.1.3   MCAO

Since the astronomical objects under scientific investigation are often too faint to allow WF sensing by means of their own beam, a sufficiently bright star is needed as GS for the AO correction. The GS has to be close enough to the scientific target in order to measure on its beam as much as possible the WF
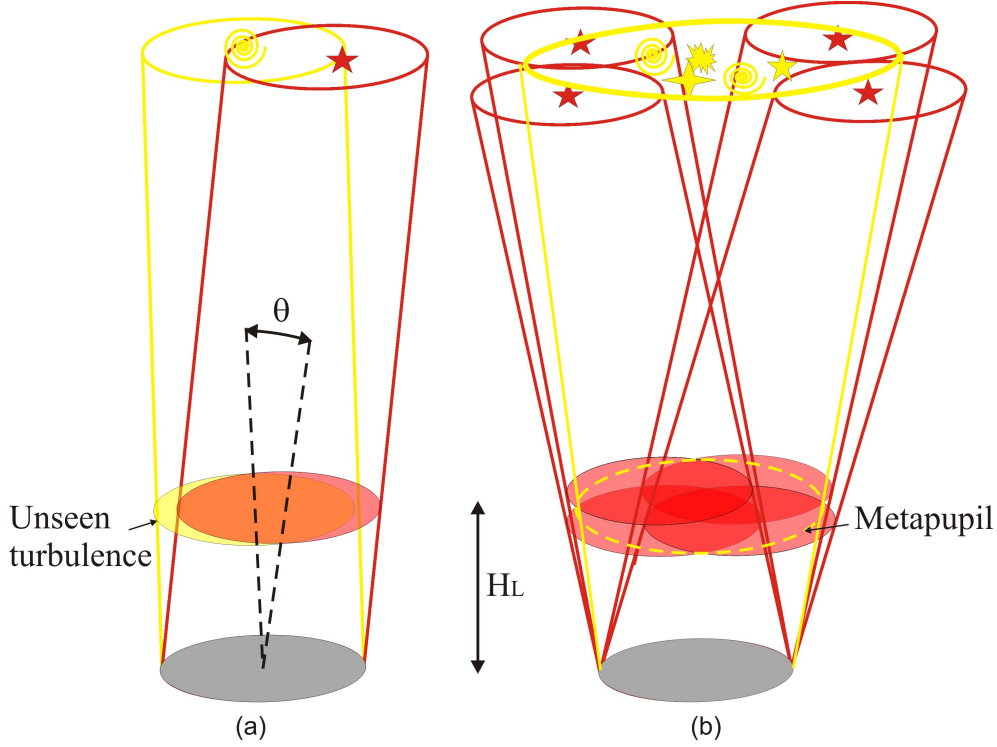
Figure 1.4: a: angular anisoplanatism. The WF measured along the direction of the GS causes the correction to be poorer increasing the separation angle θ between the GS and the science object since at the altitude H_L of a turbulent layer there are unseen regions of turbulence that are not measured and consequently corrected; b: MCAO solution to the angular anisoplanatism. At the altitude H_L several GSs achieve a better coverage of the metapupil, the region at a given altitude inside the FoV of scientific field.

perturbations of the scientific target beam (fig. 1.4a). As the angular distance θ between the GS and the science object increases the correction performance by the AO system degrades rapidly. To characterize the FoV with useful correction, the isoplanatic angle θ_0 is defined (Hardy, 1998)

$$\theta_0 = 0.057\lambda^{6/5} \left(sec\xi \int C_n^2(h)h^{5/3}dh \right)^{-3/5} \tag{1.7}$$

With this definition, θ_0 is the angular separation at which the variance between the wavefront of the GS and of the science object is 1 rad^2. Typical values for θ_0 in the K-Band are $\sim$20 arcsec. For a single-star AO system and an off-axis science object, an additional error source, the isoplanatic error, due to the small value of θ_0 has thus to be considered.

A possibility to increase the size of the corrected area is by using several GSs to measure the turbulence in the complete 3D volume above the telescope

(fig. 1.4b). In MCAO systems (Dicke 1975, Beckers 1988) the turbulence is corrected by multiple DMs which are optically conjugated to the altitude of the most turbulent layers. The correction is much more uniform over a significantly increased FOV (Ragazzoni et al. 2000, Rigaut et al. 2000, Ellerbroek & Rigaut 2001, Diolaiti et al. 2001).

The so called Star Oriented MCAO requires a WFS for each GS and combines the information from the single WFSs numerically, to retrieve the vertical structure of the turbulence and apply the appropriate commands for controlling the DM conjugated to a given layer. This approach is thus also called atmospheric tomography. The advantages of this concept is that established WFS techniques can be used, and with the help of sophisticated wavefront reconstruction algorithms, an optimal performance in the direction of the science object can be achieved (Fusco et al., 1999).

The Layer Oriented MCAO (Ragazzoni et al., 2000) requires a WFS for each DM instead of a WFS for each GS as for the Star Oriented approach. Each WFS can receive the light by several GSs whose signal is optically co-added, using a focal plane WFS as the Pyramid WFS (Ragazzoni, 1996). In this way also fainter GSs can be used, even though GSs with different brightness cause a the correction not uniform over the FoV, but rather biased towards the brighter sources.

1.2   Adaptive Optics in the EELT epoch

AO technique demonstrated to work on the sky and all the major observatories around the world have built AO modules. In figure 1.5 two images of the same stellar field in the K-Band are compared. The left figure was obtained by the seeing limited imager ISAAC (Cuby et al., 2000) while the right one could benefit of the AO correction produced by the Star Oriented mode of MCAO Demonstrator of ESO (Marchetti et al., 2008). The improvement in the angular resolution and the uniformity of the adaptive correction appears rather clear in this figure.

    As explained in section 1.1.2, there is a limit magnitude of the GS beyond which the measurement noise of the SHWS becomes too high. In the Layer Oriented approach the optical co-add of the GS light permits an increment in the limit magnitude even if fainter GSs give a small contribute in the WF

(a)   (b)
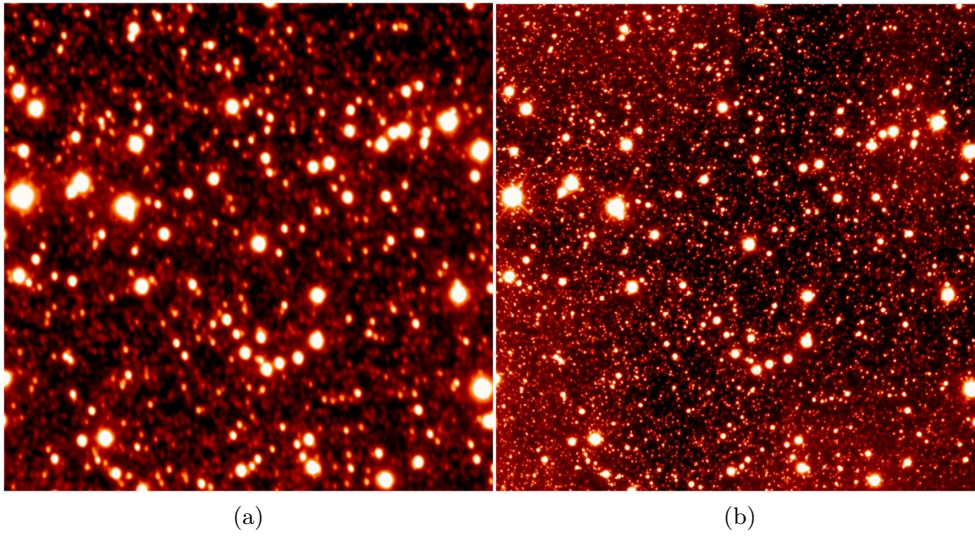
Figure 1.5: OmegaCen observed at the VLT in seeing limited (ISAAC) and diffraction limited (MAD) modes (K-Band).

sensing performance. The sky coverage, especially in the case of multiple references, is complicated to be evaluated in detail since also the GS asterism geometry has an impact on the performance. The results of the simulations (for example Fusco et al. 2006, Bello et al. 2003) can be sightly different but anyway they all agree to agree on few percent sky coverage with NGSs at high Galactic latitudes.

In the current telescopes the choice of the adaptive correction of the images is an option that can be chosen if the desired scientific targets are close to suitable NGSs. For the EELT this will not be the case anymore. As explained in section 1.1.2 the dimension of the sub-apertures in a WFS depend on the Fried parameter r_0 associated to the science instrument observing wavelength and it is independent on the telescope diameter. This means that for the EELT the GSs limit magnitude and thus the sky coverage do not rise. Because of its big structure the EELT will require anyway an active correction only to maintain the intrinsic optical quality of the telescope. The primary mirror is not monolithic but will be highly segmented and aspherical, composed by 984 segments of 1.22m side. The segments misalignment introduces local piston, tip and tilt signal that must be compensated, even though with a lower correction velocity than AO (Mazzoleni et al., 2008). Moreover a quite fast bandwidth is expected to stabilize the image, due to the structure vibration caused the wind

shake, of the order of few hundred hertz (Vernet et al., 2008). Finally the AO correction of the turbulence is necessary to exploit the angular resolution of a 42m telescope (5mas in the J-Band) or really benefit of the enormous collecting area, since without AO the SNR of faint sources grows with D_{tel} and with the correction with D_{tel}^2. The EELT can be considered as an adaptive telescope since two DMs (M4 and M5) will provide the correction of the GL turbulence. ESO launched in 2008 preparatory studies for 9 instruments and 2 post focal AO modules. All instruments but 2 require AO correction as mandatory for the scientific goals (EELT instrumentation website). The necessity to be able to make observations over a relevant fraction of the sky requires a solution to increase the sky coverage delivered by the NGSs that can be found using the LGSs that will be introduced in the next chapter.
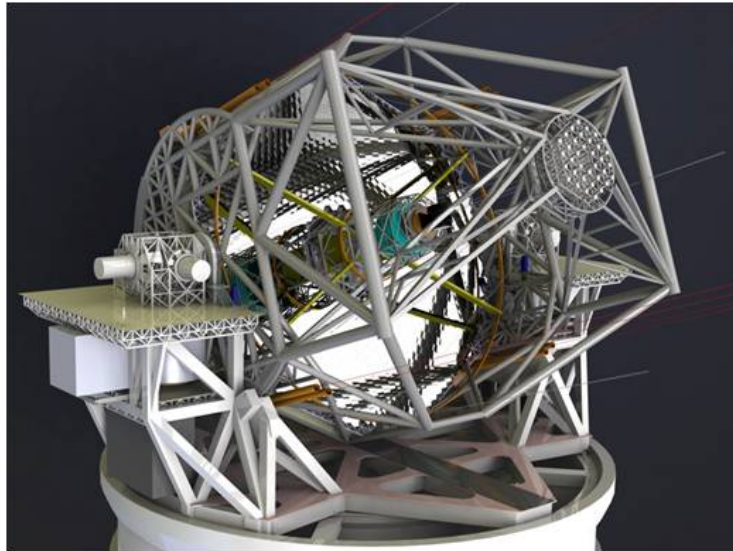
Figure 1.6: Pictorial view of the EELT (credits ESO).

1.2.1   MAORY

A specific example explaining the necessity to use the LGSs, due to sky coverage requirements, is MAORY (Diolaiti et al., 2010), the foreseen MCAO module for the EELT. MAORY Phase A study was carried out by a Consortium led by the OABo, including the Astronomy department of UniBo, OAPd, ONERA and sponsored by ESO. Its optical design is shown in figure 1.7. MAORY is requested to provide two different corrected FoV: a medium diameter (20"-1') and a large FoV diameter, up to 2arcmin. The correction
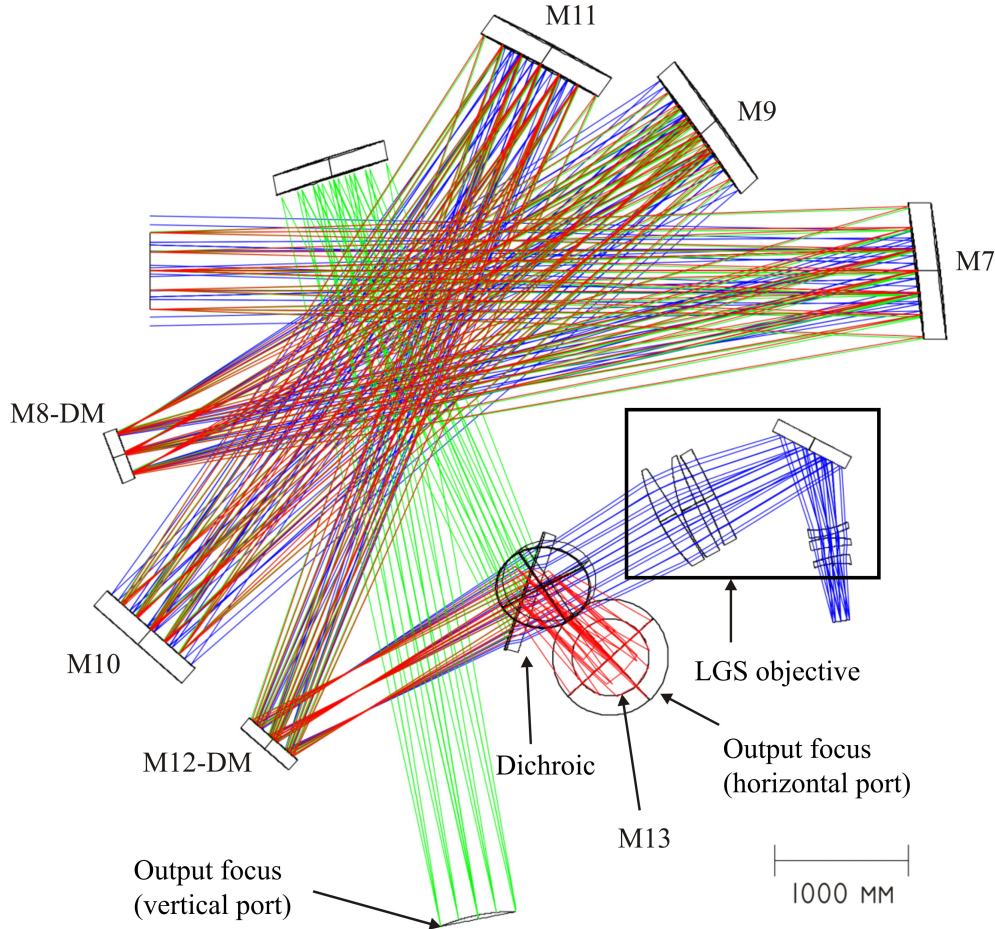
Figure 1.7: Top view of the MAORY. The optical bench is located on the EELT Nasmyth platform on one of the bent foci. MAORY is a finite conjugate relay formed by two pairs of aspheric off-axis mirror. Flat fold mirrors (two of which, M8 and M12, are deformable) allow to fit the reserved area on the Nasmyth platform. The optical relay makes an image of the telescope focal plane with unit magnification and maintain the same exit pupil location as the telescope direct focus.

quality and uniformity is expected to be high in the medium field, moderate in the large field. The EELT high angular resolution camera MICADO (Davies et al., 2010) is a candidate client instrument of MAORY and requires an image correction of high quality and uniformity to perform high accurate photometry and astrometry while a candidate science instrument that might be served on a second output port is the single field near-infrared spectrograph SIMPLE (Origlia et al., 2010), that requires a high energy concentration of the on-axis PSF. High sky coverage is a key requirement common to both science instruments also at the Galactic Pole, where the star density is low. MAORY

expected performances (figure 1.8) and sky coverage (table 1.8) can not be achieved by means of the NGSs as pointed out in section 2.2. MAORY baseline is to use 6 SHWSs and an equal number of LGSs. The WF sensing issues related to these artificial GSs are presented in the next chapter, while MAORY strategy to deal with these issues is illustrated in section 2.4.
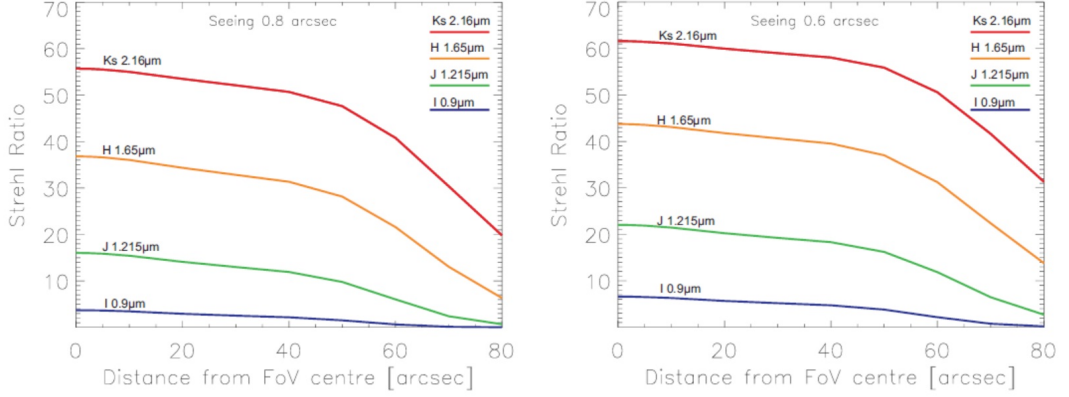
Figure 1.8: The Strehl Ratio value as function of the off-axis for two different seeing values. For each seeing value, the different lines show the radial profile in the 5 bands considered.

Minimum field-averaged Strehl Ratio (seeing 0.8")					Sky coverage
$\lambda=2.16\mu$m (Ks)	$\lambda=1.65\mu$m (H)	$\lambda=1.215\mu$m (J)	$\lambda=1.021\mu$m (Y)	$\lambda=0.9~\mu$m (I)	
0.54	0.34	0.14	0.06	0.03	39%
0.42	0.22	0.06	0.02	>0.01	80%

Table 1.1: Expected performance and corresponding sky coverage at the Galactic Pole. The minimum Strehl Ratio expected for each percentage of sky is shown. The Strehl ratio is averaged over the FoV of MICADO (53"x53"). The NGS WFS probes are assumed to be positioned in order not to obscure the client instrument FoV.

Chapter 2

Laser Guide Stars

In order to increase the low sky coverage of the NGS AO (section 1.1.3), an artificial star close to the scientific targets of interest can be switched on by means of a collimated laser beam, tuned at the D_2 lines ($\lambda \sim$589.2nm) and projected toward the sky (Foy & Labeyrie, 1985). At about 90 km of altitude there is a layer of atomic Sodium, deposited by the in-fall of micro-meteorites and removed from below by chemical reactions (Herriot et al., 2006). The Sodium atoms of the layer are excited and re-emit photons with the same wavelength of the laser. Since the global TT signal over the telescope aperture can not be retrieved from the LGSs, the explanation is given in section 2.1.1), one or more NGSs are still needed. Anyway their required magnitude is considerably higher respect to the case of the pure NGS WFS, permitting a significant increase of the sky coverage (section 2.2). Hereafter the acronym LGS will refer to the GSs formed in the Sodium layer, even though some AO modules on 6-8m class telescopes make use of another class of artificial stars, the Rayleigh LGSs (Benn et al. 2008, Thompson et al. 2009), that exploit the elastic scatter of the atoms and molecules in the lower atmosphere (Fugate et al., 1991). The scatter occurs in a broad band of wavelengths and thus it is also easier to retrieve powerful lasers from a different industrial uses, as for example the metal cutting processes. Unfortunately this WFS technique presents strong limitations for an application to big telescopes as the EELT, due to its big cone effect, explained in section 2.1.2.

The particular wavelength required by the LGSs has not wide industrial utilizes, hence the development of suitable powerful lasers has been carried forward within the astronomical community with the help of external companies. Two different technological approaches for CW lasers (a distinction
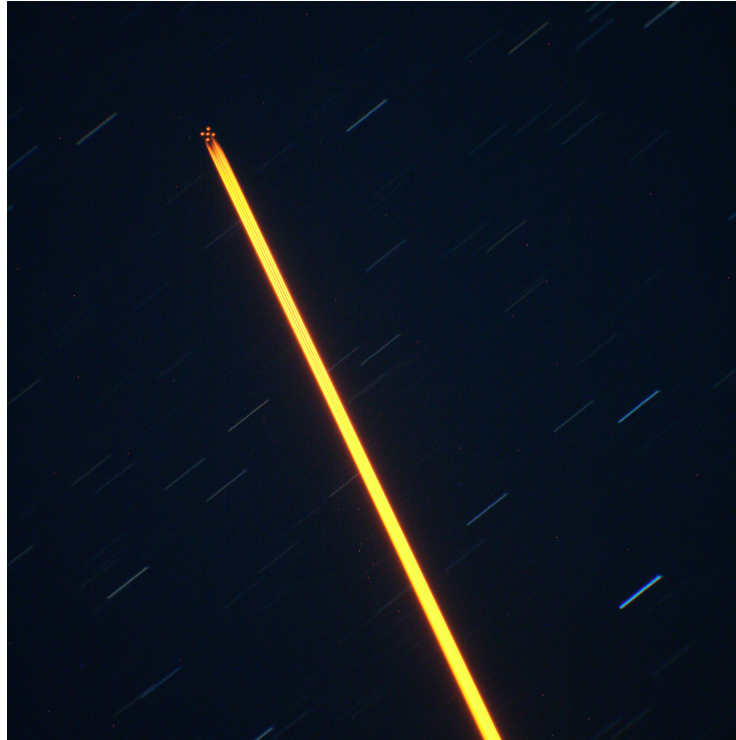
Figure 2.1: First light of the multiple LGS beam at Gemini South with a goal laser power of 60W total (courtesy of Gemini Observatory/AURA).

between CW and pulsed lasers is presented in section 2.3) generation at 589nm are at the moment developed: the sum frequency solid-state laser that combines two IR beams (1064nm and 1319nm) in a non linear crystal so that the inverse of the exit wavelength is the sum of the inverse of the two input wavelengths (λ^{-1}=589^{-1}=1064^{-1}+1319^{-1}). This technology is used, for example, at Keck and at the two Gemini Observatories (Sawruk et al., 2010). First light of the $\sim$50W laser at Gemini South Observatory is shown in fig. 2.1); ESO and Subaru Observatory instead have chosen to develop the technology of lasers at 1178nm, to be frequency doubled to 589nm (Bonaccini et al. 2010, Ito et al. 2010).

The received number of photons from an LGS n_{rec} can be calculated from the following equation:

$$n_{rec} = n_{out} \cdot (1 - p_{Rey}) \cdot p_{Na} \cdot p_{coll} \cdot p_{tras} + n_{bkg} \qquad (2.1)$$

where the number of photons exiting from the launcher n_{out} is multiplied by: the fraction of beam not scattered by the lower atmosphere (1 - p_{Rey}); the fraction of the photons arriving to the Sodium layer that are absorbed and

re-emitted p_{Na}; the fraction of the LGS light that is collected by the telescope p_{coll}; the total transmissivity through the optics and the Detector QE p_{tras}. The number of background photons n_{bkg} is an additive term. Depending on the Sodium density, a 12-14W laser generates an LGS with an equivalent V magnitude of typically 9.5 to 10.5 mag at Zenith, corresponding to $\sim$140 to 55 photons $s^{-1}cm^{-2}$ (Wizinowich et al., 2006).

2.1 LGS WFE sources

The LGSs present various peculiar features that distinguish, and usually complicate, the WF sensing respect to the use of the NGSs. These features are essentially due to the finite distance of the Sodium layer and the temporal variability of its density vertical distribution, causing an increase of the WFE error sources and the requirement for additional control loops.

The benefits of using the LGSs are in the possibility to turn on a bright GS in the desired position and to perform a large and more uniform, respect to the NGS case, correction over the FoV in case of multiple LGSs. We discuss in this section the most significant issues that must be faced when retrieving the WF by the LGSs.

2.1.1 Lower atmosphere effects

For lower atmosphere we mean the altitudes where the turbulence still plays an important role in the WF aberrations. The issues related to the LGSs happen in the upward path of the laser beam.

Fratricide effect

The easiest launching scheme for the LGSs, from the conceptual PoV, is from behind the secondary mirror, as chosen at the Gemini South Observatory (D'Orgeville et al., 2008). Only one launching telescope is needed and there is a common derotation of the LGSs to maintain them fixed respect to the sky (or the pupil). Anyway this launching scheme suffers from the so called 'fratricide effect'. In figure 2.1 the beam lying below the 5 LGSs asterism is produced by the Rayleigh scatter, described at the beginning of this chapter. A SHWS measuring the WF from a given LGS has some sub-apertures that are contaminated by the foreground light of the up going laser beams from
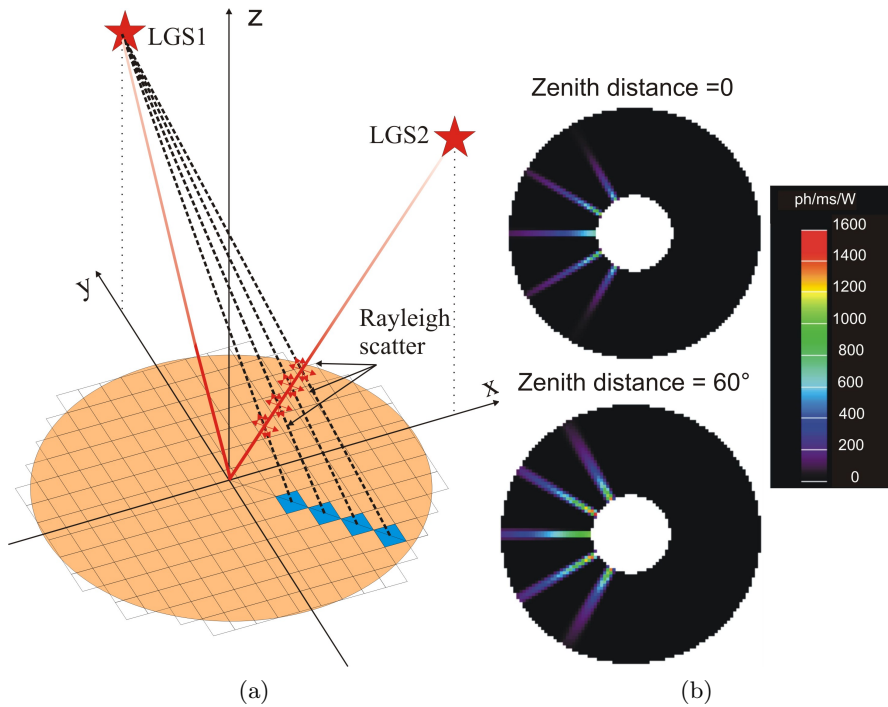
Figure 2.2: a) the sub-apertures of a SHWS related to the LGS1 that have in their FoV the beam of the LGS2 at the low atmospheric heights (blue sub-apertures) receive the Rayleigh scattered light of S2 beam; b) simulation of a SHWS in the case of LGSs launched at 2' FoV. (Courtesy of Enrico Marchetti, ESO).

other LGSs (figure 2.2a). This effect reduces the image SNR in those sub-aperture or can make them completely useless. To overcome to this problem two solutions can be adopted: a range gating with pulsed lasers, by means of the synchronization between the laser pulse and the Detector exposure time to integrate the light of the LGS and cut off the Rayleigh scattered light; place the LGS launchers outside the telescope aperture, avoiding the laser beam to cross the cylinder having the primary mirror as base. Figure 2.2b shows the sub-apertures contamination of a SHWS due to the fratricide effect in case of the launch of 6 LGSs.

TT indetermination and anisoplanatism

At the beginning of this chapter we pointed out that the sky coverage, even with artificial GSs that can be placed everywhere in the sky, is not complete because at least one NGS is required for the laser beacon insensitiveness to the full aperture tilt. The laser beam wanders on both the upward and the
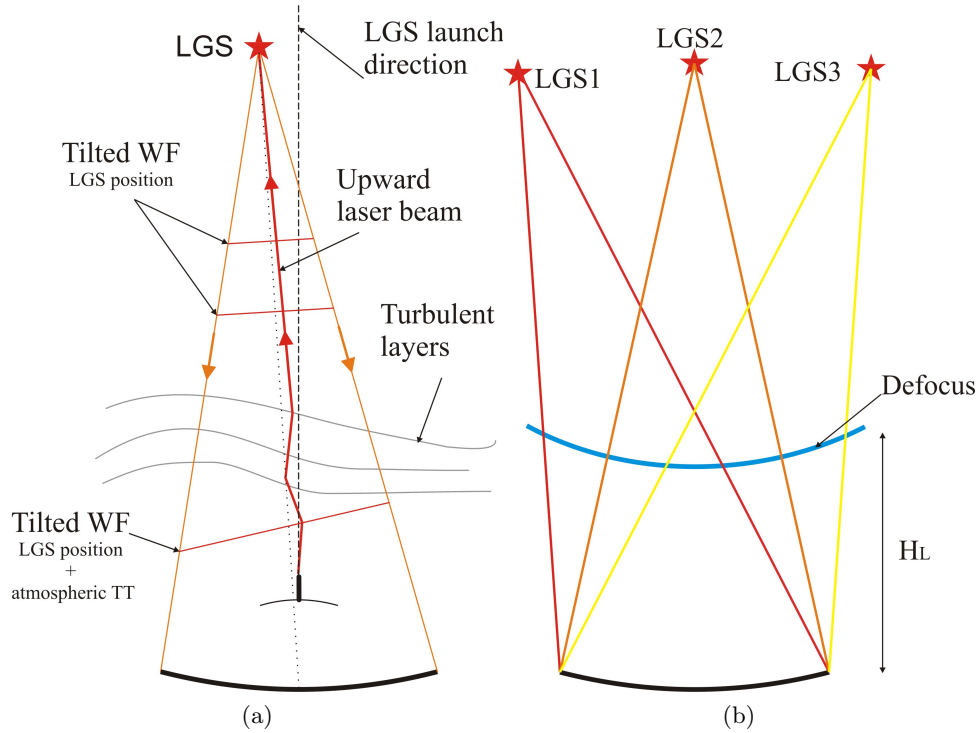
Figure 2.3: a) TT indetermination; b) TT anisoplanatism

downward trips through, at the first order, the same atmospheric turbulence. If the laser was projected by the full telescope aperture no tilt signal would be measured. When the laser is launched by a small telescope at the side of the primary mirror or behind the secondary obstruction, the TT contributions from the LGS actual position and the atmospheric turbulence can not be disentangled (figure 2.3a). It has been proposed (Foy et al., 1995) to produce a multicolor beacon to measure the differential tilt in two wavelengths or to combine Sodium and Rayleigh LGSs tilt informations, but these approaches have never been demonstrated on sky.

The current strategy in the LGS AO systems is the use the NGSs to measure the global TT (Rigaut & Gendron, 1992). Anyway the requested NGS magnitude is much fainter respect the pure NGS WF sensing case, since for the TT measurement it is not necessary to divide the pupil image in sub-apertures (section 1.1.2). The position of the TT NGS degrades the image stabilization performance due to the isokinetic angle, the angle at which the residual phase variance becomes decorrelated by 1 radian^2 due to only the TT, quite bigger anyway than the isoplanatic angle presented in eq. 1.7.

For MCAO at least 3 TT NGSs are required because of the TT anisoplanatism. Looking at figure 2.3b the Defocus term of a turbulent layer at the altitude H_L is measured with the same intensity from all the LGSs. The TT signal is the only way to discriminate the altitude of the layer producing the defocus (and the other quadratic modes). Due to the TT indetermination this information can not be retrieved by the LGSs (Rigaut et al., 2000).

2.1.2 Geometric effects

The finite distance of the Sodium layer and its vertical extension make the LGSs to cause some WF issues related to purely geometric aspects. Some of these problems increase with the telescope diameter and with the nearness of the sodium layer, being more severe at small Zenith angles.

Cone effect

Since the LGS distance is finite the incoming WF is spherical. On the high altitude turbulent layers the footprint of the LGS is smaller than the telescope diameter (figure 2.4a). The overlap percentage, respect to the footprint of an infinitely distant star, depends on the turbulent layer height H_l and Sodium layer height H_s. The footprint diameter D_l for a telescope diameter D is

$$D_l = D(1 - H_L/H_s) \tag{2.2}$$

The WF reconstruction using a single LGS results clearly less effective respect to an NGS in the same direction and with the same received flux, since part of the turbulence volume is not senses. The tomographic reconstruction of the atmospheric turbulence requires more LGSs, respect to NGSs, to sample the same metapupil area at a given altitude (figure 2.4b).
The cone effect is the main reason for the impossibility of using Rayleigh LGS for MCAO. These artificial stars are tuned on only at low altitudes, hence their footprints at the high turbulence layers are very small, requiring a big number of stars (and of course of WFSs) to have a proper metapupil coverage.

LGS launching angle

Figure 2.5a shows that the scientific FoV 2α and the incoming LGS light mean angle 2β are different. Their relationship can be calculated as

$$\beta = \mathrm{atan}\left(\frac{D/2 + H_S \cdot \mathrm{atan}(\alpha)}{H_S}\right) \tag{2.3}$$
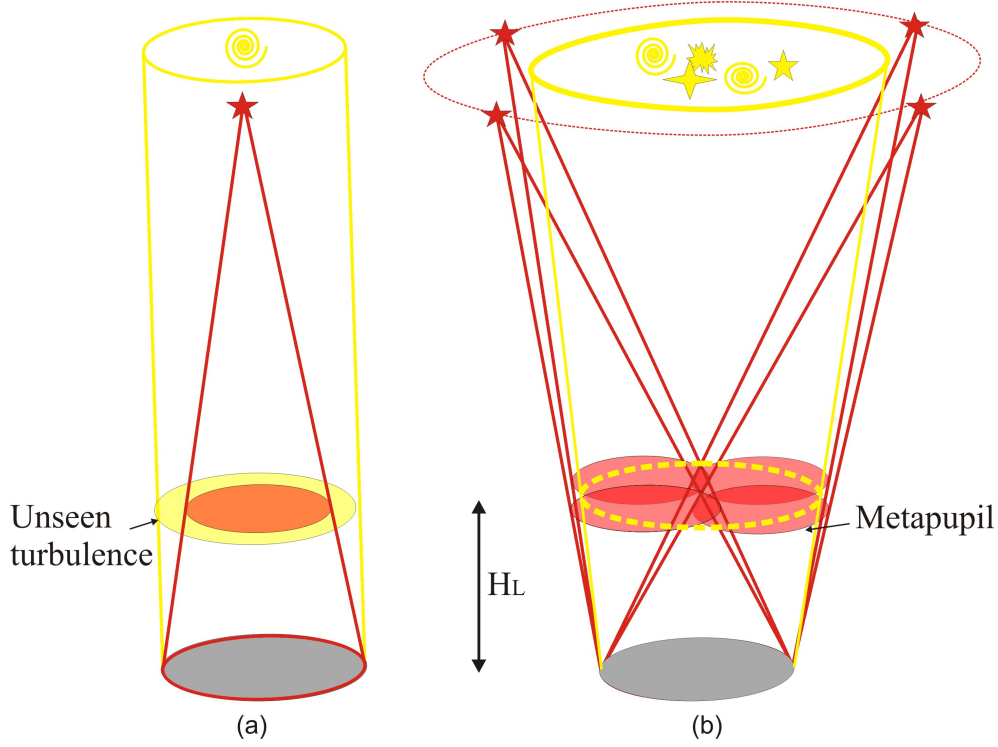
Figure 2.4: a) cone effect; b) MCAO with LGSs

. The technical FoV, defined by β $(> \alpha)$, is the angle for the LGS to sample the metapupil at a given height H_l for a scientific FoV defined by α. The LGS launching angle coincides with β in case of projection from behind the secondary mirror and α in case of side launch scheme. The described effect is true only from a purely a geometric PoV. The LGS launching angle can have an an impact especially on the MCAO and LTAO modules design where the optics dimension are defined by β in order not to vignet the incoming light of the LGSs (section 1.2.1). Considerations regarding the tomographic reconstruction, optimized for example for the center of the FoV, can reduce the difference between α and β, that looking at eq.2.3 increases with the telescope diameter D.

Zenith angle effect

The different zenith angle ξ between observations and its variation during the sky tracking changes the Sodium layer mean distance respect to the telescope by a factor depending on the cosine of ξ and consequently the LGS image shifts along the optical axis. The LGS WFS design must foresee some compensation
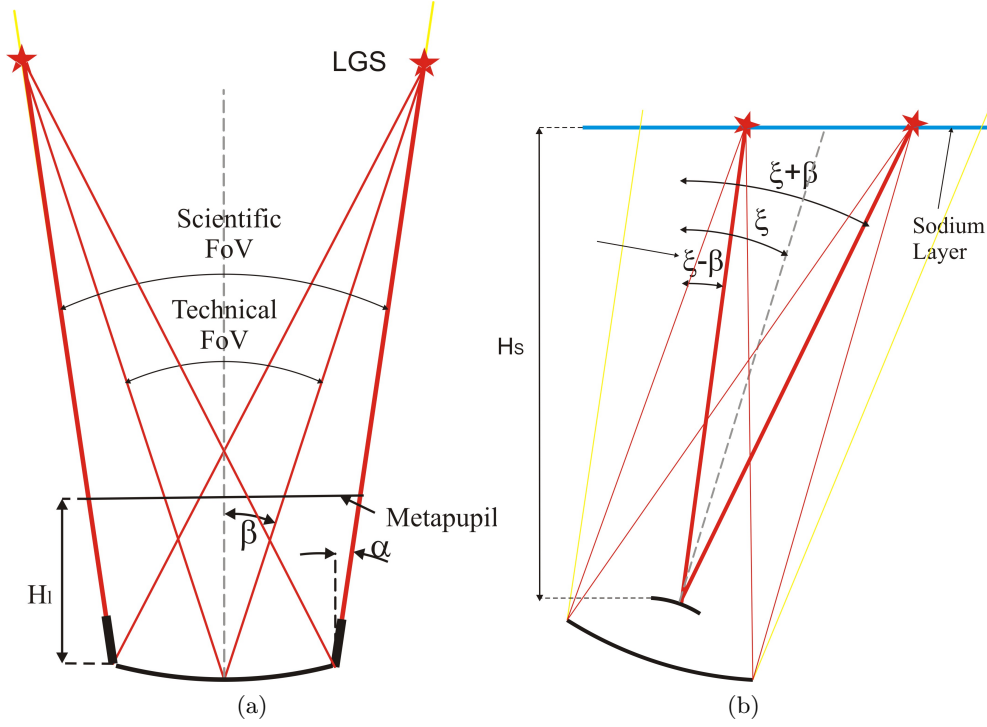
Figure 2.5: a)launch angle; b) Zenith angle effect

devices to follow the LGS image position and possibly reduce the $F_\#$ of the beams entering the LGS channel since this effect is proportional to it. In case of multiple LGSs (fig. 2.5b), for observations with non zero ξ, the different azimuthal angles of the LGSs respect to the optical axis, make the star to be formed at different distances from the Sodium layer to the telescope and thus a predictable defocus signal, whose intensity can be derived from eq. 2.6, occurs. For $\xi=30°$ and $\beta=1$arcmin the differential defocus in the direction of the LGSs is about 40nm RMS (eq. 2.6) that must be compensated separately by the different LGS probes.

Perspective elongation

The LGS is seen by the off-axis sub-apertures of a SHWS, respect to the upward laser beam axis, as an extended source due to parallattic effect. On the detector the spots appear elongated by an angular dimension ϵ, proportional to the sub-aperture distance r to the LGS launcher, that can be well approximated with the formula

$$\epsilon = \cos(\xi)r\left(\frac{1}{H_1} - \frac{1}{H_2}\right) \approx \cos(\xi)r\frac{\Delta H}{H_m^2} \qquad (2.4)$$
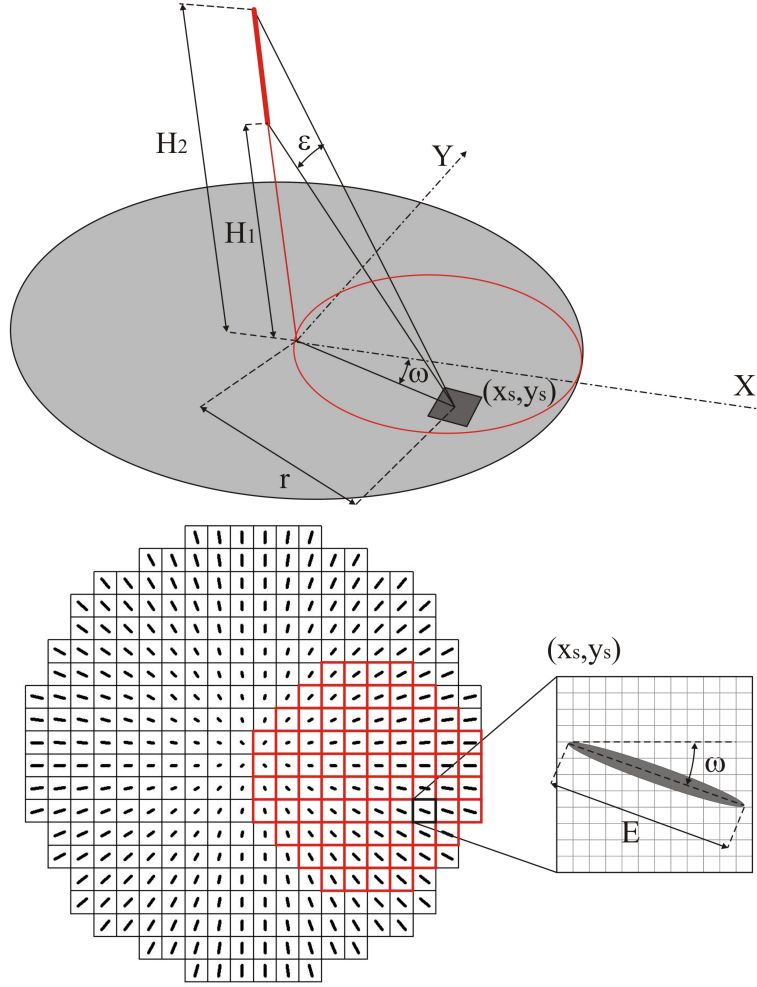
Figure 2.6: Upper figure: description of the LGS parallactic effect on the off-axis sub-apertures of a SHWS, the red circle indicates a telescope with side launch of the LGS; lower figure: geometry of the elongated spots array for the central launch configuration of the LGS and side launch scheme (red sub-apertures). The linear elongation of the spot is $E=\epsilon$ PS, where PS is plate scale on the Detector plane

where H_1 and H_2 are the LGS height edges (upper figure 2.6), $\Delta H = H_2 - H_1$ and H_m is the LGS mean altitude . The spot elongation orientation ω is always directed toward the laser launcher (lower figure 2.6).

$$\omega = \text{atan} \left(\frac{y_l - y_s}{x_l - x_s} \right) \tag{2.5}$$

with (x_l, y_l) the laser launcher coordinates and (x_s, y_s) the sub-aperture centers ones, in a common reference system. The elongation geometry of the side launch scheme can be thought as a sub-region of the radial elongation geometry

for a telescope having twice the number of sub-apertures (red bounded sub-apertures of figure 2.6).

The dependency of ϵ from r in eq. 2.4 produces, in case of side launch of the LGSs, a doubled maximum elongation respect to the central launch scheme for the same vertical extension of the source and the same telescope diameter. The choice to avoid, for example, the fratricide effect presented in section 2.1.1 has as a consequence the requirement for bigger Detectors.

2.1.3   Sodium layer variability
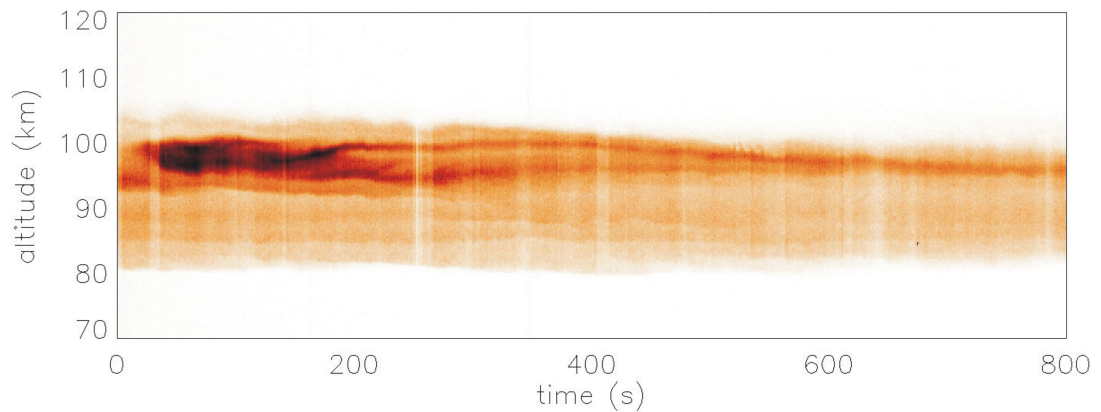
Figure 2.7: Sodium layer profile measurements kindly provided by Paul Hickson, Department of Physics and Astronomy , University of British Columbia.

In figure 2.7 a sample of the data from a campaign of measurements of the Sodium density, covering about 600s of timescale are displayed. These data were kindly provided by Paul Hickson (Department of Physics and Astronomy of the University of British Columbia) and are described in detail in Pfrommer et al. (2009). The columns represent the Sodium density with a altitude resolution of 50m. The measurements have a temporal resolution of 20ms. Unfortunately the low SNR of these data does not permit to distinguish the Sodium layer internal structures from fluctuations due to the measurement noise, up to a data binning of 200m in altitude and 1Hz in time. Anyway for the following considerations on the Sodium layer impact to the LGS WF sensing complexity and performance these binned data are good enough.
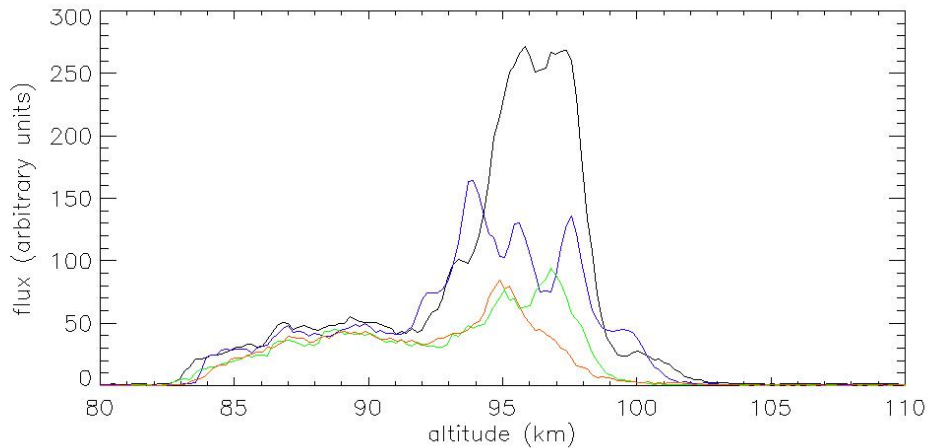
Figure 2.8: Sample of 4 Sodium layer profiles binned to 1s of temporal resolution and 200m of altitude resolution.

Intensity profile

The concentration of the Sodium layer varies significantly with geographical location (latitude, in particular) and also temporally, both seasonally and on timescales of hours or minutes. In particular, "sporadic events" can cause dramatic changes in the sodium layer on very short timescales (Clemesha, 1995). The density of the sodium layer can change by a factor of two or more depending on the telescope site and the time of the year (O'Sullivan et al., 2000). In figure 2.8 four intensity profiles taken from the Sodium Density data are plotted. It can be pointed out how the profiles and the intensities can be different in a relatively short timescale of ∼600s.

The slope measurement accuracy is affected by the elongated, irregular and time variable spot profiles: the loss of performance may be mitigated through advanced centroiding algorithms, that however require a 'template' of the LGS spot in each sub-aperture (Schreiber et al., 2009). The template for the LGS WFS centroiding algorithm may be determined for each sub-aperture as the temporal average of the LGS spot, but because of the Sodium profile variation the template has to be updated regularly during the closed-loop operations. The optimal integration time for the computation of the average template shall be short enough to avoid that the Sodium profile changes too much, but long enough to ensure a high SNR of the template itself. Another more subtle lower limit to the averaging time is set by the requirement of averaging out the

atmospheric turbulence, to avoid that the slope to be measured is "included" in the template; this aspect is mostly related to the low order modes that have a long correlation time. Finally the non stationarity of the atmospheric turbulence sets an upper limit to the template integration time: if the LGS image width due to the atmospheric seeing changes, the template may not be adequate to model the instantaneous profile and calibration errors may occur. A detailed study on an optimal handling of this issue is under investigation and will be presented in (Schreiber et al., 2011a)

Focus indetermination
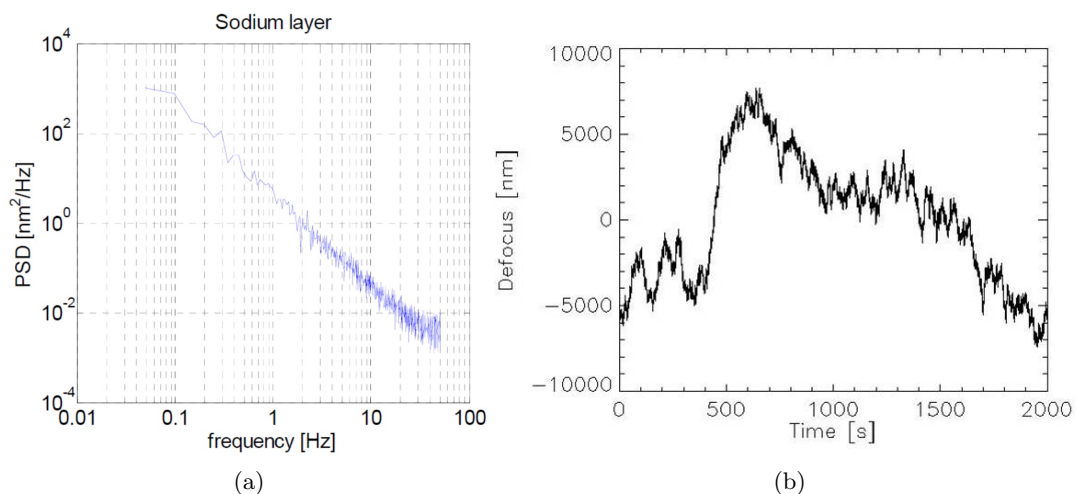
Figure 2.9: a) Temporal PSD of Sodium layer mean altitude taken from Oberti & Kolb (2008); b) Realization of a time sequence of the Defocus mean altitude for 42m telescope using the PSD of the image on the left.

Figure 2.9a shows the temporal PSD of Sodium layer mean altitude taken from Oberti & Kolb (2008), while in figure 2.9b a realization of a time sequence of the Sodium mean altitude, obtained by the PSD data, is presented. This random altitude variation, in addition to the predictable shift due to the changing zenith angle during the observation (section 2.1.2), is seen by the LGS WFS as a defocus signal, that must not be applied by the DM since the science images are not affected by this aberration. The RMS WFE σ_{def} from Sodium layer defocus is (Herriot et al., 2006)

$$\sigma_{def} = \frac{1}{16\sqrt{3}} \frac{D^2}{H^2} \Delta H \qquad (2.6)$$

For D = 42 m and H = 90 km σ_{def} is 8nm RMS for each meter of mean altitude mismatch ΔH. Note that for MAORY (section 1.2.1) the entire Error Budget set by the science requirements is 300nm of WFE (Diolaiti et al., 2010), equivalent to ΔH =40m. The dependence of this error with the square of the telescope diameter can make us understand how, passing from a 8m to an ELT class telescope, the Sodium layer focus tracking and its disentanglement from the atmospheric defocus comes to be very critical.

The strategy for GeMS (Neichel et al., 2010) at the 8m Gemini South telescope, is to use one NGS over three, the brightest one, also to measure the residual defocus signal, at a lower rate respect to the atmospheric defocus measurement, achieved by the LGS WFSs. By comparison of the defocus estimated in the direction of the NGS, it is assumed to be able to cancel the sodium layer component (Rigaut et al., 2010). The same strategy is foreseen also for MAORY and NFIRAOS (Foppiani et al. 2010, Herriot et al. 2010), the MCAO modules for respectively the EELT and the TMT. Anyway for larger diameter telescopes, looking at eq. 2.6, the defocus measurement rate by means of the NGS must be clearly faster because an equal variation of the Sodium layer mean altitude produces a σ_{def} much bigger.

Unfortunately the currently available Sodium density data do not permit to precisely retrieve the rate of this mean height variation. In fact the photon noise error in the profile centroiding is about 30m, well above the required accuracy of about 1m to properly extract a sufficiently fast measurement rate. Moreover the question regarding the anisoplanatism of the Sodium layer is still pending. No data yet demonstrated whether the LGSs of a given asterism, launched on a circle of 2 arc minutes for example, would experience different Sodium profiles and thus different mean Sodium heights. In this case a possible solution is to use all the three NGSs to measure also the defocus.

Low order modes NCPA

The LGS parallactic effect on the off-axis sub-apertures of a SHWS is inversely proportional to the square of the Sodium layer distance (eq. 2.4). Figure 2.10 shows that for a given FoV centered at the altitude H_m, a sub-aperture at distance r from the laser launcher receives the LGS light between the heights range H_{min} and H_{max}. These two altitudes have different vertical distances from H_m due to the longitudinal magnification that depends on the square of
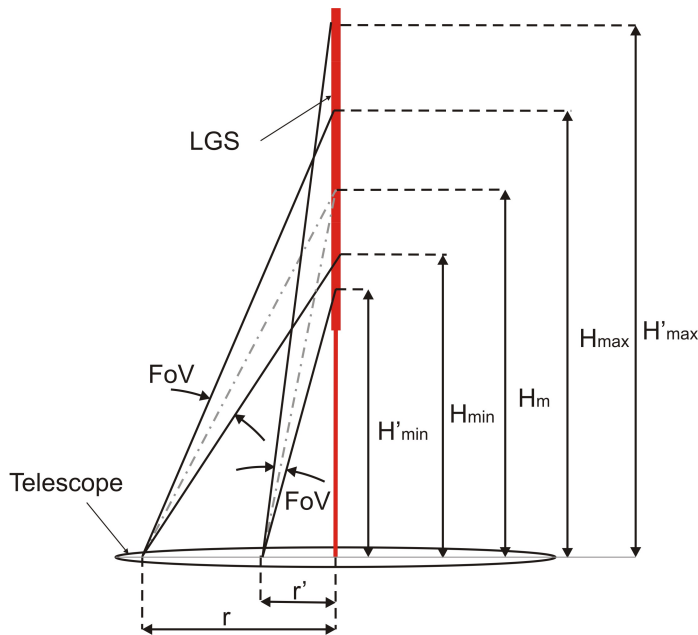
Figure 2.10: Parallactic effect: a sub-aperture with a given FoV at a distance r from the laser launcher and centered at H_m, sees the LGS inside two edge heights H_{min} and H_{max} that are at different distances from H_m. Spot truncation effect: two sub-apertures having the same FoV and centered at H_m, placed at difference distances r and r' from the laser launcher, see different segments of the LGS vertical extension. The on-axis sub-aperture receive the light from any altitude of the LGS.

the distance but, being at the same angular distance from H_m, the two half of the LGSs are re-imaged on the Detector over the same number of pixels. Even for a Gaussian intensity profile of the LGS the spot elongation would be asymmetric, with a longer tail from the lower part of the LGS. This effect causes a spots offset proportional to the distance of the sub-aperture from the laser launcher.

For an LGS WFS the FS has the purpose of truncating the elongated spots that would overflow into the adjacent sub-apertures (figure 3.22). The choice of the sub-apertures FOV depends on the sampling of elongated images and it is a trade off between the number of pixels per sub-aperture and the spot centroiding WFE. A reasonable value for the FoV is ∼12arcsec FoV. It corresponds to about 12km of Sodium layer vertical extension re-imaged by the most elongated sub-aperture, when observing at Zenith with the EELT and for the side launch scheme of the LGS. The Sodium layer vertical extension usually extends for more than this value (fig. 2.7), so a spot truncation occurs.
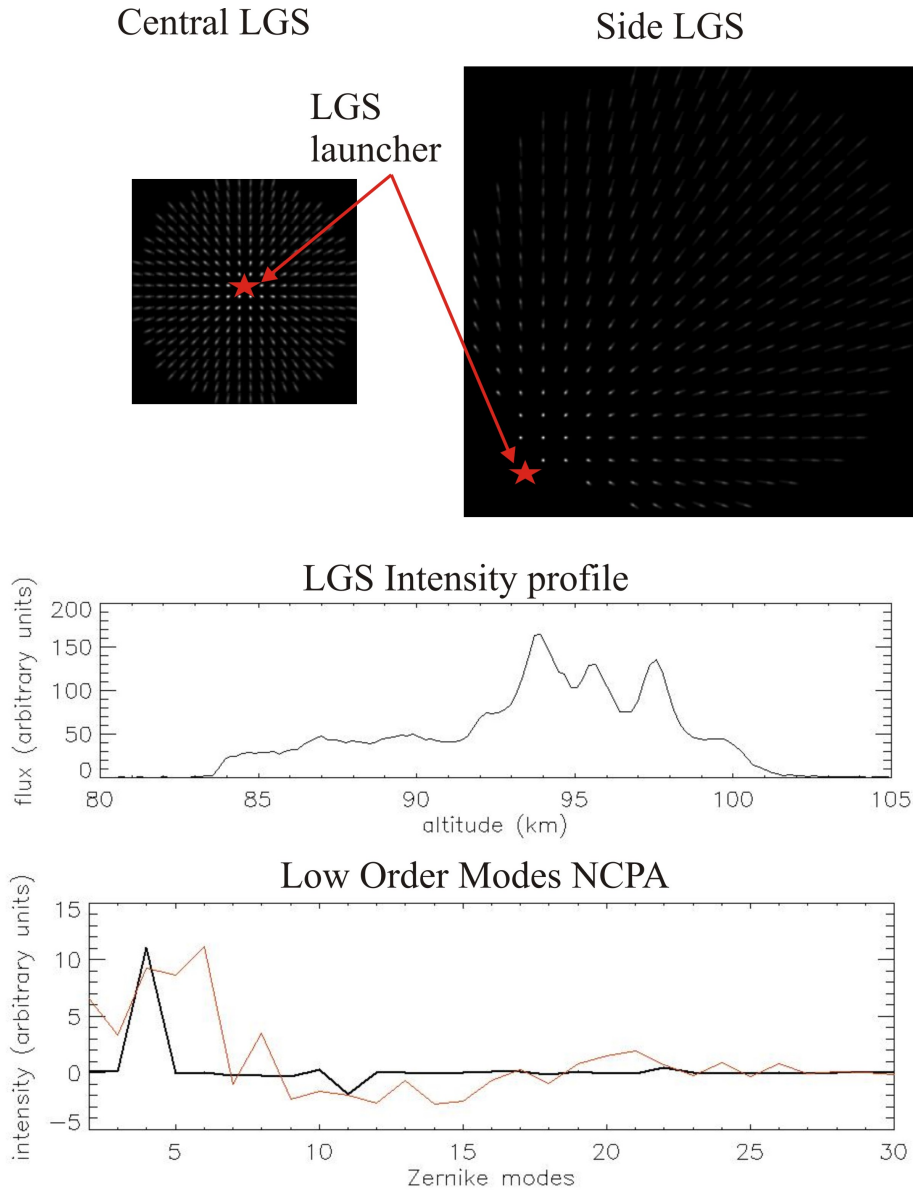
Figure 2.11: Simulation of the spots array of a SHWS from an LGS, having the intensity profile given by the upper plot, for central launching (left figure) and side launching schemes (right figure). The same platescale in the two cases results in a different number of pixels for the two launching configurations. The lower plot shows the low-order modes caused by the parallactic and the spot truncation effects for central launch (black line) and side launch (red line)

Two sub-apertures at distances r and r' from the laser launcher, having the same FoV and centered at H_m, receive the light from a different segment of LGS (fig. 2.10). Since the Sodium profile is irregular, in the two sub-apertures two spots with slightly different intensity profiles are re-imaged. Using the

Sodium density profile of figure 2.11 the corresponding LGS images in each sub-aperture were created. Two spot arrays simulating a SHWS having 20 sub-apertures over the pupil diameter, for central and side launch of the LGS, are shown in figure 2.11. The two figures have the same sub-apertures FoV and platescale, thus the symmetrical spot array requires half of the pixels per sub-aperture respect the other spots array (eq. 2.4). By calculating the spot centroids, the WF maps have been reconstructed and the Zernike modes composing the two WFs calculated. The images do not contain any noise due to atmospheric turbulence or RON, so the measured aberrations depend only by the parallactic effect and the spots truncation. Since these two effects are function only of the distance between the sub-aperture and the laser launcher (and of course of the profile), the Zernike modes are radial for the central launch scheme (Zernike=4,11,22 in the black line of the lower plot of fig. 2.11) while for the side launch configuration also other low order modes are present (red line).

2.2   LGS sky coverage
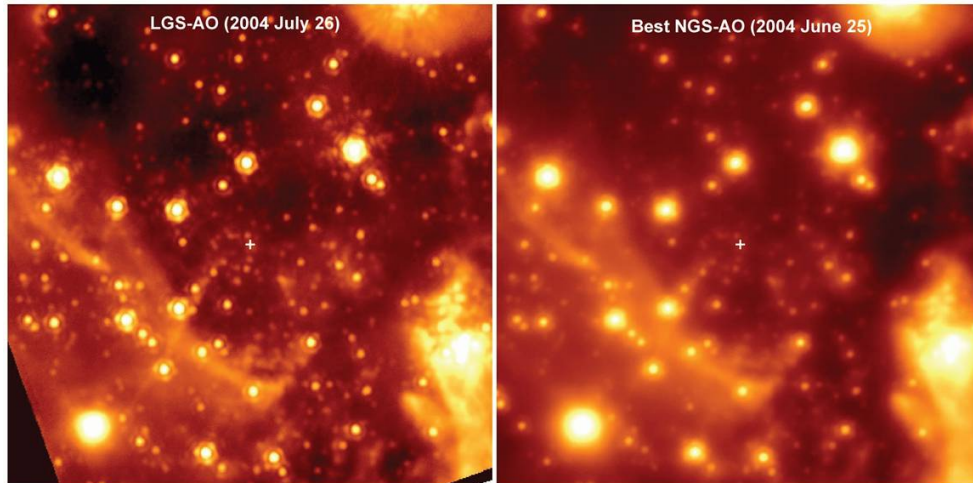
Figure 2.12: Comparison of the first LGSAO image (left) and the best NGSAO image (right) taken with the Keck II 10 m telescope (2002–2004) in the L' (3.8μm photometric bandpass of the central 7.5"x7.5" of our Galaxy.

We make now few considerations regarding the sky coverage comparison between the NGS and LGS WF sensing, using as example the observations of the Milky Way center at Keck telescope, shown (figure 2.12), carried out by means of two different AO techniques: single NGS and single LGS (plus

TT-NGS) WF sensing (Ghez et al., 2005). The left figure shows a diffraction limited core image obtained using an LGS of m_{LGS}=11.4 ($\lambda = 0.589\mu$m) and a TT star of m_{NGS}=13.7 (R-band, central $\lambda = 0.7\mu$m) at 18arcsec from the field center, with a measured SR ~ 0.68 (L'-Band, central λ=3.8μm). The right figure was obtained by means of a single NGS of magnitude m_{NGS}=13.2 (R-Band) at 31arcsec from the field center,with a SR $\sim$0.33 (L'-Band). The on axis SR of the LGS case is about twice the NGS case. The following sky coverage estimation are based only on the GSs magnitude, neglecting any other difference between the two WFSs or the atmospheric parameters during the two observations.

The NGS star has a magnitude close to the limit for a SHWS for AO appications as explained in section 1.1.2, and its distance from the field center degrades the correction performance due to the isoplanatic error, described in eq. 1.7. The image stabilization performance from the TT NGS is instead degraded by the isokinetic angle (section 2.1.1), quite bigger than the isoplanatic angle.

The influence of the TT NGS magnitude in the LGS WFS performance can be estimated by the following formula regarding the SR degradation on the direction of the LGS, in terms of peak intensity of the diffraction limited image, due to TT error (Sandler & Stahl, 1994)

$$S_\theta = \frac{1}{1 + \sigma_{SH}^2/4} \tag{2.7}$$

where σ_{SH}^2 is the measurement noise of the SHWS presented in equation 1.6. The TT NGS magnitude on the value of σ_{SH}^2 has clearly less impact than the classical NGS case, since all the light collected by the pupil, instead of the light per sub-aperture, contributes to decrease the measurement noise. The magnitude of the TT-NGS star in the case we are considering reduces the on-axis SR of 10%. The required magnitude that would have halved the SR, to be comparable to the NGS AO case , is about m_{NGS}=18.5.

The magnitude of the NGS available for the Galactic Center observation is not an unlucky case since the number of brighter stars suitable for AO is small. In the two plots in figure 2.13 the cumulative star counts n_{gs} per arcmin^2 at the Galactic Anticenter and at the Galactic Pole, using the Besancon model of stellar population synthesis of the Galaxy (Robin et al., 2003), are presented. In a poissonian distribution the probability of having at least 1 NGS, when

the mean number of NGS is 1 in the FoV, is P~0.4 . Multiplying the expected n_{gs} referred to the magnitudes of the classical NGS and the TT NGS by P, the sky coverage can be calculated. The case of single GS AO in 1arcmin FoV is presented in table 2.1.

In case of LGS MCAO, when 3 NGSs are used for TT measurement, the above
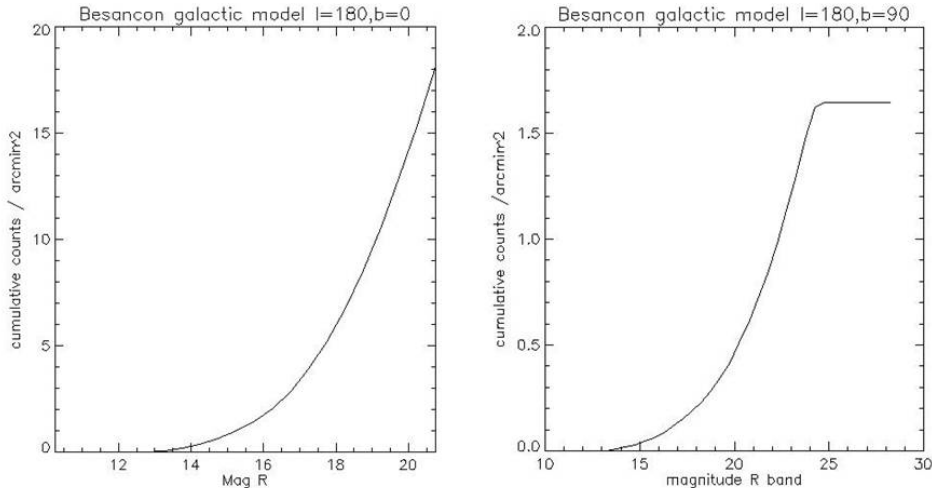
Figure 2.13: Besancon model for the estimation of the cumulative counts of stars per arcmin^2 in function of the magnitude in R-Band at Galactic anticenter (left) and Galactic pole (right).

limit magnitude (R)	Galactic anticenter counts/arcmin^2	sky coverage %	Galactic pole counts/arcmin^2	sky coverage %
13.5	0.16	5	0.02	<1
18.5	11	100	0.7	25

Table 2.1: Sky coverage estimation for single reference AO for classic NGS WFS and LGS WFS at the Galactic anticenter and Galactic pole, based on the Keck Observatory AO performances.

calculations become more complicated since also the asterism geometry and the GSs magnitude difference affect in the system performance. Anyway the increased FoV permits to raise also the sky coverage, as presented in Gemini website.

The sky coverage for the MCAO at Gemini is computed as the fraction of the sky over which the SR loss is 50% with respect to the noiseless performance on bright stars. For MAORY the sky coverage requirement is more stringent since the minimum SR to be delivered is computed on a loss of 50% respect

to the ideal diffraction limit peak (see table 1.1). This involve a refinement of the image motion correction technique caused by a faster measurement rate. Brighter TT NGSs are required, without lowering the sky coverage. The foreseen strategy is the measurement of the GSs WF in the H-Band (λ centered at 1.1μm) or J-Band (λ centered at 1.65μm) so that NGS images can benefit from the AO correction and thus have diffraction limited core. The SNR is this case, for background limited images, grows with the square of the telescope diameter respect to be proportional to D as for seeing limited images (Roddier, 1999), so fainter NGSs can be used. Even though the sky background per square arcsec in the NIR bands is usually quite brighter respect to the shorter wavelengths (ESO sky bkg data), the shrunk NGS images are contaminated by much less background photons. Accurate simulations (Clare et al., 2006) resulted in a clear advantage in using the TT NGSs in the NIR band ($\lambda > 1\mu$m) respect to the Visible Band.

2.3   Alternative WFS concepts

The LGSs are almost routinely used in the current 8-10m diameter telescopes. Anyway not all the adopted solutions to deal with the LGS issues described above in this chapter can be applied to the EELT case, for technological reasons or because the WFE related to some LGS features grow with the diameter ($\propto$D or D^2), and thus a different approach must be thought.
The SHWS is the EELT baseline WFS. Considering 84x84 sub-apertures to sample the pupil images and the side launch scheme of the LGSs, even with under-sampled spots (1pixel/FWHM along the non elongated direction), the required number of pixels of the Detector would be >1000x1000, quite above the current Detectors size suitable for AO applications (high reading rate and low RON). Moreover the spread of the elongated spots into several pixels reduces the SNR and consequently increases the centroiding measurement error (eq. 1.6), hence more laser power per LGS respect to the present day availability is required. Finally, additional WFSs must measure the NCPA produced by the Sodium layer instability: a RWFS must measure the low order aberrations and one (or more) NGS WFSs must deal with the Sodium layer focus indetermination, at a faster rate respect to smaller telescopes (section 2.1.3).
An overview about possible alternatives to the SHWS, with the goal to mitigate

the spot elongation and relax the requirements on some key components, as the laser power or the Detector size, can be found in Butteley & Love (2008). Most of these concepts require pulsed lasers and a dynamic refocusing.

In AO it is usually defined as pulsed a laser beam having a pulse rate few times faster than correction frequency, related to the turbulence coherence time τ_0 of eq. 1.2. A synchronization between the pulse and some refocusing elements inside the AO module has the goal to vary the focal length of the LGS WFS optics and maintain a fixed focal plane as each laser pulse moves up through the atmosphere. The dynamic refocus can be performed by means of fast mirror in the focal or pupil image plane (Hugot et al. 2010, Baranec et al. 2005) or using a custom polar coordinates CCD after a LA (Herriot et al., 2006). The required number of pixels and photons per sub-aperture are in this way comparable with the case of NGS WF sensing. Anyway this technology scaled to the EELT presents technological issues not yet demonstrated.

Actually also the so called CW lasers have a pulse, comparable with the radiative lifetime due to spontaneous emission of a Sodium atom in either of the excited states of about 16ns (D'Orgeville et al., 1999), that has no effects on the WFS and thus it is not considered.

At the beginning of MAORY Phase A study we started to investigate the behavior of two WFSs working with CW lasers: the BPWS and the PWS. We then decided to focus our attention on the baseline SHWS both in the simulations and in the LGS Prototype. We resumed the studies and present now the concepts, leaving to the papers in preparation (Lombini et al., Schreiber et al. 2011b) a more detailed description of the two WFS performance.

2.3.1 Bi-Prism Array WFS

The BPWS is a static optical approach that could permit to reduce the requirements on the Detector size and to cut down the WF sensing issues caused by the Sodium layer instability. The basic concept of the BPWS is the measurement of the local WF, in each sub-aperture, perpendicularly to the elongation direction ω of the re-imaged spots (fig. 2.6). The roofs of the BPs, placed on the focal plane of a LA, are in fact parallel to ω. In each sub-aperture ω, and consequently the local slope measurement, depends only on the laser launcher position and not on the LGS launching angle respect to the optical

axis, hence it is a fixed parameter. All the BP arrays, coupled to different LGSs, are identical to each other, only rotated to match the elongation pattern directed to the launcher. To reconstruct the WF slopes in two orthogonal reference direction x and y in each sub-aperture, it is necessary to combine the signals from pairs of LGSs launched at different positions.

Design

The BPWS design is based on an array of refracting BPs placed on the focal plane of a pupil plane LA. Each BP splits the elongated spots into two beams that are re-imaged, by means of another LA, into two micro-images of the sub-aperture itself (Fig. 2.14). The difference in the intensity of these two micro-images is proportional to the local WF slope.
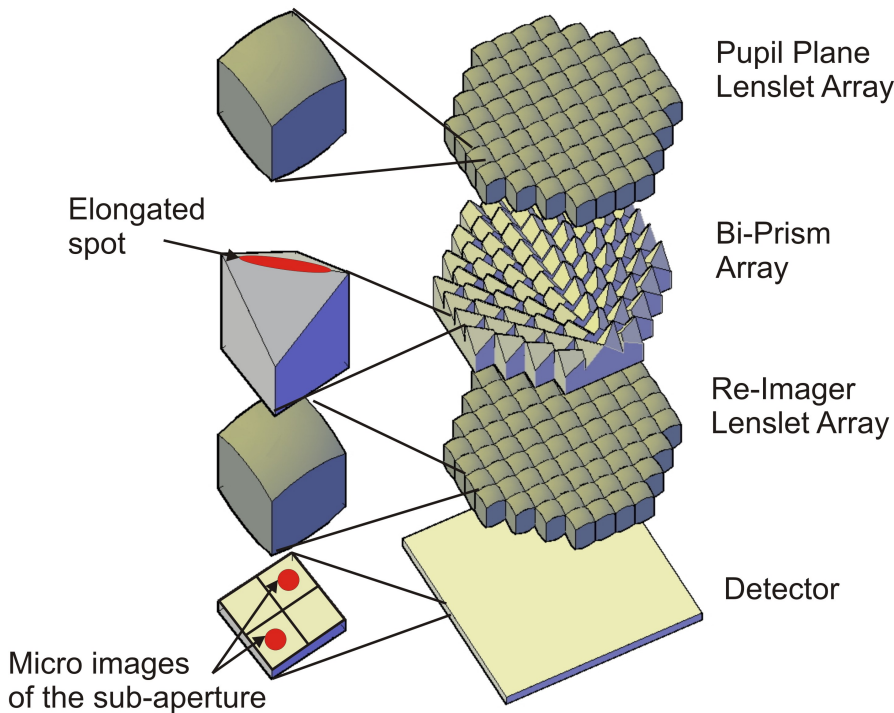
Figure 2.14: Concept of the BPWS.

The sub-aperture size d_{sub} can be calculated from the maximum allowed spot elongation ϵ (eq. 2.4) and the telescope effective focal length f_{tot}

$$d_{sub} \geq \epsilon \, f_{tot} \tag{2.8}$$

where f_{tot} is

$$f_{tot} = \frac{f_{tel} \cdot f_1}{f_{coll}} \tag{2.9}$$
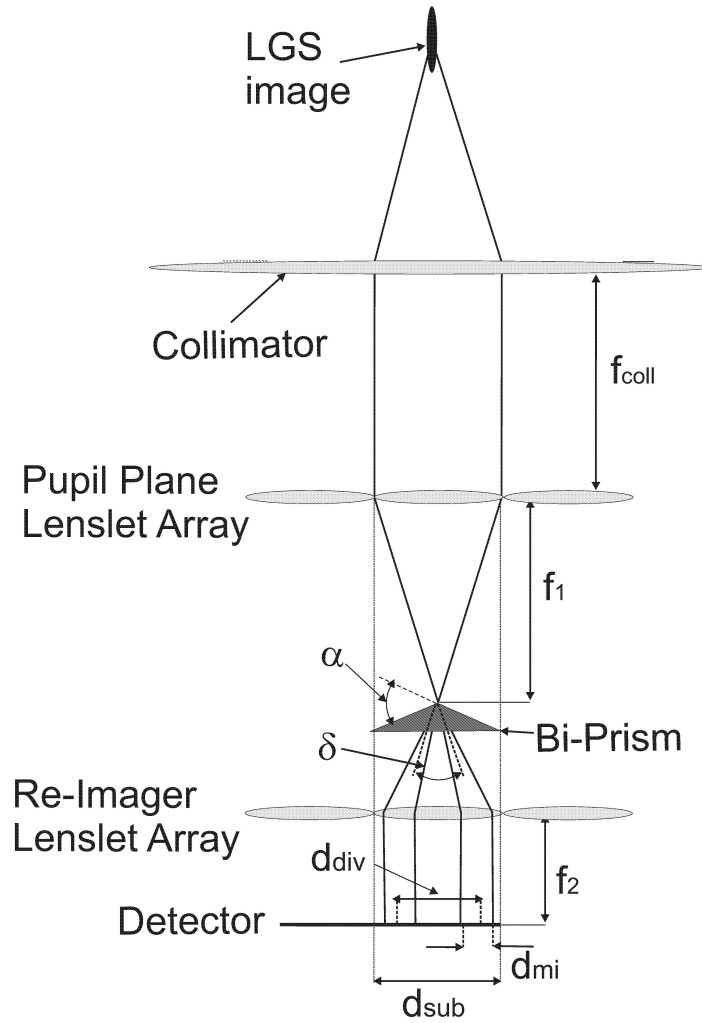
Figure 2.15: BPWF main optical parameters.

being f_{tel},f_1 and f_{coll} respectively the telescope, pupil plane LA and collimator focal lengths (fig. 2.15). The diameter of a micro image d_{mi} on the Detector is:

$$d_{mi} = d_{sub}\frac{f_2}{f_1} \tag{2.10}$$

where f_2 is the re-imaging LA focal length. The pupils distance d_{div} on the detector is:

$$d_{div} = \delta \cdot f_2 \tag{2.11}$$

with $\delta = \alpha\,(n-1)$ the BP divergence angle, α its vertex angle and n the refraction index. On the Detector plane the sub-aperture is formed by a number of pixels n_{pix} having d_{pix} of side dimension. The BPWS parameters can be chosen in order to reduce the number of pixels per sub-aperture and

thus also the Detector dimension. In table 2.2 the optical parameters of the BPWS for a 42m telescope are presented.

Custom optical arrays have been proposed (Bauman, 2003) or already built

Parameter	value
Telescope diameter	42m
Telescope Focal aperture	17.7
Collimator focal length	142mm
Num. of sub-aper over the diam	84
Sub-aper FoV	10arcsec
Num. of pixels/sub-aper	4x4
Num. of pixels over Detector	256x256
pixel size	24μm
Sub-aper side	96μm
LA1 focal length	0.7mm
LA2 focal length	0.15mm
Bi-Prism vertex angle	$60°$
Micro-images diameter	10μm
Micro-images distance	24μm

Table 2.2: Main parameters of the BP WFS for the EELT case

as, for example, in VLTI-MACAO (Arsenault et al., 2003). We believe that the manufacturing difficulties of custom optical arrays as the ones needed by the BPWS could be worthwhile, due to the requirement for an already existing Detector size, in case of performance comparable to the SHWS.

Signal combination

The signal combination of two slopes in a given sub-aperture requires linearly independent slope vectors, so it is necessary to project the LGSs from the edge of the primary mirror, otherwise the elongation pattern would look the same for all the LGSs, directed toward the central sub-aperture. To explain the signal combination let us consider two BPWSs that look at two LGSs launched from the points (x_a, y_a) and (x_b, y_b) at the edge of the telescope primary mirror, as represented in figure 2.16. For a given sub-aperture of coordinates (x_s, y_s), for example the one marked with a square, two BPWSs measure the local WF slope in the directions, $\boldsymbol{\gamma}_a$ and $\boldsymbol{\gamma}_b$

$$
\boldsymbol{\gamma}_a = atan\left(\frac{x_s - x_a}{y_s - y_a}\right)
$$
$$
\boldsymbol{\gamma}_b = atan\left(\frac{x_s - x_b}{y_s - y_b}\right) \tag{2.12}
$$
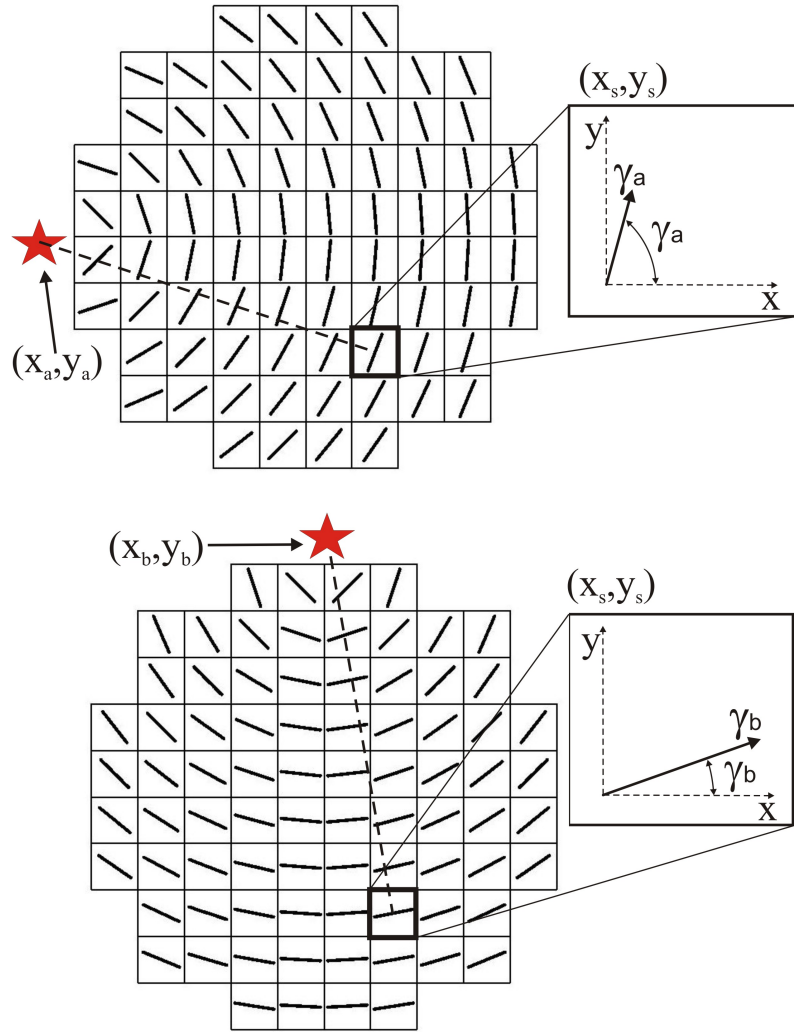
Figure 2.16: Slope measurement directions using the BPWF with the LGS launched from the left (upper figure) and from the top (lower figure) of the primary mirror. The coordinates x_s and y_s refer to the sub-aperture center.

The two measurements of the 'partial local slope' can be represented as vectors. These two vectors can always be orthogonalized. This means that the local slopes in two linearly independent directions can be always converted in local slopes in two orthogonal directions. The two orthogonalized slopes then are rotated by a proper angle to a common reference frame (x-y). The ortonormalization process of $\boldsymbol{\gamma}_a$ and $\boldsymbol{\gamma}_b$ to the unitary vectors $\mathbf{x}$ and $\mathbf{y}$ is

$$\mathbf{x} = A\boldsymbol{\gamma}_a + B\boldsymbol{\gamma}_b$$
$$\mathbf{y} = C\boldsymbol{\gamma}_a + D\boldsymbol{\gamma}_b \qquad (2.13)$$

where A, B, C, and D are the orthogonalization and rotation coefficients that depend on the angles γ_a and γ_b between the directions $\boldsymbol{\gamma}_a$ and $\boldsymbol{\gamma}_b$ and the

common reference direction $\mathbf{x}$ (fig. 2.16)

$$A(\boldsymbol{\gamma}_a, \boldsymbol{\gamma}_b) = \cos\gamma_a + \frac{\sin\gamma_a \cos(\gamma_b - \gamma_a)}{\sin(\gamma_b - \gamma_a)}$$

$$B(\boldsymbol{\gamma}_a, \boldsymbol{\gamma}_b) = -\frac{\sin\gamma_a}{\sin(\gamma_b - \gamma_a)}$$

$$C(\boldsymbol{\gamma}_a, \boldsymbol{\gamma}_b) = \sin\gamma_a - \frac{\cos\gamma_a \cos(\gamma_b - \gamma_a)}{\sin(\gamma_b - \gamma_a)}$$

$$D(\boldsymbol{\gamma}_a, \boldsymbol{\gamma}_b) = \frac{\cos\gamma_a}{\sin(\gamma_b - \gamma_a)} \tag{2.14}$$

In the same way as eq. 2.13 the retrieved signals of two BP in the x-y directions are:

$$S_x = AS_{\boldsymbol{\gamma}_a} + BS_{\boldsymbol{\gamma}_b}$$

$$S_y = CS_{\boldsymbol{\gamma}_a} + DS_{\boldsymbol{\gamma}_b} \tag{2.15}$$

with $S_{\boldsymbol{\gamma}_a}$ and $S_{\boldsymbol{\gamma}_b}$ being the two signals in the same sub-aperture from the two corresponding directions.

Given an even set $S = \{1, 2, .., N\}$ of N indexes representing the LGSs, there are N/2 pairs of indexes related to the couple of LGSs whose signals are combined to obtain the x and y local slopes described in eq. 2.15.

WF reconstruction

The BPWS measurement error per sub-aperture is derived from the quad-cell one (Hardy, 1998):

$$\sigma_{BP} = \frac{\pi^{3/2}}{2\sqrt{ln2}} \frac{\sqrt{n_{ph} + n_{pix}\sigma_{RON}^2}}{n_{ph}} \frac{d_{ima}}{d_{diffr}}(radians) \tag{2.16}$$

where n_{ph} is the number of detected photons, n_{pix} is the number of pixels in the sub-aperture,σ_{RON}^2 is the RON, d_{ima} represents the size of the spot in the non elongated direction and d_{diffr} is the size of the diffraction limit image in the sub-aperture. The measurement error is propagated through the orthogonalization process presented in eq. 2.15. The slope reconstruction error from two directions $\boldsymbol{\gamma}_a$ and $\boldsymbol{\gamma}_b$ to a common reference frame (x,y) is given by:

$$\sigma_x = \sigma_{BP}\sqrt{\left(\cos\gamma_a + \sin\gamma_a\frac{\cos(\gamma_a - \gamma_b)}{\sin(\gamma_a - \gamma_b)}\right)^2 + \left(\frac{\sin\gamma_a}{\sin(\gamma_a - \gamma_b)}\right)^2}$$

$$\sigma_y = \sigma_{BP}\sqrt{\left(\sin\gamma_a - \cos\gamma_a\frac{\cos(\gamma_a - \gamma_b)}{\sin(\gamma_a - \gamma_b)}\right)^2 + \left(\frac{\cos\gamma_a}{\sin(\gamma_a - \gamma_b)}\right)^2} \tag{2.17}$$

In a sub-aperture of coordinates (x_s, y_s) the averaged slopes $\widehat{S_x}$ and $\widehat{S_y}$ of N LGSs are calculated by means of a linear combination (the Maximum Likelihood Estimation for example) of the slopes S_x and S_y derived by the combination of all the pairs of LGS signals. In the approximation of an equal number of photons over all the sub-apertures, the measurement error of the BPWS in eq. 2.16 is constant. The orthogonalization errors of eq. 2.17 depends on the angle between the two directions to be coupled respect to the right angle. The choice of the LGSs to be couples is chosen between the combination, in each sub-aperture, that minimize the reconstruction errors.

We are investigating, by means of numerical simulations, the WF reconstruction performance of the BPWS for the EELT in the simplest case of GLAO. The results will be compared to the SHWS, where the centroid measurement error grows with the elongation of the spot (Thomas et al., 2006). The requirements in terms of system complexity and technological feasibility will be discussed in the cases of similar performance of both WFSs.

2.3.2 Pyramid WFS
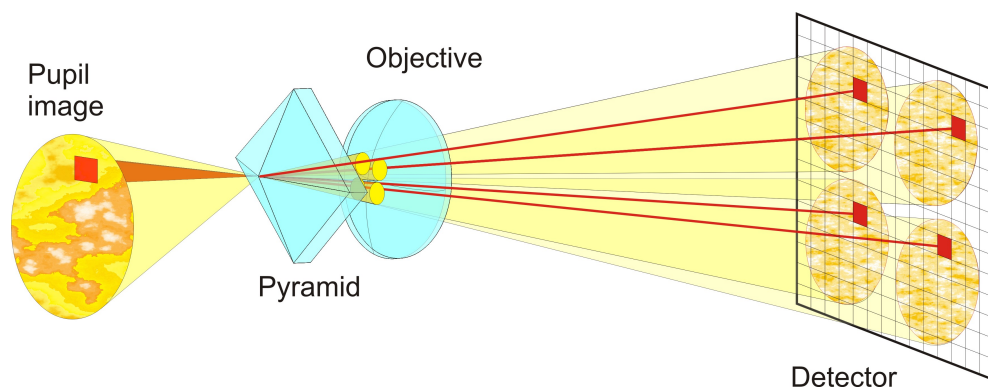
Figure 2.17: PWS working principle. The light is focused onto the tip of the pyramid and split into four beams. The four pupils are then imaged with a relay lens onto the detector. The red ray indicates the path from a sub-aperture that is re-imaged into 4 pupil images. In the presence of WF aberrations the light intensity distributions in the 4 red pixels is proportional to the local tilt of the WF.

The PWS working principle is similar to the Foucault knife edge test and in the geometrical approximation it is sensitive only to the sign of the WF slope (Malacara, 1978). The application of this WFS in AO applications (Ragazzoni, 1996) has been successfully demonstrated on the sky (see for example Arcidiacono et al. 2010 or Esposito et al. 2010). In the PWS the light

of an aberrated WF is focused on the pyramid tip and split into four beams. Four pupils are then re-imaged by means of an objective onto a Detector (figure 2.17). If the incoming WF is flat the four pupils have an equal illumination. In the simple case of a pure tilt, all the light is focused onto one face of the pyramid, yielding one bright and three dark pupil images on the Detector. In the presence of aberrations the shape of the PSF on the pyramid tip is no more uniform (left figure 1.1), and thus the distribution of the light among the four beams changes.

Since the dynamic and linear range of a pyramid WFS is rather small, as soon as the focused spot leaves the tip of the pyramid, only one face is illuminated. To enable a linear measurement of the local slope tilt a modulation of the pyramid tip or of the image by means of a pupil plane TT mirror (Riccardi et al., 1998), with a frequency that is an integer rate of the Detector frame rate, can be produced. The Layer Oriented WFS for MAD (Ragazzoni et al., 2008) demonstrated that the residual atmospheric turbulence at the NGS WF sensing wavelength produces a natural modulation of the images on the pyramid pin (Costa et al., 2003)

Pyramid WFS with LGS
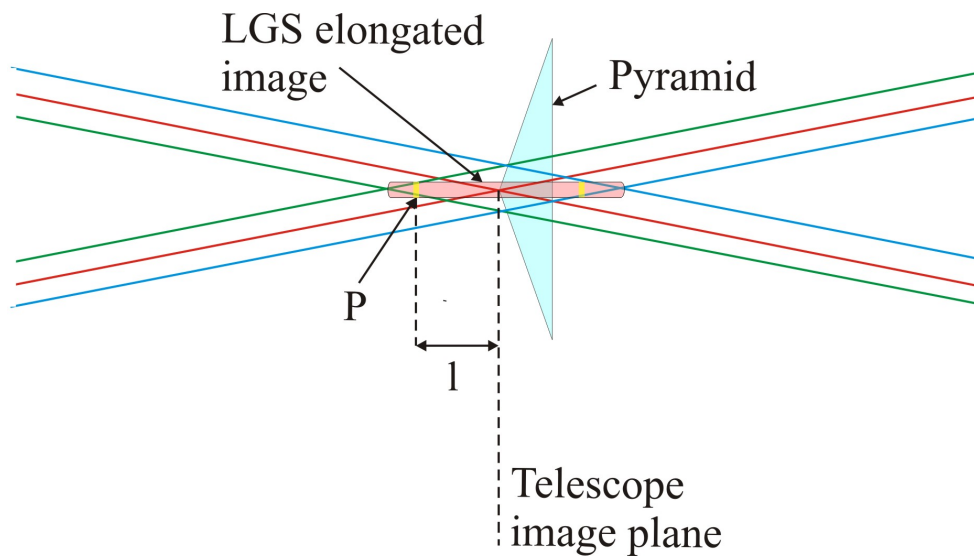
Figure 2.18: PWFS with an elongated image

The use of the PWFS with the LGSs has the straightforward advantage in the Detector size respect to the SHWS. Four pupil images having 84 sub-apertures over the diameter can be re-imaged on already available Detectors,

as the 264x264pixels Detector used by ARGOS at the LBT (Orban de Xivry et al., 2010) or the 240x240pixels one by Sphere at the VLT (Beuzit et al., 2005).

Figure 2.18 shows a pyramid placed at the center of an elongated image at the telescope image plane. If we ideally split the image into thin slices, we can consider the total measured signal by the PWFS as a sum from all the slices. Each slice will produce a signal formed, at the first order, by the atmospheric residual phase in the close loop regime ϕ_{res} plus a non atmospheric defocus term. The light focused in the slice P (figure 2.18), at the distance l from the pyramid pin, comes from a source located at an altitude at the distance ΔL from the LGS center, at H_m. Equation 2.6 gives the value of the non atmospheric defocus RMS σ_{def} from an image located in P respect to the one imaged on the telescope image plane. Considering D=42m, H_m=90km and ΔL=5km, the value of σ_{def} $\sim$40μm RMS, to be compared to ϕ_{res}, of the order a fraction of μm RMS. The PWS claims for a big dynamic range of the Detector or for a modulation of the image on the pyramid pin, to not saturate the signal. The modulation causes a reduction of sensibility and thus more photons are required. We are carrying out investigations on the PWS with LGSs regarding the dynamic range, modulation amplitude and number of photons required to retrieve a WFE comparable to the requirements of 8 to 40m class telescopes. The results will be compared to the SHWS case.

2.4   LGS WF sensing in MAORY

In this section it is described how the LGS issues presented in this chapter have been handled within the Phase A of MAORY (section 1.2.1). The baseline WFS is the SHWS, and 6 LGSs are assumed to be launched from the side of the telescope primary mirror. This scheme cancels the *fratricide effect* (the italic terms refer to the LGS issues described in this chapter) but increases the re-imaged spot sizes in the off-axis sub-apertures due to the *perspective elongation*. A mitigation on the Detector size requirement is investigated by under-sampling the spots. MCAO is also a solution to the *cone effect*.

The increase of the technical FoV due to the *LGS launching angle effect* is mitigated by an optimized strategy for tomographic reconstruction of the atmospheric turbulence in the science instrument FoV (53x53arcsec), accepting a lower correction in the outer FoV where the NGSs are searched (Conan et

al., 2009).

Due to the LGS *TT indetermination and anisoplanatism* 3 NGS are required: as a baseline 2 of them are used to measure tip-tilt only, while the third, positioned on the brightest star, is used to measure TT and defocus terms, in order to provide a reference for the rapidly variable defocus signal in the LGS WFSs caused by the *focus indetermination.*

The 3 NGS are observed in the near IR (H band), in order to take advantage of the spot shrinking ensured by the high-order correction driven by the LGS WFS, allowing the use of faint NGS. This is translated into a higher sky coverage. On each of the 3 NGS WFS channels, the light of wavelength 0.6μm-0.9μm is sent to a so-called Reference WFS, that operates typically at frequencies in the range 0.1-1 Hz, used to monitor the *Low order modes NCPA* related to the Sodium layer profile variability.

The global shift of the LGS image along the optical axis caused by the *Zenith angle effect*, common to all LGSs, is compensated by a overall motion of all 6 LGS WFSs together, while an individual compensations of the differential image shift in each LGS probe due the *MCAO Zenith angle effect* (fig. 2.5b) is produced by means of a trombone.

Among the Final Review documentation for the Phase A study of MAORY the 'Risk Assessment' document (Schreiber et al., 2009) presents an analysis of the risks and areas of concern associated to the design and construction. We list the risks related with the LGS WF sensing that can be investigated by means of the LGS Prototype described in next chapter.

Sodium layer mean height variability

> The baseline strategy for the NGS WF sensing is to use 2 stars for to measure the global TT measurement and one for TT and defocus. In case of focus anisoplanatism of the Sodium layer the defocus could be measured on all the three NGSs reducing the sky coverage 39% to 27% in the first line of table 1.1.

Profile variability

> All the centroid algorithms analyzed for the LGS WFS depend on the knowledge of the sodium density profile for proper functioning. In fact they all take advantage of a template that can be thought of as an averaging of the instantaneous spots and is measured by reference WFS for each NGS channel. The rate of the profile

variation is essential to set the Reference WFS velocity in function
of the WFE.

LGS return Flux

The number of detected photons per sub-aperture per frame used
for the simulations in is 500phe$^-$, which is higher than what is
currently achievable. Actions are undertaken to reduce the required
LGS return flux, including the study of advanced algorithms (e.g.
quad-cell) or alternative wavefront sensing schemes (section 2.3.

Detector

Considering that the baseline is to launch the lasers from the edge of
the primary mirror, the required dimension of the WFS Detector for
an elongated LGS is at least 1680x1680 (20x20 pixels sub-aperture
FoV) when Nyquist sampling of the LGS image in the non elongated
axis is adopted. The study about the LGS WFS design considers a
value of the RON equal to 3e$^-$. Exploring the possibility to under-
sample the spot up to 1"/pix leads to reduce the detector size if the
same sub-aperture FoV is considered but can require a calibration
by means of spot dithering.

Chapter 3

LGS Prototype

In parallel to the Phase A study of MAORY (section 1.2.1), the technological group of OABo and of the Astronomy Department of Unibo proposed, at the end of 2007, to build an LGS Prototype as part of the FP7 EELT Prep studies (Gilmozzi et al., 2008). For complex instruments as MAORY, the analytical and numerical simulations regarding the expected system performance should be completed by an independent experimental validation. The main goal of the Prototype was, in fact, to check the simulations results on the issues related to the LGSs, as described in section 2.1, that affect the centroiding algorithms performance of a SHWS. These simulations were carried out within MAORY group. The Prototype had to reproduce the LGS WF sensing conditions expected for a 42m telescope and since its design was started during MAORY Phase A study, we decided to focus on the SHWS, the baseline WFS of that study and of the other Phase A studies of the EELT (EELT instrumentation website). Anyway, we gave to the design enough flexibility to be able, with minor changes, to eventually explore other concepts of WFSs (section 3.7).

This 'first generation' LGS Prototype had to be quite simple from the opto-mechanical PoV, in order to be constructed and ready to deliver realistic images in about 2 years of timescale from the beginning of the study, in January 2008. For this reason we chose mainly commercial components and decided not to complicate much the CS part, preferring a robust and reliable machine.

In this chapter we describe the design of the Prototype, its alignment and briefly present the tests that have been carried on for our FP7 deadline. Finally possible opto-mechanical upgrades to add more functionalities and the relative new tests that could be exploited are shown.

Requirements

A SHWS for the EELT is foreseen to have 84 sub-apertures over the diameter that, considering 20x20 pixels per sub-aperture in case of Nyquist sampling, leads to a Detector size of about 1600x1600 pixels. Using the Detector we had in house, having 1056x1026 pixels, we decided to sample the pupil with 40 sub-apertures over the diameter, about half of the EELT case, and 24x24 pixels per sub-aperture. The required maximum spot elongation had to be 20pixels. The investigation on different image sampling, Nyquist and under sampled ones to reduce the sub-aperture size, could be achieved by means of a detector binning or varying the source diameter. The current strategy for EELT is with the side launch of the LGSs (Gonzales & S'Odorico, 2009) and thus this scheme was required to be delivered by the Prototype, in addition to the central launching scheme, necessary anyway in the alignment phase. The source profile had to reproduce the real Sodium ones described in figure 2.7 and a FS had to reproduce the spot truncation effects of the elongated spots on the Detector, described in section 2.1.3. Finally the flux intensity could be tunable, to work in different SNR regimes.

In table 3.1 a list of the parameters requirement, representing the different WF sensing conditions to be delivered, is listed.

Parameter	Value	Units	Notes
# of sub-apertures	40x40		half of EELT over the diameter
# pix/sub-aperture	24 x 24		
maximum foreseen elongation	20	pixel	
pixel scale	1 or 2	pix/FWHM	fiber change or detector binning
pixels per sub-aper	24x24, 12x12, 6x6		detector binning
launching scheme	central side side		rotation of the inear stage travel direction
sub-aperture FoV	≤12	pixel	FS diameter tuning
intensity profile	Gaussian Bi-modal Irregular		intensity filter change
Flux	50-2000	ph/sub-aper/int	power supply tuning

Table 3.1: Prototype requirements.

Man Power

The LGS Prototype development has been a team work involving the following people in different tasks:

Giovanni Bregoli: CS

Giuseppe Cosentino: Mechanical work, Electronics

Emiliano Diolaiti: components procurement, requirements, supervision

Italo Foppiani: CS, Electronics

Laura Schreiber: Data reduction and analysis of the results.

Regarding my involvement in this project, I had the Prototype construction responsibility, defined the requirements, made the design and carried out the AIT phase. The LGS Prototype is the key topic of my PhD thesis.

3.1   Conceptual Design
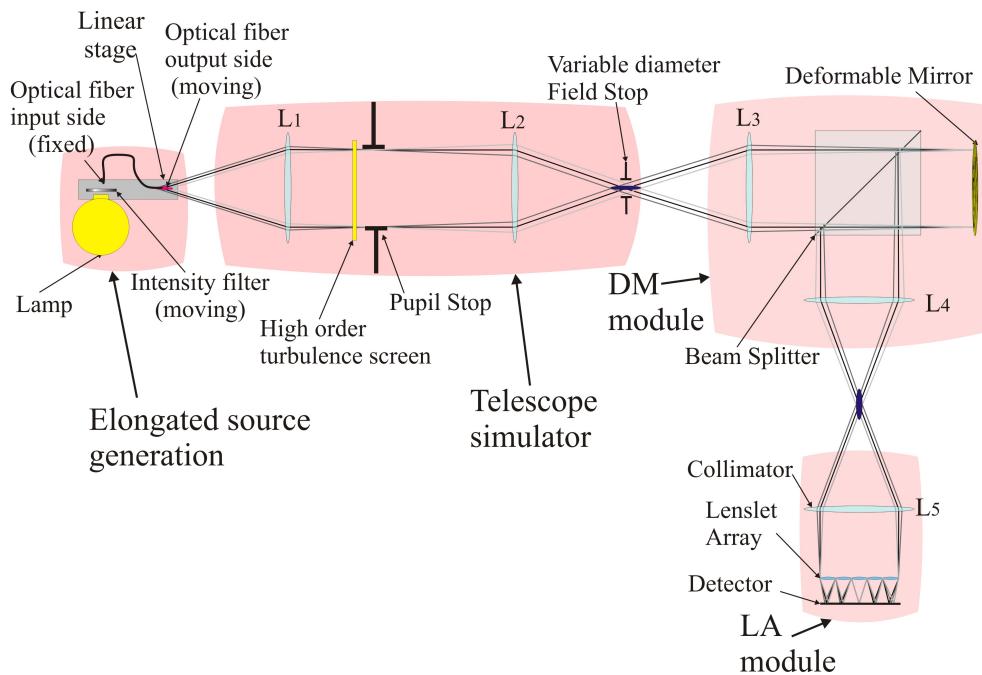
Figure 3.1: sketch showing the concept of the LGS Prototype

The conceptual design of the Prototype can be split into four parts. A modular division has been maintained also for the next phases to facilitate especially the optical alignment, to be done separately for each module.

3.1.1   Elongated source generation

The realization of an extended source was carried out by placing a 'seeing limited' size source, represented by the output side of an optical fiber, on a motorized linear stage moving along the optical axis (figure 3.1). Different positions of the source produce spherical WFs proportional to their distance respect to the collimating lens input focal point, that are seen as defocus signal by the WFS (figure 3.2). In the off-axis sub-apertures the variable defocus makes the re-imaged spots on the Detector move across the sub-apertures. By integrating the light during all the source movement, the elongated spots are formed on the Detector.

The input side of the optical fiber is fixed and it is fed by narrow band filtered light, that can be varied in intensity by means of a tunable power supply.

To realize a given intensity profile of the elongated source, between the input side of the fiber and the lamp a filter with an appropriate spatial throughput is placed (section 3.5.1). The filter, mounted on the motorized linear stage, settles the light transmissivity as a function of the source axial position, making it possible to generate the desired 'Sodium layer' profile. This solution has been chosen for its simplicity and robustness although the profile filter substitution must be done manually.
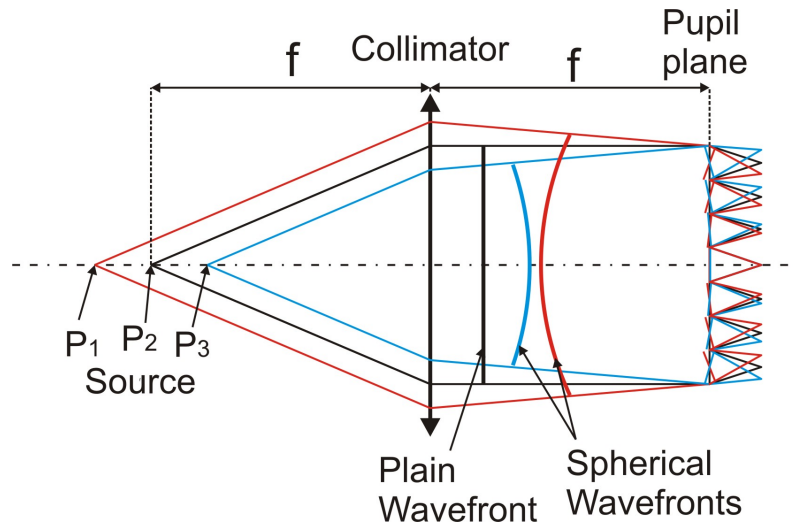
Figure 3.2: The source position is related with the spherical wavefront arriving to the pupil images that cause the spots offest in the SH sub-apertures.

3.1.2 Telescope simulator

The telescope simulator or Module 1 is an afocal system where the PS represents the telescope aperture (fig. 3.1). The lens L1 collimates the light from the source onto the PS while the next lens, lens L2, makes an image of the source and produces a telecentric output beam. The telecentricity, common feature of all the modules, yields the pupil images from the sources at different heights to overlap.

The lens L1 is chosen to have a shorter focal length respect to L2 in order to reduce the fiber movement for a given elongation of the spots (eq. 3.1), and thus also the detector integration time and the censequently light background contamination. Before the PS a phase screen (section 3.5.1) can be placed to introduce high order aberrations to the WF and simulate a static atmospheric turbulence. On the image plane formed by L2, a FS with variable aperture sets the sub-apertures FoV, to avoid light contamination among adjacent sub-apertures by means of a spot truncation (fig. 3.22).

3.1.3 DM Module

The second afocal system, Module2, is formed by the identical lenses L3 and L4 which give a unitary magnification. A BS is placed after L3. The light that passes straight through the BS arrives to the DM placed on the pupil image, while the folded light is lost. The light loss due to the BS does not represent an issue for the Prototype. The light reflected by the DM and folded by the BS is then focused by the lens L4, while the straight light is lost. The insertion of the DM in the optical path has the goal to remove the WF aberrations on the LA plane, caused by the optics and during the alignment phase or to produce a spots offset via low order aberration coefficients, a useful test of the algorithms performance. Moreover the DM can be used to dither the spots on the Camera and perform the centroiding algorithms response calibration procedure (section 3.6).

3.1.4 Collimator and Lenslet Array

The Module3 is formed by a collimator which re-images the next pupil image on the LA that focuses a spots array on the detector.

Figure 3.3: Concept of the LGS Prototype: relevant quantities used for the system dimensioning

3.1.5   Optical parameters relationship

In the figure 3.3 the optical parameters useful to calculate the Prototype dimensioning are shown. The linear spot elongation E on the Detector (fig. 2.6) depends on the linear stage travel l_{obj} over which the source is placed and it can be calculated by the formula

$$E = l_{obj} r \frac{f_2^2}{f_1^2} \frac{f_{LA}}{f_5^2} \tag{3.1}$$

where r is the distance of the sub-aperture from the center of the elongation radial pattern on the LA, f_1, f_2, f_5 and f_{LA} are respectively the focal lengths of the lens L1, L2, L5 and of the LA. From this formula the inverse relationship between the elongation and the square of lens L1 focal length can be achieved. The geometric dimension of the non elongated side of the spots on the Detector δ_{ima} depends on the source diameter δ_{obj} with the following relation:

$$\delta_{ima} = \delta_{obj} \frac{f_2}{f_1} \frac{f_{LA}}{f_5} \tag{3.2}$$

To simulate the side launch configuration of the LGS the movement direction of the motorized linear stage must be tilted by a certain angle κ respect to optical axis. The simulation of the LGS launcher placed at the side

of the telescope is realized when κ is

$$\kappa = \frac{f_1}{2D_{PS}} \tag{3.3}$$

The pupil image diameter on the DM depends on the two lenses focal lengths (excluding lens L1) that precede it in the optical path:

$$D_{DM} = D_{PS}\frac{f_3}{f_2} \tag{3.4}$$

while the pupil size at the LA plane regards all the 4 preceding lenses focal lengths

$$D_{LA} = D_{PS}\frac{f_3}{f_2}\frac{f_5}{f_4} = D_{PS}\frac{f_5}{f_2}M_2 \tag{3.5}$$

where M_2 is the Module2 magnification, chosen to be equal to 1.

For the calculation of the FS diameter equation 3.1 must be used, to find the source travel Δl_{obj} that maximize the re-imaged spot elongation without light overhang among the sub-apertures. The relation between Δl_{obj} and the re-imaged source length after lens L2 is

$$\Delta l_2 = \Delta l_{obj}\left(\frac{f_2}{f_1}\right)^2 \tag{3.6}$$

The FS must be placed on the image plane of the source position seen at infinity from the PS, called NGS position. Since after L2 the beams are telecentric, the beam size on the FS plane, coming from the source at distance Δl_{obj} respect to the NGS position, sets the proper PS diameter:

$$D_{FS} = \frac{\Delta l_2}{F_2} \tag{3.7}$$

where $F_2 = f_2/d_{PS}$

We began to play with the above formulas to have a base for the optical design phase and check the overall size of the Prototype that had to fit inside the optical bench dimension. The starting points were the Detector number of pixels and pixel size, since we had it in house, and some reasonable parameters for commercial LAs and DMs.

3.1.6   Control Software

A custom CS has been developed to control and synchronize the motorize linear stage, DM and Detector to acquire sets of images simulating the LGSs WF sensing, to be successively reduced and analyzed. Before any run of acquisitions
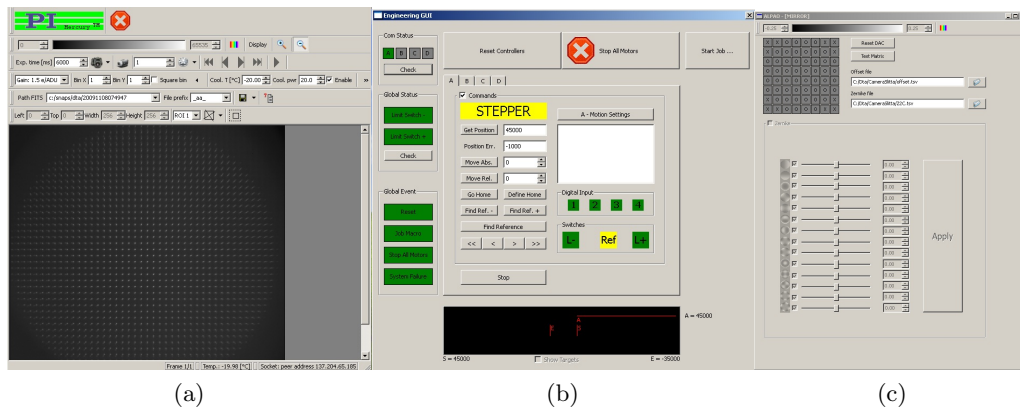
Figure 3.4: Graphical interfaces of the Prototype CS: a) main window; b) motorized linear stage engineering window; c) DM engineering window

the light source intensity must be set, the intensity filter, the high order phase screen and the FS must be properly positioned. The remotely tunable parameters (Motorized linear stage travel, DM shape, Detector binning) can be instead varied before any acquisition.

The CS is formed by two distinct programs linked by a command protocol in a TCP/IP connection (client/server socket). The server program is written in C++ and takes care of the control of the various devices and of the LGS images simulation by means of devices synchronization. The client program, written in IDL, initializes the different device parameters, starts the experimental run (commands sent to server via socket) and saves the acquired images. A typical client run is the following:

1. Open socket connection (for first image only)
2. Set Camera parameters: exposure time, dark, bias
3. Set Camera binning
4. Set DM shape
5. Set linear stage initial and final position
6. Start run
7. Linear stage moves in the initial position
8. Acquisition start (open Camera shutter)
9. Linear stage moves to final position
10. Stop acquisition (close Camera shutter)
11. Linear stage moves back to initial position
12. Repeat eventually sequence from point 2 or point 10

13. Close socket connection

14. The client receives the images to be processed

During the alignment phase an engineering version of the CS was used. We needed in fact to acquire sets of images with source placed in different positions along the optical axis and analyze the data afterwards.

3.2   Optical Design
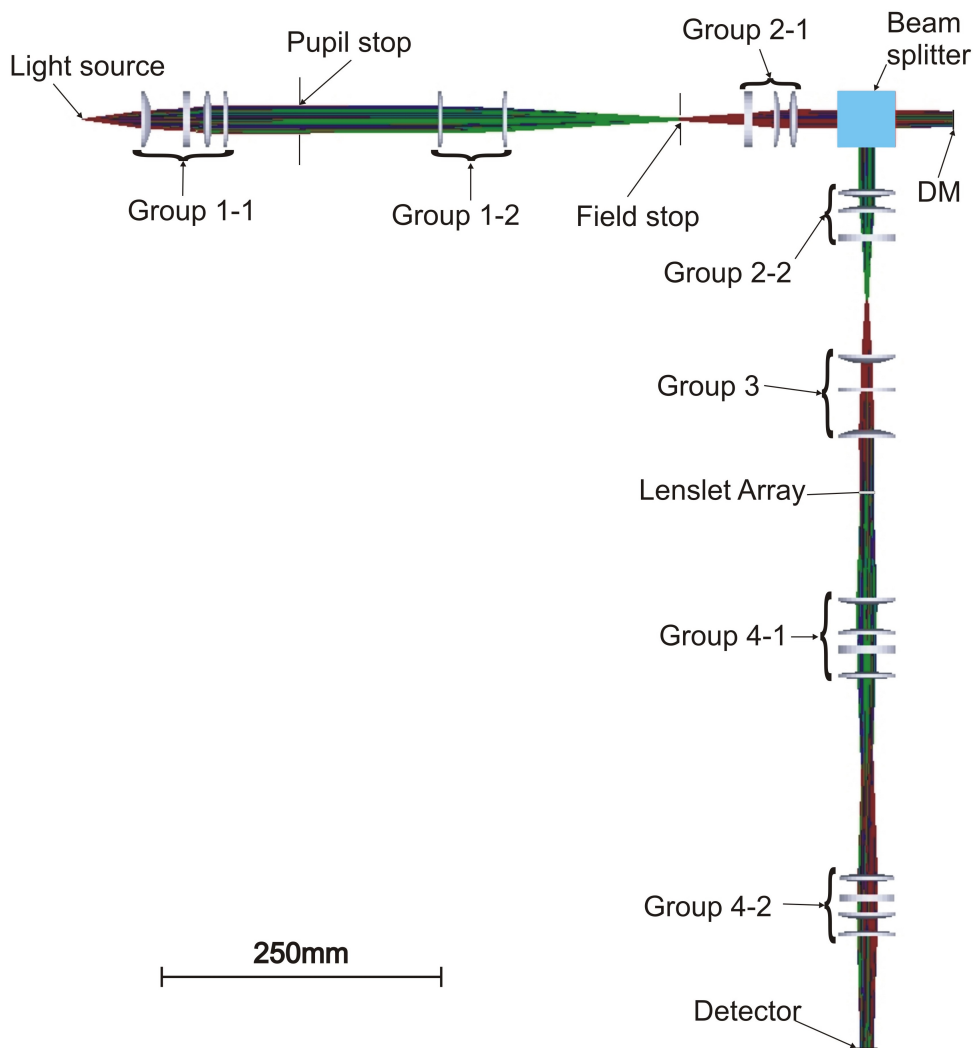
Figure 3.5: Optical design of the Prototype.

The main concern of the optical design was to combine a good optical quality in a reduced available space, the optical bench. A design that makes

use of slow working FAs produces typically a good optical quality and a general relaxation of the alignment tolerances but the overall size of the system is increased. To match both the requirements ,optical quality and allowed space, the single ideal lenses of the conceptual scheme (figure 3.1) became groups of lenses (figure 3.5). Since we worked with almost monochromatic light and thus there were no effects of chromatison to be considered all the lenses are singlets. The number of lenses composing each group depends mainly on the working FA and the FoV. The Group1-1 works at ~F/3.5 to reduce the motorized linear stage travel range (eq.3.1) and is composed by 4 lenses, that become 2 in Group1-2, due to a more relaxed F/7.5.

In the definition of the lenses number and curvature radii composing the groups, the optical quality, defined as the WF aberrations amplitude, caused by the optics, on the pupil image planes (as explained in section 3.3), was the principal merit function but not the only one. Using the Gullstrand formula for two lenses, the effective power of a lens system P_e, which is the inverse of the effective focal length f_e, is :

$$P_e = \frac{1}{f_e} = P_1 + P_2 - sP_1P_2 \qquad (3.8)$$

where P_1 and P_2 are the power of the single lenses ans s is the lenses distance. It can be understood from this equation that short focal lengths give a compact design, the other principal merit function during the optical design phase, but the optical quality is usually degraded and more lenses are needed to reach the goal.

In the optical design phase we added another afocal system, the Module4, formed by Groups 4-1 and 4-2 as shown in figure 3.5. The two reason of the Module4 insertion are: 1) the impossibility to place the Detector directly on the spots array plane formed by the LA, due to the small focal length of the micro lenses (3.85mm); 2) the requirement to match the LA pitch (300μm) with an integer and even number of Detector pixels (13μm of side dimension) per sub-aperture. A magnification of 1.04 times made by Module4 permitted to have sub-apertures with 24x24 pixels. Analogously to Group1-1, both lens groups of Module4, which work with off axis sources, required 4 lenses to achieve a satisfying optical quality.

In table 3.2 the nominal optical parameters that came out from the design are presented. From the starting points composed by the LA focal length and diameter (12mm), corresponding to 40x40 sub-apertures and the pupil image

size on the DM (14mm over 15mm of active area) we derived the other listed quantities.

During the optical design, a preliminary mechanical design was started. In fact some constraints on the distances between the optical elements, concerning the necessary clearance for the mechanical holders, had to be considered.

The optical tolerances analysis is presented in the next section while the prescription data of the optical design are listed in table 3.8.

Component	Parameter	Unit
PS	diameter	25mm
Pupil image on DM	diameter	14mm
Pupil image on LA	diameter	12mm
FS	diameter	<3.4mm
Group1-1	focal length	88.6mm
Group1-2	focal length	186.5mm
Group2-1	focal length	104.8mm
Group2-2	focal length	104.8mm
Group3	focal length	90.1mm
Group4-1	focal length	122.7mm
Group4-2	focal length	127.5mm
LA	focal length	3.85mm
	pitch	0.3mm
Source	core diameter	0.1-0.2mm
	travel[1]	~1mm for 1pixel displacement
	travel[2]	~0.5mm for 1pixel displacement
	tilt angle for side launch	~6°
[1] central launch for the most elongated sub-aperture		
[2] side launch for the most elongated sub-aperture		

Table 3.2: Nominal optical parameters of the Prototype

3.2.1 Reference axes definition

Hereafter we will refer to z axis as the direction parallel to the optical axis, x and y axes as the directions perpendicular to the optical axis and, respectively, parallel and orthogonal to the optical bench. For NGS position we mean the source placed at Group1-1 focal point which is seen at infinity by the PS, while as reference position of the soruce is intended the one that is re-imagined in the center of the sub-apertures and give a null (or the minimum value) WF measurement.

3.3   Optical quality and tolerances

The usual procedure for the tolerances analysis during the optical design phase of the AO instruments begins from the maximum allowed WFE defined in the Error Budget (section 1.1.1). Successively the tolerances for the single opto-mechanical parameters are calculated, setting the manufacturing and alignment accuracy of the components.

In the case of the Prototype we had time and cost constraints that did not permit to buy custom components with tight specifications for the optical parameters and mechanical components accuracy. We performed thus a sensitivity analysis, by means of Monte Carlo simulations, where some compensators were foreseen to overcome the construction inaccuracies of the commercial opto-mechanical components and the alignment errors.

The tolerances analysis on the optical quality regarded the residual aberrations on the LA plane and on the Detector, after the re-imaging of the spots array operated by Module4. We considered as acceptable a degradation of the optical quality that could be corrected by means of the DM shape adjustment without consuming too much dynamic range. Regarding the spots offset caused by the the WF aberrations the goal was to maintain the maximum displacement below 1/10 of pixel.

Regarding the tolerances on the pupil images sizes and blur on the DM and LA, the objective was to maintain a maximum difference respect to the nominal case below 1/10 of sub-aperture size. This tolerance did not come out from a detailed WFE calculation but it is a 'rule of thumbs' for the AO systems tolerance analysis, used also in real instruments as the Layer-Oriented WFS for MAD and LINC-NIRVANA. For 40 sub-apertures over the diameter, this tolerance is translated in an overall 1/400 of precision of the optical parameters that have a role in the pupil images size and the system telecentricity.

As explained in section 3.4, the lens groups are mounted into two independent sub-groups. One is formed by a single lens while the other is composed by the remaining lenses, assembled together inside a tube. Both sub-groups can be moved along the three reference axes and regulated in tilt respect to the optical axis. The Monte Carlo simulations made with Zemax used as tolerance operands, depending on the cases, the lens center, tilt, or position difference respect to the nominal values and the focal lengths tolerances provided by the optics constructors.

3.3.1   WFE on the LA plane

The WFE on the LA plane coming from an on-axis source is ∼250nm RMS, considering all the optics with the nominal parameters and in proper position. The WF is composed by defocus and spherical aberration that are always produced by real lenses. In the Monte Carlo simulation regarding the optical quality we gave to each single lens a reasonable tolerance value for the tilt and decenter. Considering the center of curvature tolerance and the lens holder construction accuracy we considered a conservative value of 0.2mm of decenter, while a tilt tolerance of 0.2° resulted from considerations about the wedge of lenses and holders. The sub-groups tilt and centering regulations were used as compensators, taking count also of the positioning accuracy of the stages. We used as merit function the direction of the beam after the lenses, to be of the order of the measurement accuracy during the alignment phase (section 3.5.2). The simulation resulted with a reasonable value of WFE of ∼450nm, averaged over all the realizations, the main contributions being tilt and astigmatism, thus able to be corrected by the low order DM.

Different source positions along the z-axis respect to the NGS one introduce, apart the desired defocus that produces the spot elongation of the spots (figure 3.2), a peculiar spherical aberration depending on the position, impossible to be compensated by the DM.

Moreover the side launch configuration makes the source to work a little off-axis and other low order modes contribute to the WF aberration on the LA plane. In table 3.3 we present the aberration coefficients in the center of the source (position P2) and at the two edges of the stage travel (positions P1 and P3, explained in figure 3.2).

		WFE RMS (μm)				
Zernike mode		tilt	defocus	astigm	coma	3rd spherical
	P_1	0.14	-13.92	0.18	-0.03	0.21
Source Position	P_2	0	-0.24	0	0	0.15
	P_3	-0.17	13.79	0.19	-0.06	0.08

Table 3.3: Aberration coefficients form the source in three different z positions, described in fig. 3.2.

3.3.2   Module4 Optical quality

The Module4 makes an image of the spots array from the LA focal plane to the Detector with a magnification factor of 1.04. The tolerance analysis on this module has been carried on for three requirements: re-imaged spots optical quality, field distortion and magnification factor.

The calculations for the expected WFE after the alignment phase followed the same procedure described in section 3.3.1, i.e. by simulating plausible values for the lenses center and tilt positioning uncertainties and using the corresponding stages as compensator. The tolerance analysis results are shown in the upper figure 3.6: the geometric spot sizes from the on axis and other 8 off-axis point size source positions are re-imaged on the Detector and fit always inside the diffraction limit circle. No image size enlargement is produced by Module4.

The grid distortion analysis was performed by calculating the re-imaged spots offset respect to the sub-aperture centers, coming from a regular grid of sources placed at the input focal plane of Module4. The lower figure 3.6 shows that these spot displacements, seen as local slope signals, introduce only low order modes, that can be removed by the DM as NCPAs or, for the case of TT, by shifting the Detector on its plane saving dynamic range of the DM.

The magnification factor of Module4 depends on its lens groups focal length ratio. A difference respect to the nominal value is translated into a spots offset proportional to the sub-aperture distance from the optical axis, hence a defocus signal. The maximum allowed magnification factor error has been chosen to produce a spots offset of 2 pixels in the edge sub-apertures, that means 0.2% of tolerance. The WF aberration resulting from this error can be removed by applying about 3μm RMS of defocus by the DM or moving the source of 0.6mm along z, applying in this way an inverse defocus signal to the pupil planes (section 3.1.1) .

3.3.3   Pupil images size

The two pupil images diameters (at the DM and LA planes) depend on the focal length of the preceding lens groups as shown in the equations 3.4 and 3.5. Group1-1 focal length does not enter this calculation and it is discussed later, so we used the other 4 lens groups in the tolerance analysis. The nominal pupil size on the DM, 14mm over 15mm of active area, was chosen
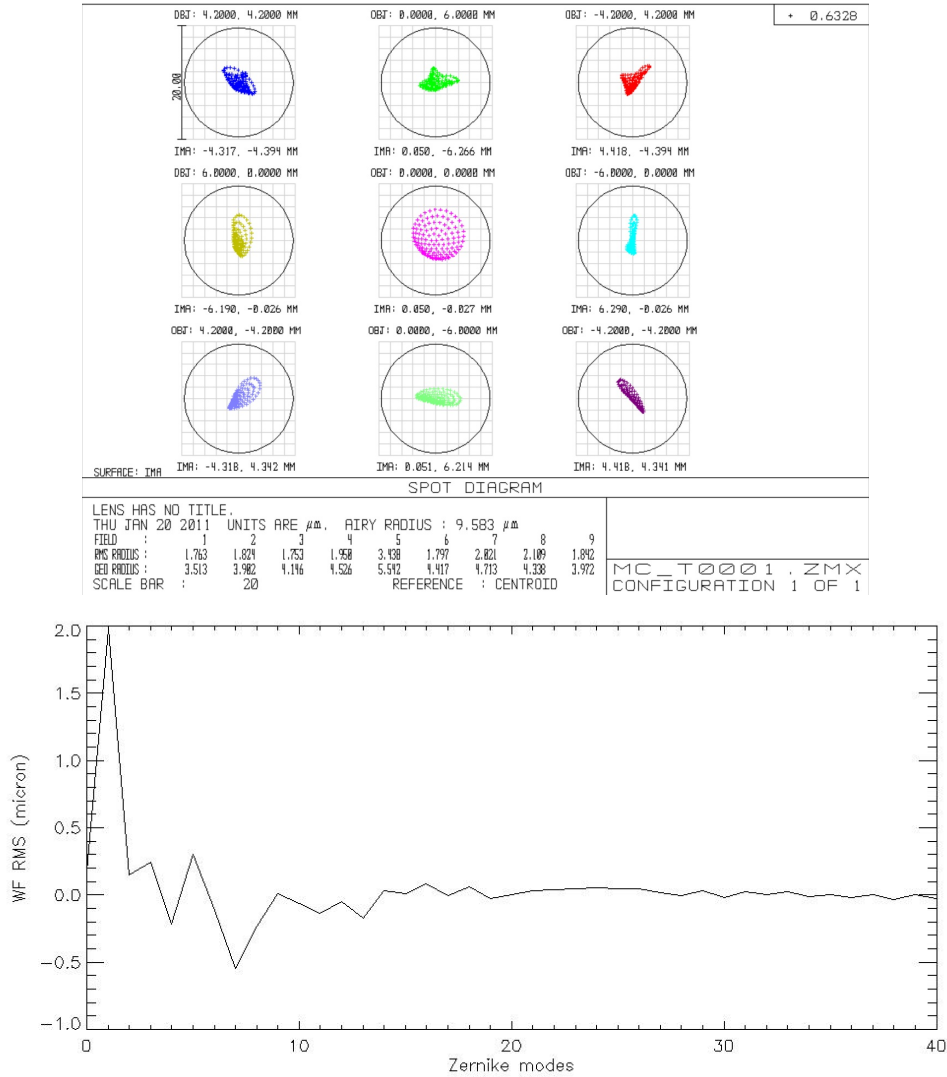
Figure 3.6: Tolerance analysis of Module4. Upper figure: optical quality of the spots after the re-imaging of the spot array; lower figure: aberrations introduced to the system after the Module4 alignment procedure resulted in one of the realizations during tolerance analysis. The plot is indicative to show that only the low order modes have a significant value.

to avoid edge effects when applying a certain shape and it is not a critical value, 0.1mm of tolerance in diameter could be accepted; contrariwise the pupil size on the LA has the above described 1/10 of sub-aperture size of maximum difference respect to the LA diameter. In the tolerance analysis for the pupil image dimension on the LA we considered as uncorrelated the single components errors, Group1-2 focal length, Group3 focal length and Module2 magnification, that is the ratio between the focal lengths of the Group2-1 and Group2-2. We assigned them the total error, 1/400 respect the pupil

size nominal value, divided by the square root of the number of elements, leading to a 1/600 of tolerance for these parameters. Considering 0.1mm for the manufacturing accuracy of the custom spacers that separate the lenses inside the tubes (fig. 3.8) and a tolerance of 1/100 for the commercial lenses focal lengths, the simulation resulted, in the worst case, to 1/65 of maximum focal length difference after the positioning of the lenses in their holders. Anyway this error can be compensated operating in the sub-groups mutual distance, by means of the linear stage, with a shift along the optical axis of 1.5mm. Taking count also of the stage positioning accuracy of ±0.02mm, we could expect a groups focal length accuracy of the order of 1/1000, well inside the requested tolerances. For the pupil image size on the DM, the Group2-1 focal length can have more relaxed specifications, remembering that an equal variation of the Group2-2 focal length must follow.

3.3.4   Group1-1 focal length and position

The Group1-1 focal length affects the spots dimension and elongation on the Detector, as it can be seen in equations 3.2 and 3.1. It is not a critical parameter and an error of 1/200 is considered acceptable since such a variation on spot size is quite negligible.
A mis positioning of the PS, not on the Group1-1 focal point, brings a non linear dependency between the distance of the source from the NGS position and the correspondent spot position on the Detector respect to the reference one. This effect has been described in section 2.1.3 and implies that the source intensity profile is different from the re-imaged post intensity profile. Anyway it is quite small for the Prototype and a tolerance of 1mm in the distance Group1-1 to PS does not introduce relevant profile differences.

3.3.5   Source size

As presented in table 3.3, the WF aberration mode having the maximum amplitude on the LA plane is the defocus term ($\pm26\mu$m RMS), when the source is at the edge positions of the linear stage travel for the elongated spot generation. In a single sub-aperture this value must be divided divided by the number of sub-apertures over the diameter. The local defocus affecting the LA micro-lenses shifts the sub-aperture image plane of a maximum value ~0.04mm along z, respect to the nominal image plane position, less than the

focus depth of F/12.8 focusing beams. The spots on the LA image plane, coming from a point size source, have thus always a geometrical diffraction limited size, as the ones re-imaged by Module4 on the Detector (figure 3.6). For these reasons the real spots size on the Detector, from the source in a fixed position, is the result of the convolution of the source diameter with a diffraction limited PSF defined by the LA micro lenses size. Considering both the source and the PSF with a Gaussian profile, the spot dimension δ_{ima} is the geometrical value δ_g, calculated following eq.3.2 and using the optical values of table 3.2, summed in quadrature with the PSF size δ_{PSF}:

$$\delta_{ima} = \sqrt{\delta_g^2 + \delta_{PSF}^2} \tag{3.9}$$

A source with a core diameter of 0.2mm is re-imaged on the Detector as a spot size having 2 pixels of FWHM.

3.3.6 Telecentricity

The telecentricity of the beams produces the overlapping of the pupil images from sources in different z-positions, since the pupil image diameter is calculated by dividing the collimating lens focal length by the arriving beam $F_\#$. The system telecentricity depends on the proper position of the elements placed on the pupil planes, that must coincide with the lens groups focal points. In the calculations to find the alignment tolerances on the telecentricity the position of the the group of lenses were the variables and the adjustment of their distances respect to the PS, DM or LA the compensators. The results shown that the limit blur of the pupil images (1/10 of sub-aperture) was reached with a positioning error of 0.12mm, correctable by means of the linear stages, whose accuracy of 0.02mm makes this alignment procedure absolutely feasible.

3.3.7 Modules positioning

The various modules were foreseen to be aligned independently (section 3.5.2) and be integrated together to form the final configuration of the Prototype. The output focal plane of a module had to coincide with the input focal plane of the subsequent one, otherwise a defocus signal would have affected the WF on the LA plane, to be compensated by a fiber shift or by the DM. The smaller FA of the Group1-1 respect to the other lens groups of about a factor 2 makes

anyway the defocus compensation, by means of the fiber shift along z, to be 4 times smaller than the positioning error value. This permitted to accept a positioning tolerance of about 2mm to be compensated by 0.5mm of source shift.

Differently, the Module4 had to be positioned with a bigger accuracy since, to avoid the enlargement of the re-imaged spots size on the Detector, its input and output focal planes were required to be positioned at distance respect to the the spots array plane below the depth of focus. The correct positioning was achieved during the alignment phase by minimizing the measured spots FWHM.

3.3.8   Field Stop alignment

As presented in section 2.1.3, a FS is foreseen in an LGS WFS to avoid the signal contamination in the adjacent sub-apertures. The low order NCPA introduced by the truncation of a variable intensity profile extended source (section 2.1.3) is one of the LGS issues to be studied with the Prototype. For this reason we did not want to introduce the same effect due to a not accurate alignment of the FS.

The FS position along the z-axis sets the sub-aperture FoV center. A displacement of 1/10 of pixel for the FoV center respect to the sub-aperture center was chosen as tolerance. The length of extended source l_{obj} is re-imaged on the image plane where the FS is placed with a length l_2 (figure 3.3). A spot elongation E of 1 pixel on the Detector, in the sub-aperture having the biggest elongation for the side launch configuration, corresponds to l_2=2.3mm. Thus the tolerance of 1/10 of pixel can be achieved with ∼0.2mm of accuracy in the FS axial positioning.

The FS decentering respect to the optical axis causes instead the spot truncation to be not symmetric for sub-apertures at the same distance to the spots array center. We took 1/30 of FS diameter as centering tolerance which corresponds to about 0.1mm of centering tolerance. The FS diameter to have 22 pixels of maximum spot elongation, over 24 pixels of sub-aperture side, is 3.4mm (eq. 3.6 and 3.7) and the proper diameter value tuning was performed during the alignment phase. Test requiring a different spot truncation require the FS diameter to be changed manually.

3.3.9   Tolerance analysis summary

We summarize the results of the tolerance analysis, reminding the values of 1/10 of sub-aperture as the allowed pupil difference in size or mis positioning respect to the nominal values and 1/10 of pixel as the maximum spots displacement respect to the sub-aperture centers. The correction of the residual WFE below the tolerances must be achievable by means of the compensators, composed by the linear and tilt stages, the DM shape and the source position.

Optical quality:

- from the alignment of the optics respect to the optical axis a WFE of ∼450nm RMS on the LA plane can be expected, to be compensated by the DM;

- the different positions of the source causes a differential WF on the LA plane shown in table 3.3. This effect varies the spots shape and can not be compensated;

- after the Module4 alignment the re-imaged spots are diffraction limit and the low order aberrations produced by the optics can be compensated by the DM;

- an erroneous magnification factor of Module4 produces a defocus signal, to be compensated by means of the source shift along z;

Pupil images size:

- the construction and alignment tolerance of the lenses vary the focal lengths of the lens groups defining the pupil images size. This error can be overcome by means of the tuning of the sub-groups mutual distance;

Group1-1 focal length:

- it affects the re-imaged spots size in both directions (elongated and non elongated side) but it does not appears as a critical value;

Telecentricity

- requested for the pupil images overlapping from sources at different positions along z, the specifications on the telecentricity is reached by moving the group lenses along the optical axis;

Modules positioning:

- a mis positioning of the modules 1,2 and 3 produces a defocus signal to be compensated by means of the source shift;

- the positioning accuracy of Module 4 must be below the spots array focal depth. It is checked by measuring the spots FWHM;

FS positioning:

- a mis positioning causes low order NCPA aberrations.

In table 3.4 we present the detailed alignment tolerances for the various elements

Tolerance	Unit
Group4-1 f_l	±1mm
Group4-2 f_l	±1mm
Module4 magnification	±0.1%
Module1 - Module position	±1mm
Module2 - Module3 position	±1mm
Module4 - LA focus position	±0.05mm
Detector plane position	±0.05mm
FP position	±1mm
FP centering	±1mm
PS to Group1-2 distance	±0.5mm
Group2-1 to DM distance	±0.16mm
DM to Group2-2 distance	±0.16mm
Group3 to LA distance	±0.13mm
Group4-1 - Group4-2 distance	±1mm
Group1-1 f_l	±0.2mm
Group1-2 f_l	±0.31mm
Group2-1 f_l	±1mm
Group2-2 f_l	±1mm
Group3 f_l	±0.37mm
Module2 magnification	±0.1%

Table 3.4: Alignment tolerances

3.3.10   Requirements on compensators

The tolerance analysis presented in this section foresees some compensators to retrieve the optical quality during the alignment phase. In the following the compensator requirements are presented.

Lens centering respect to the optical axis:±0.2mm
Lens tilt adjustment: ±0.2°
Source centering: the off-axis positioning of the source produces a tilt signal. If Δ_{obj} is the source distance from the optical axis, the

displacement Δ_{ima} of the spots respect to the center of the sub-apertures, similarly to eq. 3.2, can be calculated as:

$$\Delta_{ima} = \Delta_{obj} \frac{f_2}{f_1} \frac{f_{LA}}{f_5} \qquad (3.10)$$

where the operands, defined in section 3.1.5, have their dimensions listed in table 3.2. The accurate removal of the tilt signal is performed by means of the DM or by the Detector displacement along the image plane. The requirement of <1 pixel of spots displacement due to the source decentering can be reached for Δ_{obj} <0.2mm.

Source axial positioning: the source shift along the optical axis is used to remove the defocus signal introduced by an erroneous positioning of the modules during their integration together (section 3.5.3). A source positioning accuracy of 0.2mm produces the maximum allowed spots offset of 1/10 of pixel.

LA grid alignment: The alignment between the LA grid and the Detector axes, defined by the pixel columns and lines, of 1/10 of pixel can be achieved by $\sim$20arcsec of rotation accuracy of the LA along z.

DM tilt accuracy: the mean value of the spots offset on the Detector (TT signal) can be removed by means of a tilt of the DM. An accuracy of 250nm RMS in the tilt signal is sufficient to place the mean value of the spots centroids below 1/10 pixel of distance respect to the reference positions

DM defocus accuracy: The removal of the residual defocus can be achieved by a Defocus signal accuracy by the DM of $\sim$150nm RMS.

3.4   Mechanical Design and Hardware components
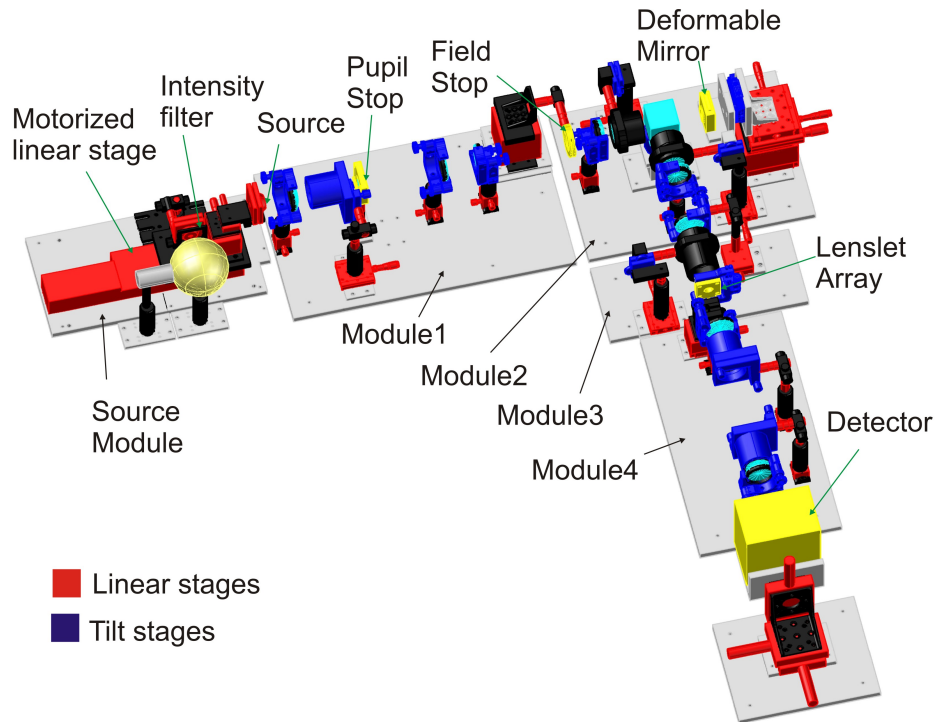
Figure 3.7: 3D view of the mechanical design of the prototype. The red components are the translation stages while the blue ones are the tilting ones, both used during the optical alignment. The yellow components represent the key elements of the Prototype: PS, FS, DM, LA, Detector

The mechanical design was carried out taking care of the tolerance analysis described in section 3.3, particularly regarding the compensators foreseen by the tolerance analysis. For this reason all the components (lens groups, DM, Detector, optical fiber, etc.) were mounted on positioning and tilt stages, in order to accurately position and align all the optical elements within the tolerances and match the estimated optical quality. In figure 3.7 the mechanical design of the Prototype is presented. The components drawn in red are the position regulations and the blue elements are the TT adjustment stages. The split of the Prototype into modules had the objective to allow their internal alignment independently.

Each lens group, that substituted the single lenses during the optical design phase, is split into two sub-groups to be aligned and moved separately, as shown for Group4-2 case in figure 3.8. One lens is mounted alone on an holder having the required adjustment stages while the remaining lenses are
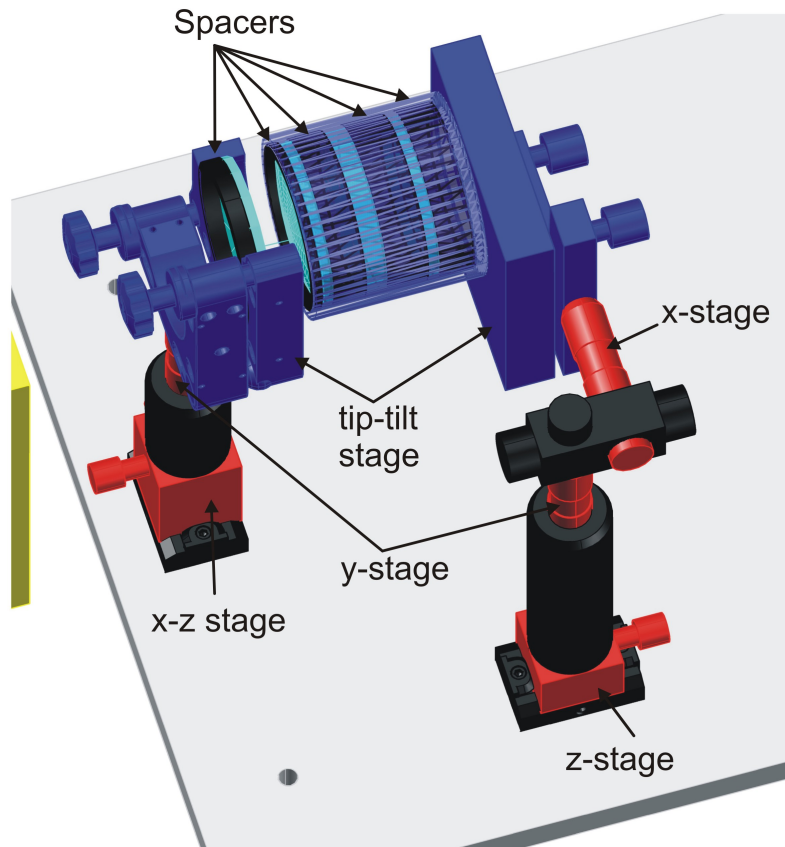
Figure 3.8: Mechanical design of the Group4-2. The spacers set the proper distances between the lenses and avoid the contact glass-metal with the holders and tube caps. The translation and rotation stages permit the alignment and the adjustment of the focal lengths and global position of the groups, to overcome the construction opto-mechanical error of the components as explained in section 3.3.

assembled together inside a cylindrical tube, their mutual distances settled by custom plastic rings of proper thickness. Some sub-group, as the one formed by the 3 lenses in fig. 3.8, have a cantilevered mount, since the centering along the x-axis is performed by commercial (and cheap) translating optical posts. Anyway the mechanical components are attached to the optical bench and are not subjected to any variable flexure after the alignment phase or drastic temperature variations, that would produce a lenses misalignment.

The tolerance analysis demonstrated that the splitting into two sub-groups was sufficient in terms of optical quality. The distance of the sub-groups defines the effective focal length of the group (eq. 3.8), so it can be tuned during the alignment procedure to achieve the correct value. Moreover the two sub-groups

can be moved by the equal quantity in the same direction along z, to match their focal point to the planes where the PS, DM or LA are placed.

Due to the short timescale for the Prototype development we chose, when possible, only commercial components for lenses holders and stages. The non standard components, like the PS, some holders, the base plates and the plastic rings between the lenses were manufactured in the mechanical workshop of OABo.

We present the mechanical design of the different modules highlighting the principal features.

Source generator module
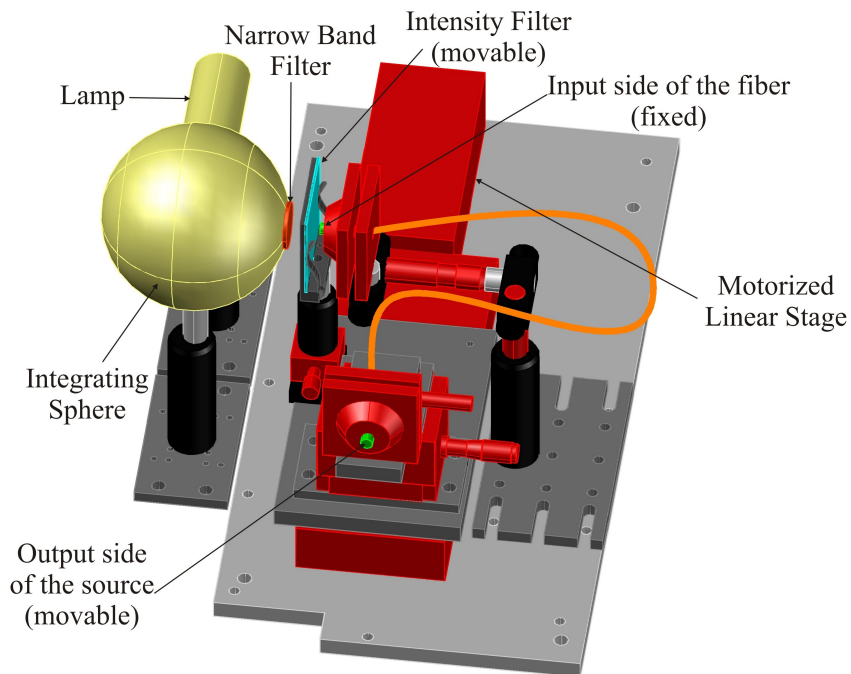
Figure 3.9: 3D design of the source generator module

The light intensity of the lamp placed inside a cylindrical tube is set by a power supply (fig. 3.9). The light enters into an integrating sphere to supply an uniform light intensity over the FA required by the source. The output hole of the sphere is covered by the narrow band filter that transmits the light at $\lambda = 632 \pm 10$nm. The intensity filter (section 3.5.1) is placed on the motorized linear stage to provide the desired profile of the elongated source and can also be shifted manually along the optical axis by means of a linear stage, to match the profile with the source 'altitude' range. The stage travel range (100mm) is

by far longer than the required source travel while the its maximum velocity permits to complete an acquisition in about 3s (section 3.1.6). Both sides of the optical fiber can be adjust in position along the three axes. Table 3.5 shows the linear stage and optical fiber main parameters.

Component	Company	Parameter	Value
Linear stage M404.42S	PI	Travel range Resolution Min incr motion Max velocity	100mm 0.16μm 0.2μm 3mm/s
Optical BLF37-200	Thorlabs	Core Diam NA	0.1,0.2mm 0.37

Table 3.5: Main parameters of the motorized linear stage and of the optical fiber.

Module1
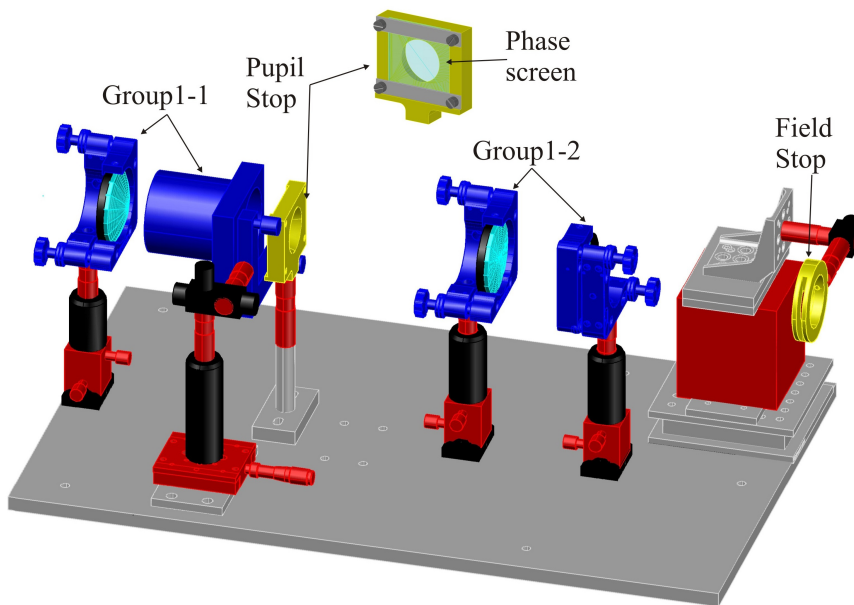
Figure 3.10: Module1 mechanical design

The short distance between the last lens of Group1-1 and the PS requires a cantilever mount of the sub-group (fig. 1.10). The PS mount is custom made piece. The drill setting its diameter has a conical profile to avoid reflections inside the hole from the non collimated beams from the sources in different positions respect to the NGS one (fig. 3.2). The FS can be moved along the three axes and its diameter must be regulated manually.

Module2
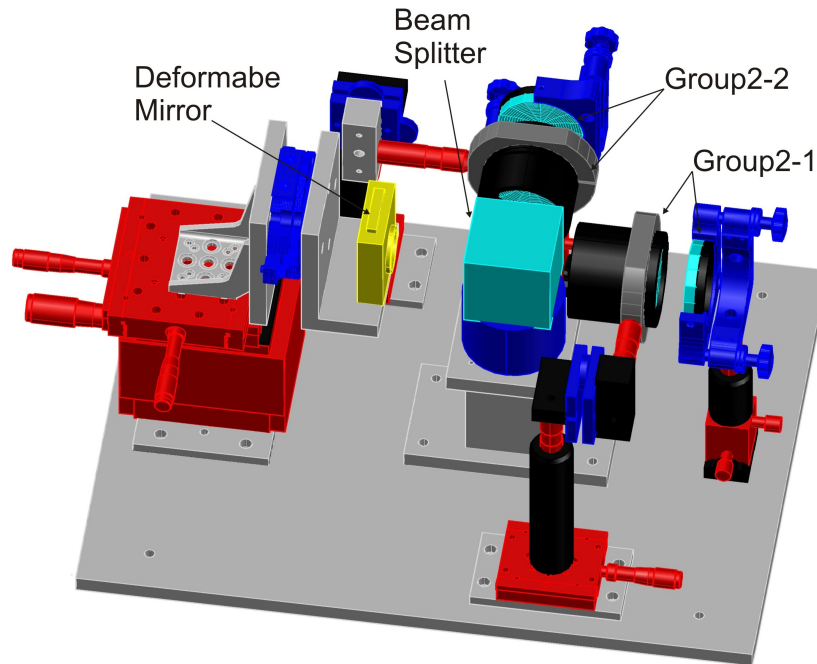
Figure 3.11: Module2 mechanical design

The presence of the BS between the lens groups and the DM makes this module quite crowded, with little clearance between the various elements. As explained in the final part of the optical design section, we started a preliminary mechanical design to check the necessary clearance among the commercial mechanical components. In this case the tilt regulations of the two tubes had to be placed off-axis, above the linear stage for the sub-group movement along the z direction (fig. **??**). Table 3.6 presents the main parameters of the DM. The big TT stroke permits to achieve the calibration procedure of the centroiding algorithms (section 3.6.2) by means of a spots offset.

Component	Company	Parameter	Value
DM	ALPAO	Pupil diam	15mm
52-v2		# of actuators	52
		Pitch	2.5mm
		TT stroke	$\pm50\mu$m
		inter act stroke	$\pm1\mu$m
		Best flat	5nm (rms)
		Linearity	$> 95\%$

Table 3.6: Main parameters of the DM.

Module3
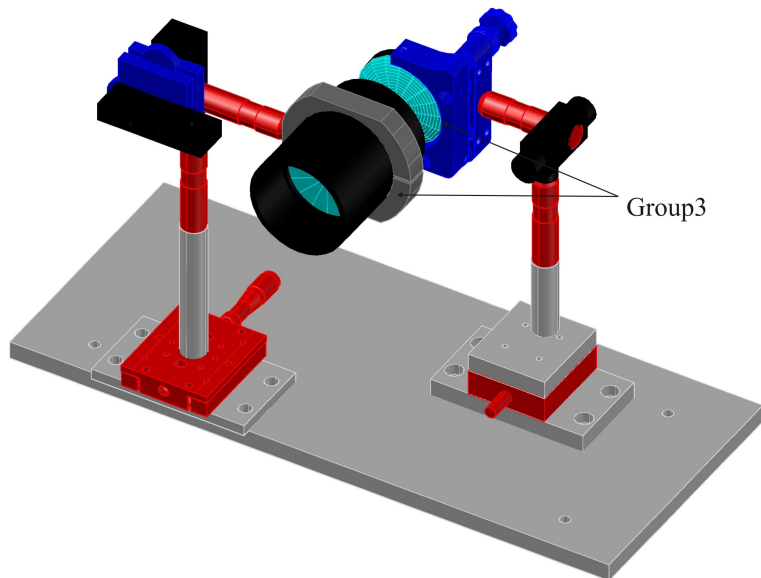
Figure 3.12: Module3 mechanical design

The Module3 is formed by the collimator (fig. 1.12). We choose to place the LA on Module4 since its alignment required anyway a re-imaging of the spots array on the Detector, easier to be produced by using directly Module4.

Module4
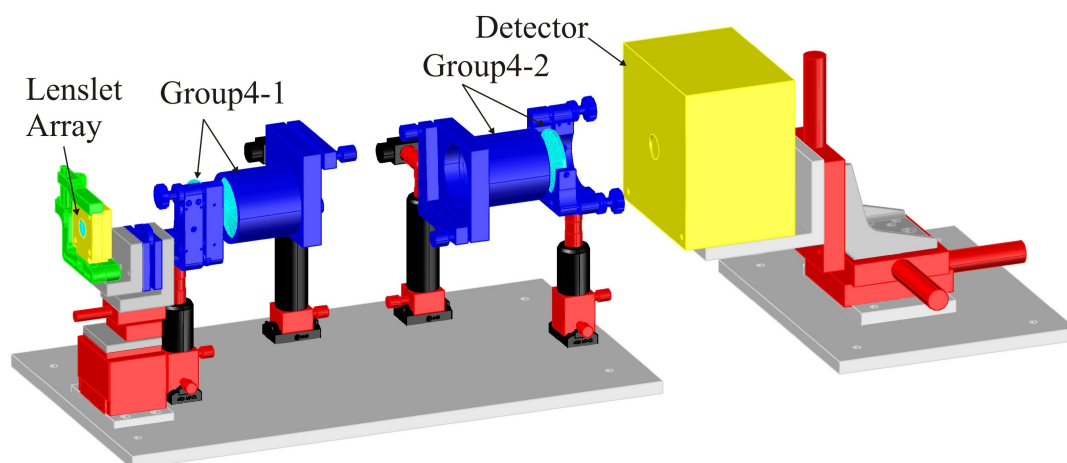
Figure 3.13: Module 4 mechanical design

The LA is contained inside a custom holder. In addition to the centering

and tilt regulations the LA is foreseen to be rotated about the optical axis, in order to align the lenslets to the detector axes (green component of figure 3.13). The Detector is mounted on an independent base plate to be used during the internal alignment phases of the different modules. The main parameters of the LA and Detector are listed in table 3.7.

Component	Company	Parameter	Value
LA APO-Q	AμS	Surf shape Pitch Focal length Area	plano-convex 300 3.85mm 15x15mm
Camera Marconi CCD4710b	DTA	Pixel size Dimension A/D conversion RON Binning Gain Dark Current	13x13 μm 1055x1026pix 16bit unsigned $11e^-$/px * 2x2 to 8x8 $0.84e^-$/ADU * $0.6e^-$/sec *
* @ -20 ^oC			

Table 3.7: Main parameters of the LA and of the Detector

3.5   AIT

In this section we describe all the phases of the Prototype AIT, started with the procurement of the optics and mechanics and the manufacturing of the non standard mechanical pieces in the workshop. The critical components have been characterized, the modules aligned internally and after, put together to form the final set up. Finally we configured the Prototype in order to make it able to simulate properly the LGS features of a SHWS.

3.5.1   Characterization of the components

(a)   (b)
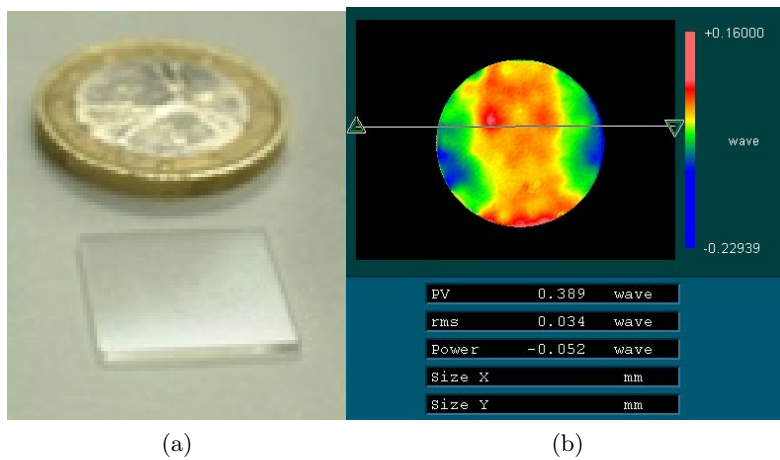
Figure 3.14: a: picture of the LA having 50x50 sub-apertures with 0.3mm pitch; b: interferogram of the best flat shape of the DM WFE.

We decided to characterize the parameters of the principal components of the Prototype that had an impact in the tests or during the alignment phase. The Detector RON measurement, for example, permitted to set the proper flux of the source in order to have the same values of SNR of the simulations, where the expected (or hoped) photon flux from the LGSs and the Detector RON were used. The LA lens grid dimensions and regularity were measured to check the construction accuracy. The mis position of the center of curvature of the micro lenses could cause offsets of the re-imaged spots positions on the Detector respect to the sub-aperture centers, producing high order aberrations on the measured WF. This systematic effect could be characterized but not corrected by the low order DM. The DM shape was measured with an interferometer (fig 3.14b) and we could verify the linearity of the applied modes and recorded the best flat DM shape to be used when the DM was mounted on its module

(section 3.5.3).

In the following we describe the custom components characterization.

Intensity filter

The intensity filter concept (section 3.1.1) must simulate realistic Sodium
profiles as the ones presented in figure 2.8. We chose a simple and robust
solution that was to print the desired profiles along the motorized linear stage
movement direction on transparent plastic screens; a picture of a bi-modal
screen is presented in the upper figure 3.15. The comparison between the
desired intensity profile (solid line) and the measured transmissivity of the
printed screen (dashed line) is shown in the lower figure 3.15. The printed
profile follows in shape the theoretical curve, the difference in intensity is a
function of the printed Grey intensity and it was taken into account for the
successive filters generation.
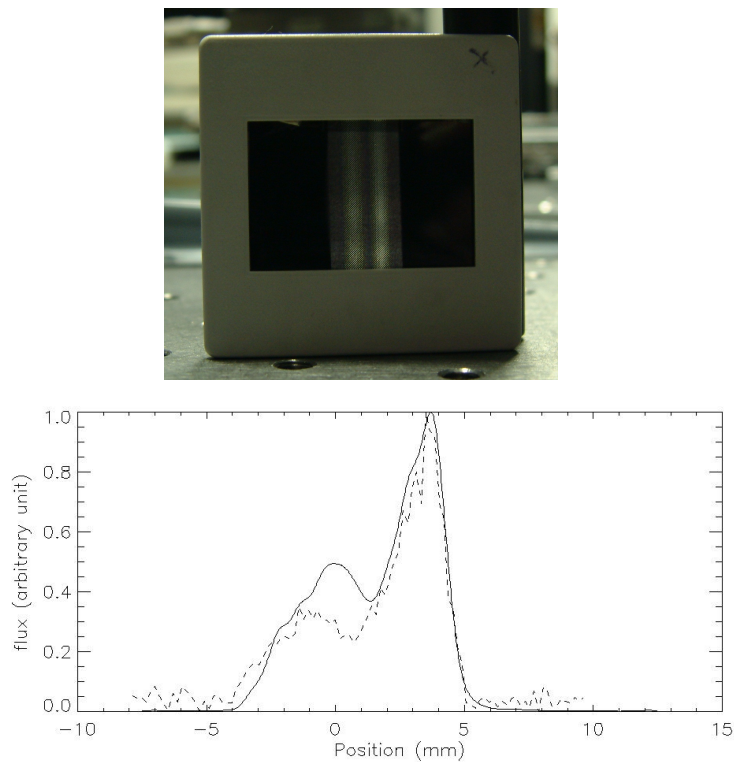
Figure 3.15: upper figure: picture of a filter with bi-Gaussian intensity profile;
lower figure: comparison between a simulated bi-Gaussian profile (solid line
curve) and the measured intensity if the printed profile.

Phase screens
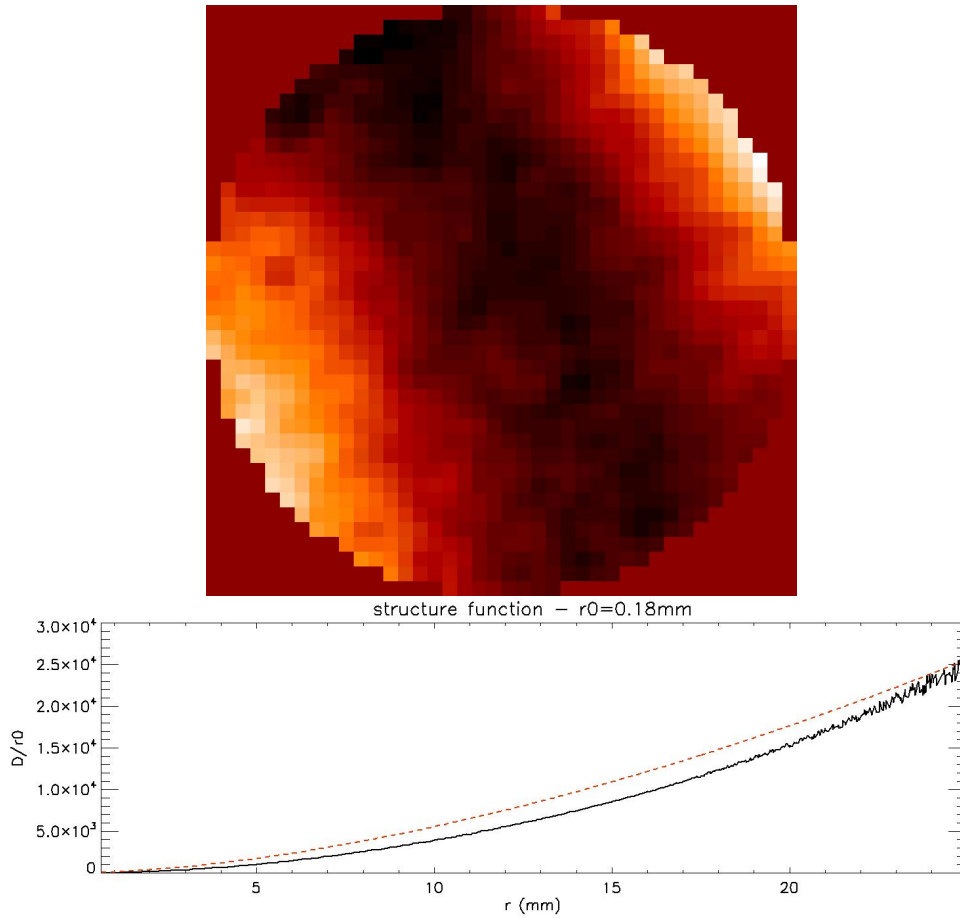
Figure 3.16: up: phase map of a plastic phase screen used to simulate the atmospheric turbulence; bottom: structure function of the screen (solid line) compared with the theoretical Kolmogorov curve (dashed line).

The static atmospheric turbulence is simulated by means of plastic screens over which a laquer-spray was deposited, following the procedure described in (Thomas, 2004). Since this procedure is quite empirical, the achievement of a screen reproducing sufficiently well the atmospheric turbulence features, suitable for our requirements, took several attempts. The phase measurements of the screens were done by using the Prototype itself. From the slopes offset in the sub-apertures we reconstructed the phase map (upper figure 3.16). The turbulence strength was measured by the phase structure function that, for the phase function ϕ with a position vector r, is

$$D_f(r) = \left\langle |\phi(r+l) - \phi(r)|^2 \right\rangle \tag{3.11}$$

where l is a displacement vector and brackets $\langle \rangle$ represent an ensemble average. For the Kolmogorov model of the atmospheric turbulence phase the structure function of the phase is (Hardy, 1998)

$$D_\Phi(r) = 6.88 \left(\frac{r}{r_0} \right)^{5/3} \tag{3.12}$$

The measurement of the structure function of the screen is shown in the lower figure 3.16. The fitting of the data with the Kolmogorov's theoretical curve produced a coherence length r_0 (eq. **??**) of 0.19mm, corresponding to 0.15m considering a sub-aperture size of 0.5m

3.5.2   Modules integration

The alignment accuracy of the modules composing the Prototype was subjected to the tolerances listed in table 3.4. The reference optical axis was determined by a collimated laser beam, parallel to the optical bench plane, that could be varied in diameter by means of an iris diaphragm. The lenses and lens groups alignment was done by minimizing the transmitted beam deviation respect to the optical axis, which is the lens centering procedure, and maximizing the overlap on a diaphragm placed before the optics of the spurious reflections and Newton's rings produced by the laser beam reflected by the lenses surfaces, which is the lenses tilt regulation procedure (Smith, 2000).

The modules alignment consisted basically on the adjustment, when required, of the focal plane positions, the lens groups effective focal lengths, the modules telecentricity and magnification. A brief explanation of the procedures used to determine these parameters is now presented, showing also that these measurements were sufficiently accurate to achieve the tolerances requirements presented in section 3.3.

Focal plane position and focal length measurement

A laboratory CCD is centered respect to the laser beam, defining the output focal plane nominal position of the lens group. The CCD is mounted on a linear stage moving parallel to the optical axis. The optics (single lens or group of lenses) are aligned in centering and tilt with respect to the laser. The measurement of the focal planes positions and of the focal lengths was not enough accurate when using as observable the spots dimension at the different

the z positions of the CCD since the required accuracy was smaller than the measurement accuracy. So we chose to follow another procedure. A plate with 2 holes at known distance D is placed perpendicular to the optical axis before the optics, letting pass only two small beams that crossed the lenses off-axis and converged at the lenses group focal plane (figure 3.17a). The difference between the actual focal plane and the CCD plane can be calculated. The measurement of the distance of the two spots as a function of the CCD position along z determines the working $F_{\#}$. This value, multiplied by the holes distance D, gives the effective focal length. If δ_d is the centroiding precision of the spot on the CCD, the error in the focal point position is

$$\delta_f \sim \delta_d atan\left(\frac{D}{f}\right) \tag{3.13}$$

For D=6mm, δ_d=1pix (8μm for the laboratory CCD) and taking the shortest focal length f of table 3.2 (f=88.6mm), the result is a measurement accuracy of the focal point position below 0.01mm, within the tolerances. The accuracy in the focal length measurement is $\delta f/f$, using the above parameters it results below 1/1000.
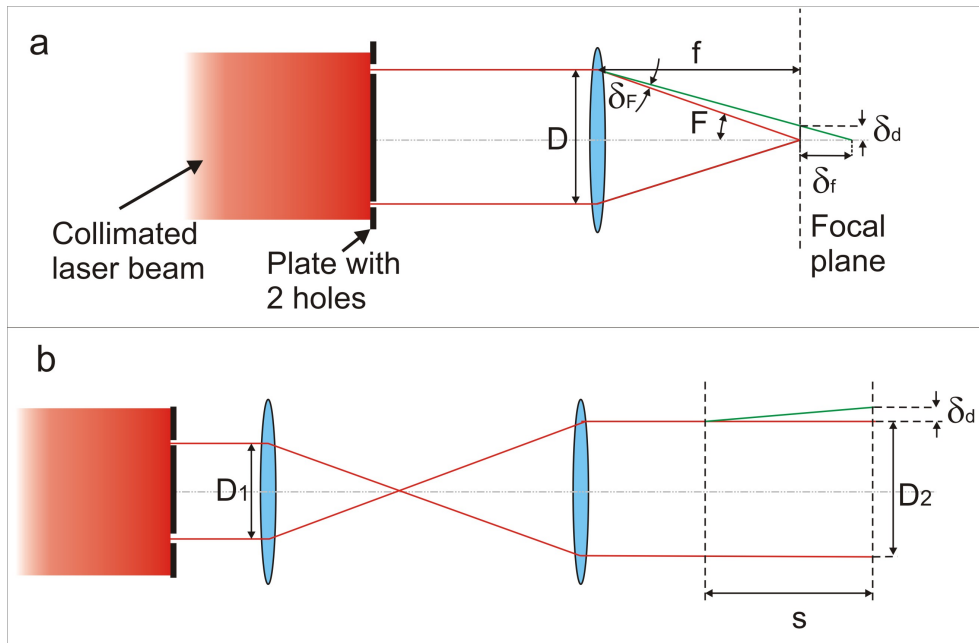
Figure 3.17: sketch illustrating the procedures used to check the optical parameters measurements and accuracies during the modules alignment.

Telecentricity and modules magnification measurement

The two lens groups of a certain module are aligned respect to the optical axis, the group that focuses the beam (Group1-2, Group2-2 or Group4-2) already settled regarding its effective focal length and positioning respect to the CCD, as explained in the above procedure. A plate with 2 holes of known distance D_1 is placed before the module and let pass only two small laser beams (figure 3.17b). The distance D_2 between the two spot centroids is calculated after passing the two lens groups. The system telecentricity is reached when this distance does not change as a function of the CCD position along z. At this point the module magnification, that is the ratio between the distance of the holes and the corresponding spots on the CCD can be calculated. The telecentricity measurement accuracy is $\delta d/s$ where δ_d the centroiding precision of the spot and s is the CCD shift between two measurements. The tolerances requirement is reached for $s \geq 10$mm, $\delta_d = 1$pixel and $D_2 \geq 7$mm corresponding to a magnification factor accuracy better than 1/1000.

Module1 alignment procedure
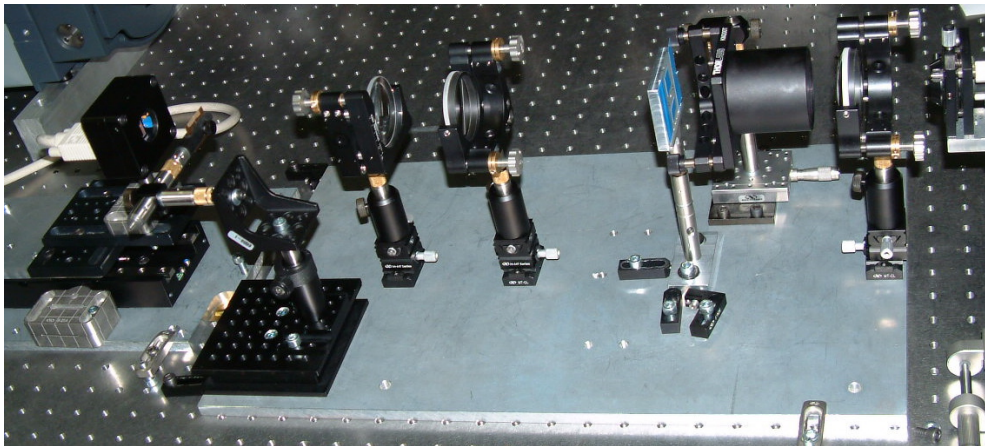
Figure 3.18: Picture of Module1 during the alignment procedure. The laboratory CCD is mounted on a (motorized) linear stage aligned to the optical axis.

As an example we explain in the following enumeration the alignment procedure of Module1 (fig. 3.18):

1. CCD positioned on the nominal Module1 output image plane. The laser spot centroids at different CCD positions along z define the

optical axis.

2. Group1-2 placed on its nominal position and aligned respect to the laser

3. Focal length measurement of Group1-2

4. Possible adjustment of Group1-2 focal length by tuning the lenses mutual distances (section 3.4)

5. Group1-2 focal plane position measurement and possible shift of the Group1-2 along z to match the Module1 output image plane with the CCD plane

6. Iteration from step 3 until within specifications

7. Group1-1 placed on its nominal position and aligned it respect to the optical axis

8. Measurement of output beam telecentricity

9. Possible Group1-1 positioning adjustment along z

10. Measurement of the beam collimation after passing through Module1

11. Possible adjustment of Group1-1 focal length by tuning the lenses mutual distances

12. Iteration from step 8 until within specifications. The Module1 is now afocal

13. Source placed on the object plane nominal position and regulated in position until the its image is focused and centered on the CCD plane

14. PS placed on its nominal position and centered respect to the optical axis

15. Measurement of the output beam telecentricity, by means of the source moved off-axis along the object plane, and possible adjustment of the PS position until within specifications

The other modules followed a similar alignment procedure. For Module 2 a flat mirror, being less fragile, substituted the DM that was mounted after after the Prototype integration.

3.5.3   Prototype final integration

The integration of the modules together formed the final Prototype set up. The Detector, the first element to be placed, defined the spots array focal
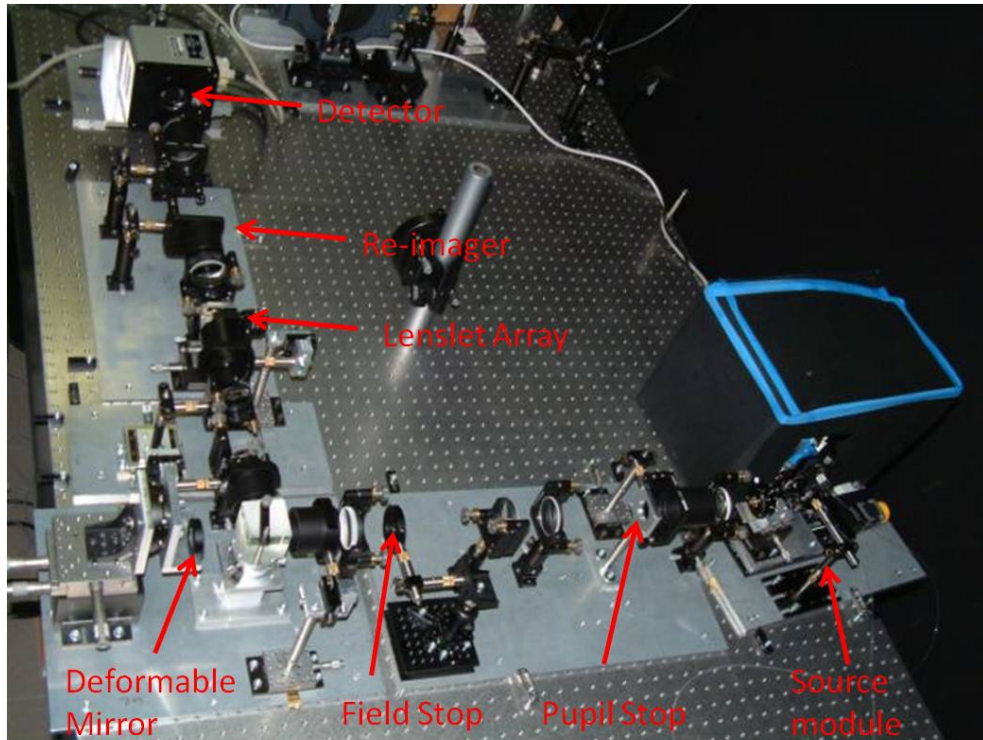
Figure 3.19: Picture of the Prototype integrated in the laboratory. In the lower-right corner of the picture the inclination of the linear stage that moves the source to give the LGS side launch effect to the spot elongation pattern on the Detector can be noticed.

plane position and the optical axis. After it the Module4 was inserted in the optical path and aligned respect to the optical axis. The incoming collimated laser beam produced a re-imaged spots array on the Detector (we remind that the LA is mounted on this module and was already properly positioned and aligned), so the Module4 was moved along z until the spots FWHM was minimized. Then the Module3 was placed on its nominal position and a point source was centered on its input object plane, seen as an infinitely distant source from the LA. The Module3 was moved along z until the measured defocus as a function of the source z-position corresponded to the expected value. The Module2 and successively Module1 positioning were carried out looking at the defocus signal coming from a mismatch of the correct modules positioning (section 3.3.7). During the alignment phase of Module2 we noticed that in the images with high SNR it was possible to distinguish a ghost image close to the spots in each sub-aperture. We were able to find the source of this ghost in the reflection of the light by the DM that passed straight to the BS

and was reflected by the optical fiber custom brass head. The light traveled again along the optical path till the Detector. We substituted the fiber head with a mat plastic one and resolved the issue.

At this point the Prototype was aligned and a symmetrical pattern of elongated spots could be imaged on the Detector. We describe now the finishing touches to add the functionalities to be exploited during the test phase.

DM alignment and slopes flattening
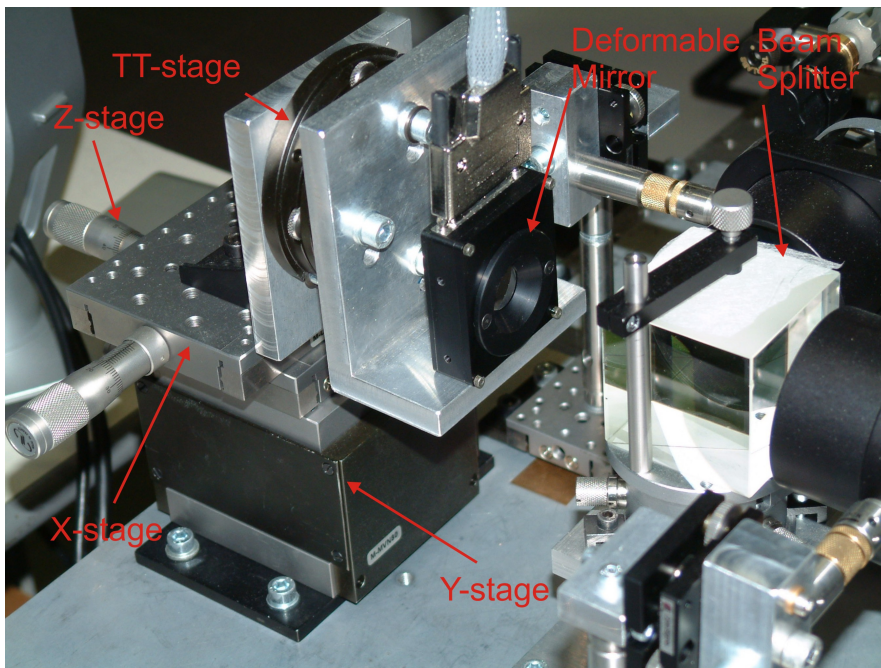
Figure 3.20: Picture of the DM mounted on Module2.

After the modules integration, on the Module2 pupil image plane the DM substituted the flat mirror mounted at its place. The DM centering respect to the optical axis was done by applying some defocus, i.e a radial deformation of the DM surface and measuring the WF variation with the SHWF. The achieved centering is considered acceptable when almost no other aberrations apart defocus were introduced by the DM in the optical path.

A modal interaction matrix was created placing the source at the NGS position and permitted to translate the DM surface shapes to Zernike modes (Noll, 1976) seen by the WFS. The slopes flattening procedure is the minimization of the WF aberrations caused by the optics by means of a proper setting of the DM shape. As discussed in section 3.3 the alignment procedures produces only

low order aberrations, so a 52 actuators DM was sufficient to correct them. We iteratively reduced the residual WF variance, during a sequence of images acquisition, by means of the slopes measurement and DM shape adjustment, until the convergence toward the flat WF was stopped since the measured WF amplitude was of the order of the measurement noise. The residual WF after this procedure resulted to be $\sim$ 30nm RMS and the corresponding DM shape became the 'zero slopes' reference shape.

Field Stop alignment
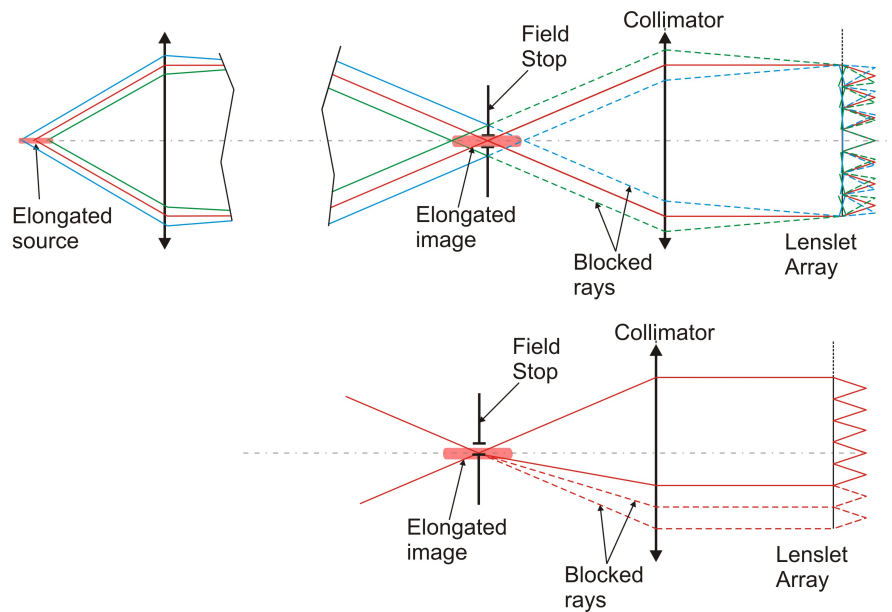
Figure 3.21: Alignment procedure for the FS; upper figure: the positioning along z while; the lower figure: centering respect to the optical axis.

During the alignment procedure of the FS, its diameter was set equal to the size of the source re-imaged on the FS plane, called δ_2 in figure 3.3. In this way the FS blocked all the rays of the elongated source but the position re-imaged at the FS plane (red rays of the upper figure 3.21). The correct position along z of the FS had to correspond to the NGS position of the source, from which the measurement of the the spots array position formed on the Detector did not produce any defocus signal.

The decentering of the FS caused instead an asymmetrical vignetting of the pupil image on the LA plane (lower figure 3.21). The FS centering procedure consisted in the achievement of a symmetrical intensity of the spots respect to

the optical axis. In figure 3.22 the comparison of the elongated images before
and after the FS aligning and regulation in diameter is shown. The elongated
source has a flat profile to better measure the spot centroid during the FS
diameter setting.
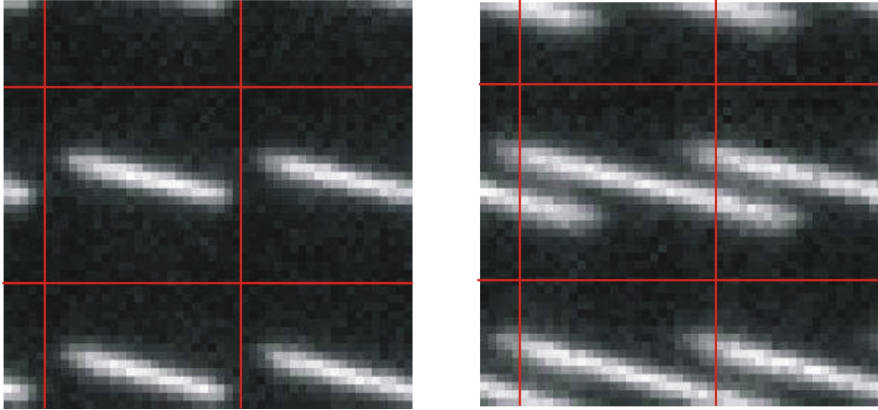
Figure 3.22: By tuning the FS aperture it is possible to remove the
contamination among adjacent sub-apertures.

Side launch configuration

The central launch configuration of the LGS was useful during the alignment
phase but for the tests phase it was foreseen to switch to the side launch scheme
in order to replicate the current MAORY baseline (section 1.2.1). This change
required the tilting of the motorized linear stage travel direction respect to the
optical axis, actually of its baseplate as it can be seen in figure 3.23. The tilt
angle had to be half of the Group1-1 FA (eq. 3.3). This procedure was carried
on iteratively. After tilting the stage baseplate, we checked in the spots array
image which sub-aperture was at the center of the radial elongation geometry,
corresponding to the LGS launcher position respect to the telescope axis. This
procedure prosecuted until the correct tilt angle was reached. Since the NGS
source position, that is the center of the elongated source, was not above the
rotation pivot, a recentering of the source had to be done after each step.
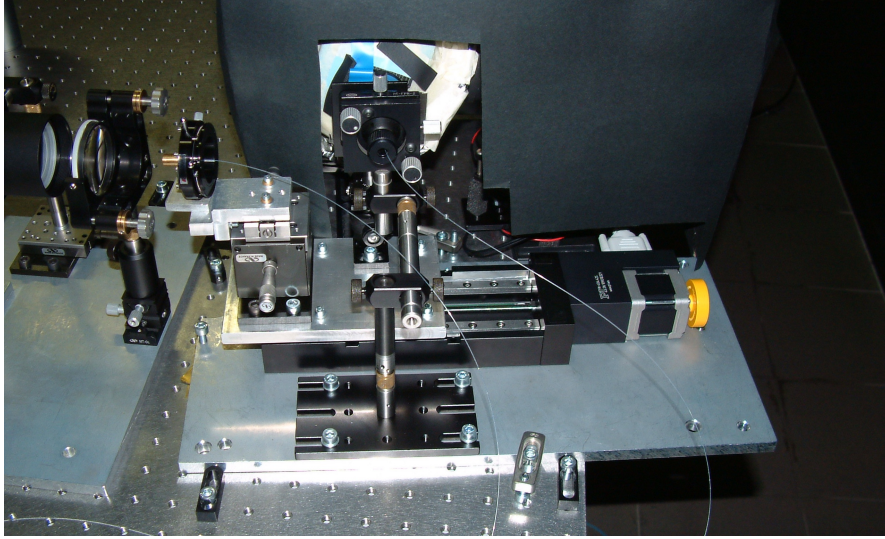
Figure 3.23: Picture of the elongated source generation part of the Prototype. The tilt of the base plate respect to the Module1 plate produces the non radial elongation pattern of the spots array on the Detector.

3.6   Data reduction and tests

3.6.1   Data Reduction

The data reduction software is modular package written in IDL. Each acquired frame is corrected for hot pixels, bias and dark current by subtracting an ambient background frame, taken by covering the PS. Each frame is also checked for bad lines and cosmic rays (figure 3.24) and the information on the bad pixels location in the image cube is stored in a specific file (a sort of 3D mask). Each frame is split up in 40×40 sub-apertures of 24×24 pixels each (12×12 in case of CCD 2x2 binning) so the data are stored as a 5-dimensional matrix ([24×24] pixels x [40×40] sub-apertures x number of frames).

The centroiding algorithms tests presented in section 3.6 make use of a template represented by the average of a set of LGS images, sub-aperture by sub-aperture. For this reason also a cube of the average sub-aperture images is stored. All the images are corrected for bad lines, by averaging the values of the two adjacent lines in the affected frame, and for cosmic rays by computing the median of the 3x3 region around the bad pixel.

Finally the procedures for the centroiding computation accepts as input the 5-dimensional matrix described above and the template image. Other information about the spot characteristics (tilt, elongation, etc.) and the RON
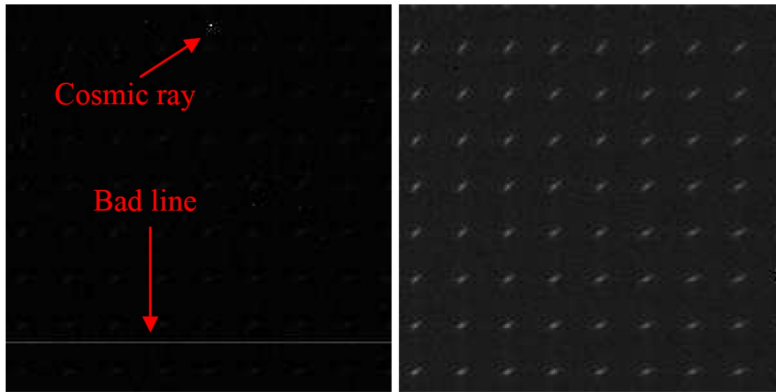
Figure 3.24: Example of a bad line and a cosmic ray correction on the same portion of the frame. The picture on the left looks dark because of the high contrast between the bad pixels and the spots in the sub-apertures.

can be passed as optional input. The spot centroids are computed in all the 40×40 illuminated sub-apertures of the Prototype pupil and their error are the RMS of the difference between the set of calculated positions in a given sub-aperture and the average position of the same sub-aperture. Data affected by bad pixels can be eventually discarded in the computations.

In figure 3.25 a Detector image snapshot shows a spots array with non radial elongation geometry and a bi-modal intensity profile of the spots. The LGS is simulated to be launched from the left edge of the primary mirror.

3.6.2   Tests

The first set of tests performed with the Prototype has been achieved in the first semester of 2010. We present in the following a brief description of the tests to demonstrate that the Prototype is able to reproduce the LGS features required in table 3.1.

The centroid algorithms considered in the tests are the WCoG (Fusco et al., 2004) and the correlation. Both algorithms require a calibration procedure to avoid effects of non linearity and non unitary gain. In addition to the numerical calibration based in the a numerical shift of the spots in the sub-aperture, the Prototype could supply a dithering calibration by means of applying TT signals to the DM. An Hybrid solution, that combined the two calibrations was also investigated.

The agreement between analysis of data produced with the LGS Prototype and simulations was tested for different scenarios related to the algorithm
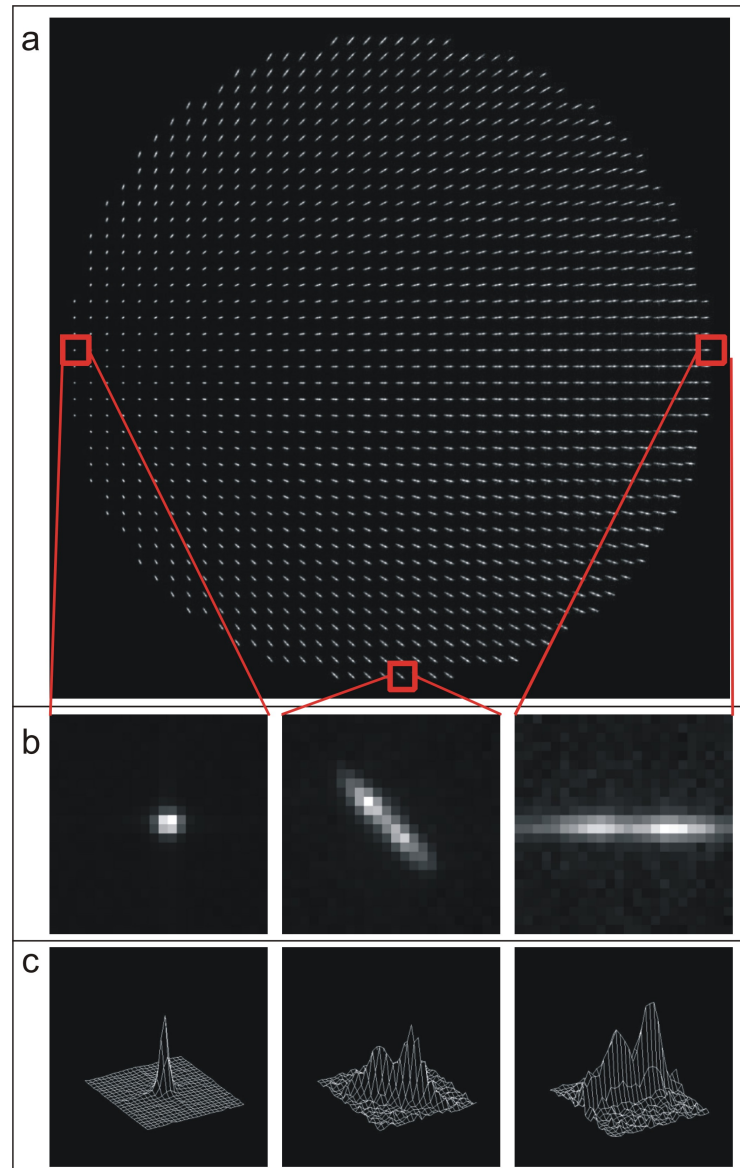
Figure 3.25: a: spot pattern on the detector with side launch configuration and bi-modal shape intensity profiles of the images; b: zoomed sub-apertures showing three different elongation directions and extent; c: 3-D representations of the images of b.

performance:

1. **Reference case** The two algorithms performance in case of 'ideal conditions' (Nyquist sampling, no spot truncation, Gaussian Sodium density profile) were measured in order to validate the results of the simulations. The measurement error was computed on 200 images in each sub-aperture. As templates the averaged

images of the elongated source, with an SNR similar to the expected one produced by averaging the instantaneous spots in 1 second of MAORY close loop, was used.

2. **Influence of truncation** The effects of truncation on the OPD Error per sub-aperture was evalutated for the two considered algorithms. Using the data from the previous test we extracted a smaller (in terms of sub-aperture FoV) sub-image of the spot in each sub-aperture.

3. **Influence of sampling** The goal was to demonstrate the feasibility of the Hybrid calibration technique described above and apply it to under-sampled LGS images. Data were taken both in Nyquist and under-sampled conditions. The measurement error was computed on the centroid measurement of 100 LGS images in each sub-aperture.

4. **Influence of profile** The goal was to demonstrate the robustness of the algorithms with an irregular intensity profile of the spots. Data were taken in under-sampled conditions (1 pixel FWHM in the non elongated axis). WCoG was performed by the dither technique. The measurement error was computed on the centroid measurement of 100 LGS images in each sub-aperture.

5. **Low order WF errors** Different intensity filters allow the prototype to emulate different Sodium density profiles. These variations in the LGS image shape are translated into non atmospheric low order aberrations (section 2.1.3), that need to be monitored by a RWFS based on NGS channel (section **??**). The objective of the Prototype in this case was mainly the validation of a set of numerical simulations, able to translate a general sodium profile in the corresponding LGS image in each sub-aperture. The next step will be to extend the analysis to the working conditions of MAORY. For this purpose the upgrade in the Prototype design by means of a variable intensity source (section 3.7.1) will permit to simulate realistic time series of sodium profiles.

A more accurate description of the tests can be found in Schreiber et al. (2010a) and Schreiber et al. (2010b).

3.7   Design upgrade

The Prototype goal is to reproduce the expected LGS features for a SHWS and compare the data with the simulations. This goal has been achieved as shown in the tests presented in section 3.6. Anyway some upgrades regarding the optics, the mechanics and some key components, to increase the Prototype functionalities and to remotely set the parameters variation, could permit to investigate in detail other LGS issues. A feasibility study of the Prototype upgrades is presented in the following and it regards the change of the intensity filter with a SLM (Upgrade 1), the simulation of multiple off axis LGSs (Upgrade 2) and, by adding a second DM, the tomographic correction of the turbulence at least for the low order modes (Upgrade 3).

We present a list of LGS features, described in chapter 2, that would be very interesting and strategic to be investigated in detail after the Prototype upgrade.

- Sodium profile temporal variation - Upgrade 1
- Low order NCPA - Upgrade 1
- Tomographic reconstruction of the turbulence - Upgrade 2
- Low order modes correction of the turbulence - Upgrade 2 and 3
- Temporal evolution of the turbulence - Upgrade 2
- Focus layer anisoplanatism - Upgrade 1 and 2
- Zenith angle effect for MCAO - Upgrade 1 and 2
- Alternative WFS concepts investigation

The last point of the above itemization regards the possibility for other WFS concepts to be investigated by means of the Prototype. In the image plane after Module2 the elongated image has all the required features of the LGS. In the current design the is not the necessary clearance to insert a folding mirror between Module2 and Module3 and thus all the modules after Module2 should be removed. In the new optical design (fig. 3.31) it would be possible to perform, one at each time, two different WFSs in the same WF sensing conditions.

3.7.1   Variable intensity source
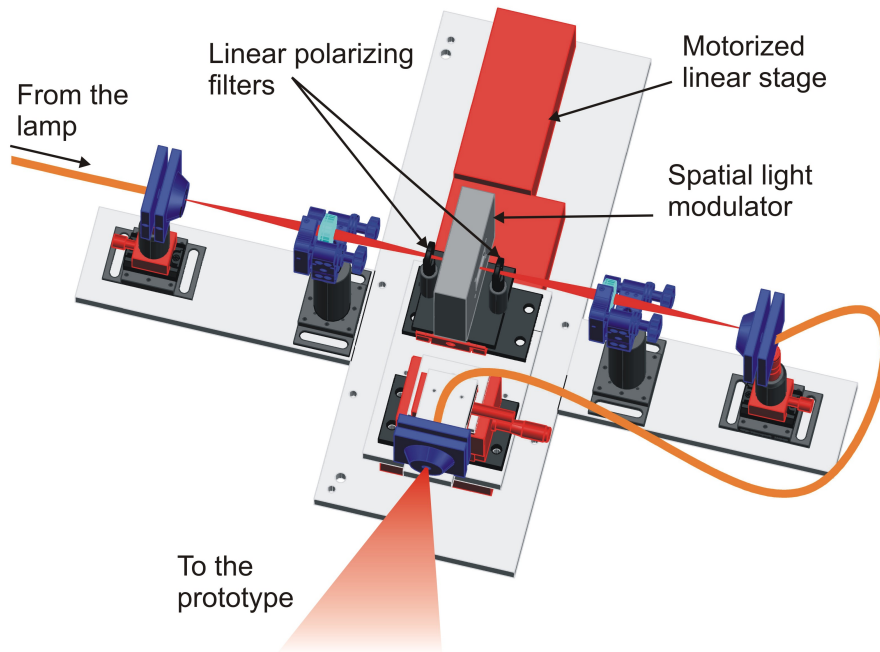
Figure 3.26: 3D design of the Prototype upgrade in the elongated source generation module where the SLM replaces the intensity filter.

In the current version of the Prototype the intensity filter that simulates the Sodium profile requires to be changed manually every time a new profile is chosen for the measurements (section 3.5.1). Of course this feature limits the possibility to deeply explore the parameter space regarding the Sodium density temporal variation (section 2.1.3), necessary to investigate the WFE related with, for example, the reference profile of the centroiding algorithms. A variable profile generation by means of the control in current or voltage of the power supply of the lamp, in addition to the necessity of a synchronization with the motorized linear stage, does not give us enough reliability: due to possible drifts of the bulb temperature a 'close loop' control of the output light intensity would be requested, complicating too much the control system. Therefore we decided to modify this part by means of a SLM, that behaves as the current version of the intensity filter but where the desired transmissivity, as a function of source position, can be programmed before any run. For a correct working two linear polarizing filters must be placed before and after the SLM (figure 3.26). A light source is re-imaged by means of a lens at the

the transmissive LCD of the SLM. At the next image plane, made by another lens, the fixed input side of the optical fiber, whose output side represents the elongated source of the Prototype, is fed by the light modulated in intensity as a function of the Prototype source position along the optical axis.

The SLM we bought has an LCD with 800x600 square pixels of 32μm side and 200:1 of contrast ratio. Using an optical fiber of 60μm core diameter, its image made by a 50mm focal length lens on the LCD plane will have a geometrical size of $\sim90\mu$m, corresponding to $\sim$3 LCD pixels. A stage travel range of about 7mm, required to produce the maximum elongated spot of 14 pixels on the Detector for the LGS side launch scheme (table 3.2) corresponds to $\sim$220 LCD pixels. This will permit to create intensity profiles of the source that reproduce sufficiently well the real ones (section 2.1.3) and the small profile perturbations to simulate its time variation for the successive acquisition.

3.7.2   Multiple LGSs and and phase screens

One of the most important upgrades of the Prototype is the simulation of multiple off-axis LGSs launched from the telescope edges, as foreseen for the EELT, and the investigation of the issues related to the tomographic reconstruction of the atmospheric turbulence with elongated sources.

In this launching scheme each LGS must form a non radial pattern of elongated spots, rotated as a function of the laser launcher position (figure 3.27). The simultaneous measurement all the LGSs of a given asterism would require an equivalent number of Detectors and it is discarded. As explained in eq. 3.3 and shown in figure 3.25, the method used by the Prototype to reproduce the LGS side launch is based on the tilting of the source movement direction respect to the optical axis. The straightforward option of rotating the source movement direction about the optical axis has been discarded too because of the opto-mechanical complexity and cost. In fact the non parallel directions of the off axis elongated sources would require the motorized linear stage to be rotated to swap among the different LGSs.

The approach that we are considering will leave unchanged the elongated source generation module (sections 3.1.1 and 3.7.1) and will move the requested modifications to the Module1 (figure 3.28). A Dove prism will be placed after the Group1-1 and, when rotated about the z-axis, it will produce an elongation pattern geometry as coming from an LGS with any azimuthal angle. Two
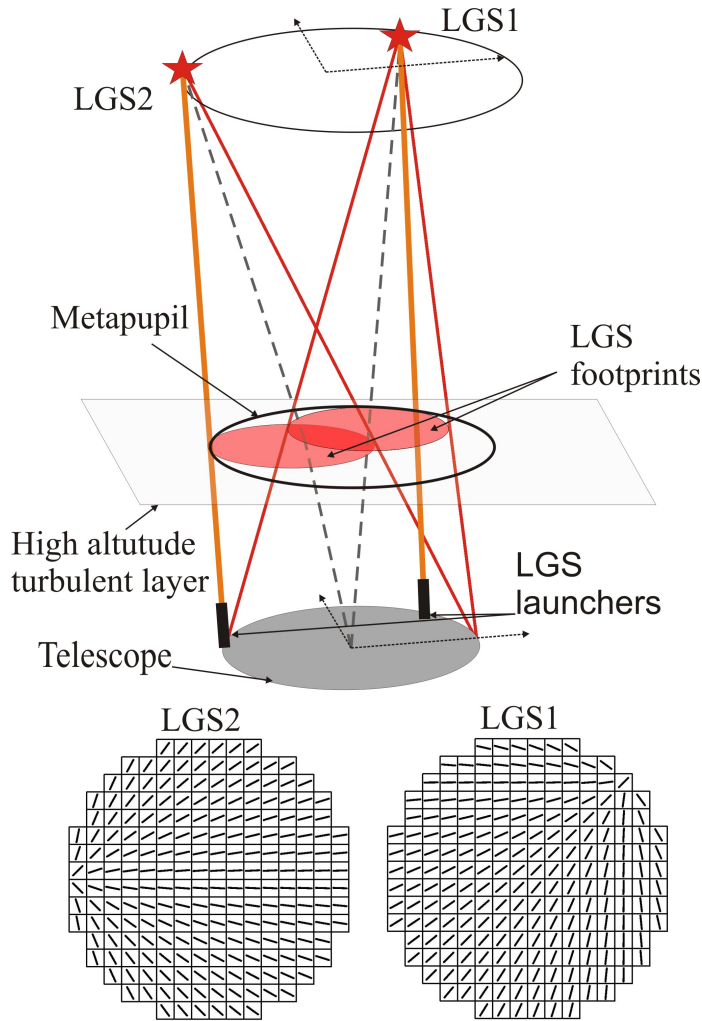
Figure 3.27: Sketch illustrating two LGSs launched from the side of the primary mirror. The two LGS footprints intersect different regions of the metapupil on a high altitude layer. The elongated spots re-imaged by the SHWSs on the Detectors are directed toward the LGS launcher.

phase screens, placed between the Dove prism and the PS, will represent two atmospheric turbulence layers, one at the ground layer and the other at a selectable high altitude layer. The footprint position of an LGS on the high altitude turbulent layer depends on the layer altitude and on the LGS zenith and azimuthal angle (fig. 3.27). A couple of motorized linear stages will move the high altitude layer screen in the x and y directions in order to make the LGS light pass through the correct footprint (figure 3.27). In this way any layer altitude and LGS launching angle can be simulated by just selecting the proper screen shift. We will not simulate the cone effect (section 2.1.2) and
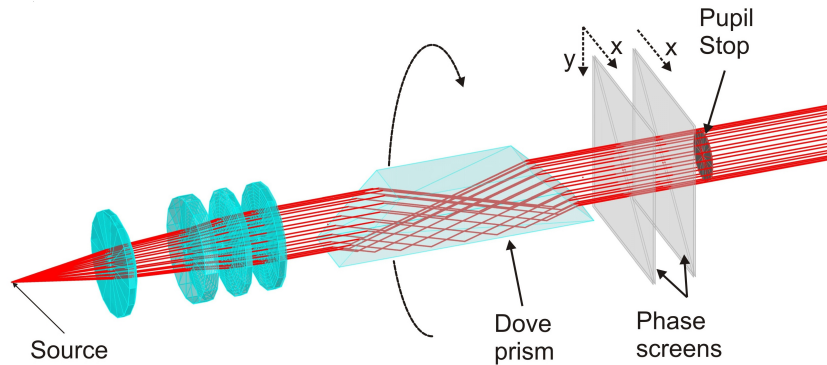
Figure 3.28: Picture showing the multiple LGSs simulation in the modified Module1. The Dove prism rotates about z to image the spots elongation pattern as coming from different off-axis sources. The phase screens are moved to make the LGS beams intersect the proper turbulence footprint.

the footprints diameter will be the same at any altitude. The position of the high layer screen along the optical axis is not an issue until the the rays ,after the screen crossing, are shifted of less than the coherence length associated to the screen (Shamir et al., 1993).

After the image acquisitions from all the LGSs of the chosen asterism, both screens can be moved to simulate the turbulence layer shift in the Taylor hypothesis of frozen turbulence, where the variations of the turbulence caused by a single layer can be modeled by a 'frozen' pattern that is transported across the aperture by the wind in that layer (Roddier, 1999).

The presence of the Dove prism and of the two phase screens requires an increase of the distance between the Group1-1 and the PS. The Group1-1 focal length is unchanged in order to not vary the source travel to form the elongation spots (eq. 3.1) so the PS is no more placed on its focal plane. This cause the loss of symmetry between the source travel and the elongated re-imaged spot elongation, similarly to the real LGSs case explained in section 2.1.3. The generation of the intensity profile will have to take count of this factor when choosing the profile of the elongated spot.

As all the refracting optics, the Dove prism introduces some aberrations to the WF on the pupil images plane, mainly astigmatism, that depend on the incoming beam collimation. The light from the source at the NGS position is collimated after passing through the Group1-1 and it is not affected by these aberrations while the WF coming from different source positions will be

aberrated after passing the prism. From the source edge positions (P1 and P3 of figure 3.2) the WF will be ∼70nm RMS at the pupil planes and, as for the case aberrations described in section 3.3.1, it can not be corrected by means of the DM.

The measured WFs from the LGS asterism will be combined to reconstruct the phase of the two screens. The reconstruction performance will be evaluated by placing the source at the NGS position and measuring the WF as coming from a point size and bright star. Moving the screens the reconstruction can be checked at any position of the field.
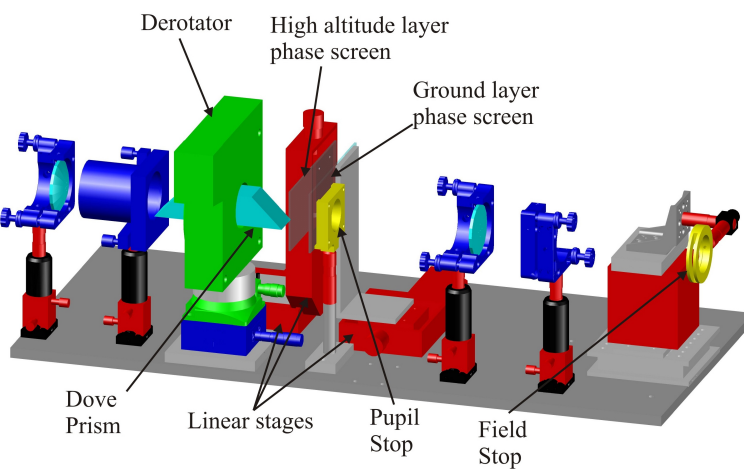
Figure 3.29: 3D view of the Module1 modification to insert the Dove prism and the moving phase screens to simulate multiple LGSs and atmospheric turbulence in two layers. The red elements are the linear stages, the blue parts the tilt states and the green ones the rotating stages.

3.7.3   MCAO

Another possible upgrade of the Prototype, that must follow the multiple LGSs simulation described in the previous section, is the MCAO configuration, achievable by means of the addition of a second DM, conjugated to the high layer phase screen. In figure 3.30 the new design of Module2 is presented. The DM conjugated to the ground layer (DM_0) is the already existing one in the current set up and it is placed with a tilt angle γ respect to the incoming beam. The two lens groups after DM_0 re-image a pupil close to which a second DM (DM_1) is placed, conjugated at the high layer screen and tilted by the same angle γ respect to the incoming beam. Finally a lenses group makes an image
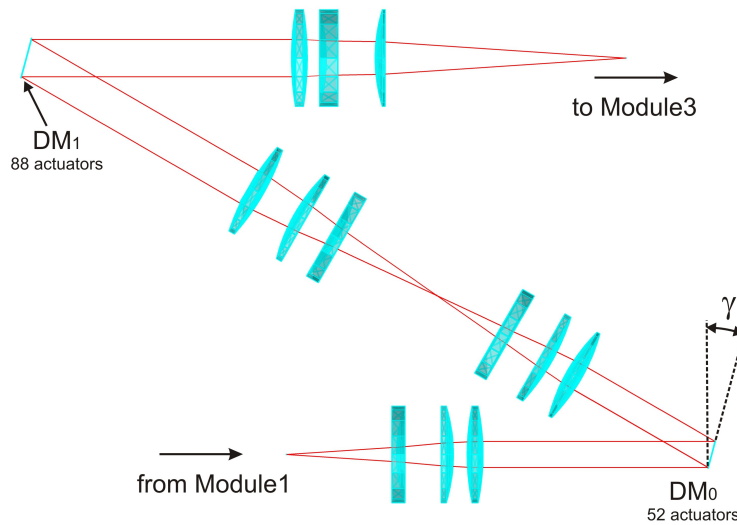
Figure 3.30: Optical design of the new Module2 with 2 DM conjugated to the phase screens.

of the source.

The tilt of the DMs respect to the optical axis ($\sim 15°$) causes the pupil images from sources at different z positions to not overlap when moving along the x-direction on the DM planes. At the edge of the mirrors the pupil omages displacement becomes 1/30 of DM pitch, considering 7 actuators over the diameter. Anyway this problem will be present, with different angles, also for MAORY post focal DMs (fig 1.7) and in the EELT M4 and M5 (EELT optical design webpage), so its effects on the WF sensing performance can be studied.

3.7.4   New optical design

We show in figure 3.31 the possible optical design of the Prototype after the upgrades presented above. Among the new features, a new faster Detector appears necessary to permit a reduction of the readout time after any acquisition, that is the bottle neck of the current version of the Prototype and thus permit a large number of acquisitions in a reasonable amount of time. Moreover we are open to investigate possible alternative concepts of WFSs, as the ones presented in section 2.3 with multiple, elongated and variable profile sources. A removable fold mirror placed between the Group2-4 and Group3 of the new optical design would not interfere with the SHWS mountings.
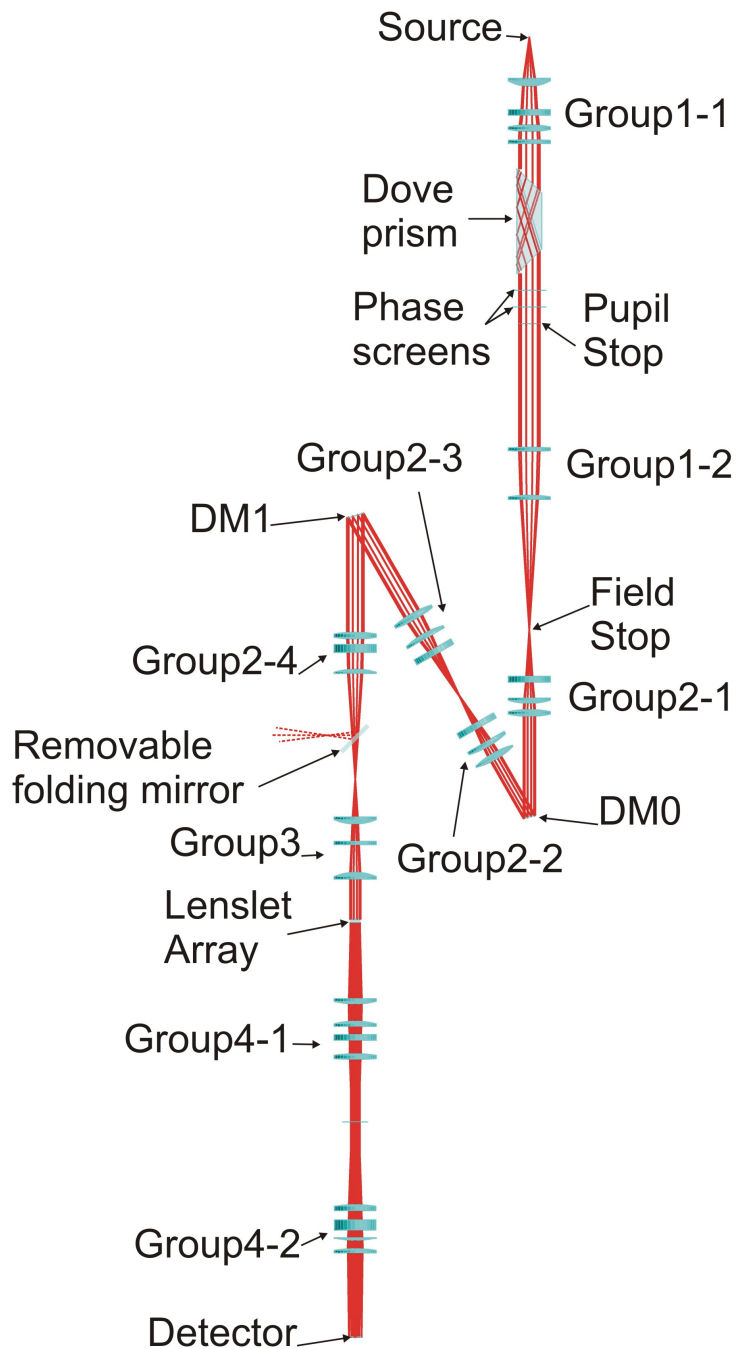
Figure 3.31: Overview of the possible Prototype upgrade. A removable folding mirror can be placed before the collimator to perform test on other WFS concepts.

Prototype prescription data					
	Surf	**Radius**	**Thick**	**Glass**	**Diam**
		mm	mm		mm
Object		Infinity	49.325		0
Group1-1	1	Infinity	9.67	BK7	50.8
	2	-51.68	28.06		50.8
	3	Infinity	2.50	BK7	50.8
	4	77.52	15.60		50.8
	5	127.811	8.09	BK7	50.8
	6	-127.811	10.00		50.8
	7	412.674	4.57	BK7	50.8
	8	-412.674	39.53		50.8
PS	STO	Infinity	149.07		25
Group1-2	10	412.674	4.57	BK7	50.8
	11	-412.674	53.03		50.8
	12	155.04	5.09	BK7	50.8
	13	Infinity	157.5668		50.8
FS	14	Infinity	62.79		
Group2-1	15	Infinity	2.50	BK7	50.8
	16	74.1911	17.06		50.8
	17	Infinity	6.17	BK7	50.8
	18	-98.288	7.00		50.8
	19	112.093	9.44	BK7	50.8
	20	112.093	35.00		50.8
BS	21	Infinity	50.80	BK7	50.8
	22	Infinity	50.02		50.8
DM	23	Infinity	-50.02	MIRROR	14
	24	Infinity	-25.4	BK7	50.8
	25	Infinity	0	MIRROR	71.6
	26	Infinity	25.4	BK7	50.8
	27	Infinity	35		50.8
Group2-2	28	112.093	9.44	BK7	50.8
	29	-112.0933	7.00		50.8
	30	98.288	6.17	BK7	50.8
	31	Infinity	17.06		50.8
	32	-74.191	2.50	BK7	50.8
	33	Infinity	62.79		50.8
Image plane	34	Infinity	45.56		
Group3	35	Infinity	8.20	BK7	50.8
	36	-64.6	22.61		50.8
	37	-258.4	2.50	BK7	50.8
	38	Infinity	33.44		50.8
	39	64.6	8.20	BK7	50.8
	40	Infinity	48.16		50.8

	Surf	Radius	Thick	Glass	Diam
		mm	mm		mm
LA	41	1.76	1.00	SILICA	12
	42	Infinity	3.16		12
LA focal plane	43	Infinity	91.79		12
Group4-1	44	Infinity	6.17	BK7	50.8
	45	-103.36	20.79		50.8
	46	103.36	6.17	BK7	50.8
	47	Infinity	10		50.8
	48	Infinity	2.5	BK7	50.8
	49	77.52	20.83		50.8
	50	179.757	6.68	BK7	50.8
	51	-179.757	75.25		50.8
	52	Infinity	100.00		0
Group4-2	53	153.805	7.22	BK7	50.8
	54	-153.805	15.00		50.8
	55	-77.52	2.50	BK7	50.8
	56	Infinity	10.00		50.8
	57	Infinity	6.17	BK7	50.8
	58	-103.36	10.90		50.8
	59	155.04	5.09	BK7	50.8
	60	Infinity	101.19		50.8
Image	61	Infinity			12.48

Table 3.8: Data editor of the Prototype current optical design.

Conclusions and future work

AO will be fundamental to achieve the science goals of the future EELT. The use of LGSs will permit to make observations with a diffraction limited angular resolution in a fraction of the sky considerably bigger respect to the case of NGSs. Anyway many issues about the WF sensing with the LGSs, especially for the Extremely Large Telescopes case, are still open.

The Prototype goal was to reproduce an extended source simulating in a realistic way an LGS and its variable intensity profile, to feed a SHWS with a number of sub-apertures of the same order of the EELT case. Its construction, described in detail in this Thesis, provided us an useful test bench for the LGS WF sensing. The first tests carried out after its integration resulted in a very good agreement with the simulations results. For this reason we are pretty confident on the reliability of the Prototype as LGS simulator and decided to increase its functionalities, by means of an automatized variation of the source intensity profile and the extension of its capabilities to the MCAO simulation. The modular design of the Prototype will permit to simplify these modifications. The feasibilities studies of the upgrades presented at the end of chapter 3 will become real parts of the Prototype hopefully soon.

In section 2.3 two alternative WFS concepts, respect to the SHWS, have been briefly presented. The aim is to investigate possible backup solutions and evaluate the technological feasibility and system complexity to achieve the required performances of the AO systems. The detailed investigation regarding the two mentioned WFSs performance with LGSs is on going. The results will be presented in two papers in preparation. The option to test them, or others WFS concepts, by means of the Prototype without dismounting the SHWS, will be made possible in the upgraded design, where a sufficient clearance to insert a removable folding mirror before the SHWS collimator is foreseen.

Dedication

Many people helped and supported me during the PhD period.

First, I give thanks to Emiliano who has been a constant source of encouragement and dedication. I appreciate especially his patience and sincerely I'm lucky to work with him.

The other guys of the -1 floor at Bologna Observatory, Italo, Laura, Giuseppe and Giovanni, deserve special note for having been always present for any question, doubt and necessity. The Prototype construction would have not been done without these talented individuals.

I thank my advisor Prof. Marano for having put trust in me and Prof. Fusi Pecci for his support.

My journey at Gemini Observatory gave me the possibility to grow my scientific knowledge, I tried to learn as much as possible from the people working there. This period has been enriched by new friends that made me feel at home. Thanks Francois, Benoit, Maxime, Vincent, Celine, Mathieu (too many French, I know), Gelis, all the day crew of the telescope and really many others.

To my mom and my brother, I feel their love even if many times I pretend I don't notice it.

I dedicate this work to Marica. His presence, more than anybody else, has shaped my life. I borrow a line for her

l'amor che move il sole e le altre stelle
Divina Commedia - Paradiso, XXXIII, 145

Bibliography

Arcidiacono, C., Lombini, M., Moretti, A., Ragazzoni, R., Farinato, J., Falomo, R., **An update of the on-sky performance of the Layer-Oriented wave-front sensor for MAD**, 2010, SPIE, 7736, 77363D

Arsenault, R., Alonso, J., Bonnet, H., Brynnel, J., Delabre, B., Donaldson, R., Dupuy, C., Fedrigo, E., Farinato, J., Hubin, N., Ivanescu, L., Kasper, M., Paufique, J., Rossi, S., Tordo, S., Stroebele, S., Lizon, J.-L., Gigan, P., Delplancke, F., Silber, A., Quattri, M., Reiss, R., **MACAO-VLTI: An Adaptive Optics system for the ESO VLT interferometer**, 2003, SPIE , 4839, 62721I

Babcock, H. W., **The possibility of compensating astronomical seeing**, 1953, PASP, 65, 229–236

Baranec, C., Bauman, B., Lloyd-Hart, M., **Concept for a laser guide beacon Shack–Hartmann wave-front sensor with dynamically steered subapertures**, 2005, OPTICS LETTERS, 30,7

Bauman B., **Optical Design for Extremely Large Telescope Adaptive Optics Systems** 2003, PhD Thesis

Beckers, J. M., **Increasing the Size of the Isoplanatic Patch with Multiconjugate Adaptive Optics**, 1988, ESO Conference on Very Large Telescopes and their Instrumentation, Vol. 2, pp. 693-703

Bello, D., Conan, J.-M., Rousset, G., **Numerical versus optical layer oriented: a comparison in terms of SNR**, 2003, SPIE, 4839

Benn, C., Abrams, D., Agocs, T., Cano, D., Gregory, T., Guerra, J., Martin, O., Morris, T., Myers, R., Rix, S., Rutten, R., Skillen, I., Skvarc, J., Tulloch, S., **GLAS/NAOMI: ground-layer AO at the**

William Herschel Telescope, 2008, SPIE, 7015, pp. 701523-701523-10

Beuzit, J.-M., Feldt, M., Dohlen, K., Mouillet, D., Puget, P., Antici, J., Baruffolo, A., Baudoz, P. and 25 co autors, **SPHERE: a 'Planet Finder' Instrument for the VLT**, 2005, The Messenger, 125

Bonaccini Calia, D., Feng, Y., Hackenberg, W., Holzlöhner, R., Taylor, L., Lewis, S., **Laser Development for Sodium Laser Guide Stars at ESO**, 2010, The Messenger, 139

Butterley, T., and Love G., **Laser Guide Star elongation mitigation study**, 2008, ELT-TRE-DUR-09400-0001

Clare, R., Ellerbroek, B., Jean-Pierre Veran,J.-P., Herriot, G., Anderson, D., **Sky coverage and tip/tilt error analysis for TMT**, 2006, SPIE, 6272, 627232-1

Clemesha, B. R., **Sporadic neutral metal layers in the mesosphere and lower thermosphere**, 1995, J. Atmos. Terr. Phys., 57,7 pp. 725-736

Conan, J.-M., Diolaiti,E., Fusco, T., Petit, C., Robert, C., Schreiber, L., Foppiani, I.,Meimon, S., Sauvage, J.-F. , **MAORY Adaptive optics system analysis and performance**, 2009, MAORY TRE-TRE-INA-528-0007-2

Costa, J., Ragazzoni, R., Ghedina, A., Carbillet, M., Vérinaud, C., Feldt, M., Esposito, S., Puga, E., Farinato, J., **Is there need of any modulation in the pyramid wavefront sensor?**, 2003, SPIE, 4839, pp. 288-298

Cuby, J.; Lidman, C.; Moutou, C.; Petr, M., **ISAAC at the VLT: one year later**, 2000, SPIE, 4008, p. 1036-1047

D'Orgeville, C., Chun, M., Sebag, J., Boyer, C., Montgomer, D., Oschmann, J., Rigaut, F., Simons, D., **Gemini Mauna Kea Laser Guide Star System**, 1999, SPIE, 3762, pp. 150-160

D'Orgeville, C., Daruich, F., Arriagada, G., Bec, M., Boccas, M., Bombino, S., Carter, C., Cavedoni, C. et al, **The Gemini South**

MCAO laser guide star facility: getting ready for first light,
2008, SPIE, 7015 70152P-1

Davies, R.; Genzel, R, **MICADO: The Multi-adaptive Optics
Imaging Camera for Deep Observations** , The Messenger, vol.
140, p. 32-33

Dicke, R., **Phase-contrast detection of telescope seeing errors and
their correction**, 1975, APJ, 198, pp. 605-615

Diolaiti, E., Ragazzoni, R., Tordi, M., **Closed loop performance of
a layer-oriented multi-conjugate adaptive optics system**, 2001,
A&A, 372, 710

Diolaiti, E., Conan, J.-M., Foppiani, I., Marchetti, E., Baruffolo, A.,
Bellazzini, M., Bregoli, G., Butler, C., Ciliegi, P., Cosentino, G.,
Delabre, B., Lombini, M., **Conceptual design and performance of
the multi-conjugate adaptive optics module for the European
Extremely Large Telescope**, 2010, SPIE, 7736, 77360R-1

Ellerbroek, B. and Rigaut, F., **Methods for correcting tilt
anisoplanatism in laser-guide-star-based multi-conjugate
adaptive optics**, 2001, JOSA, 18, 10

Esposito, S., Riccardi, A., Fini, L., Puglisi, A., Pinna, E., Xompero, M.,
Briguglio, R., Quirós-Pacheco, F., Stefanini, P., Guerra, J., Busoni, L.,
Tozzi, A., Pieralli, F., Agapito, G., Brusa-Zappellini, G., Demers, R.,
Brynnel, J., Arcidiacono, C., Salinari, P., **First light AO (FLAO)
system for LBT: final integration, acceptance test in Europe,
and preliminary on-sky commissioning results**, 2010, SPIE,
7736, pp. 773609-773609-12

Foppiani, I. and Diolaiti, E., **MAORY Sub-system error budgets**,
2009, MAORY TRE-TRE-INA-528-0005-2

Foppiani, I., Diolaiti,E., Baruffolo, A., Biliotti, V.,Bregoli, G., Cosentino,
G., Delabre, B., Lombini, M., Marchetti, E., Rossettini,P., Schreiber,
L., Tomelleri, R., Conan, J.-M., D'Odorico, S., Hubin, N., **System
overview of the Multi conjugated Adaptive Optics RelaY for
the E-ELT**, 2010, SPIE, 7736, 77362Z-1

Foy, R., Migus, A., Biraben, F., Grynberg, G., McCullough, P.R., Tallon, M., **The polychromatic artificial sodium star:A new concept for correcting for the atmospheric tilt**, 1995, A&AS, 111, pp 569-578;

Foy, R. and Labeyrie, A., **Feasibility of adaptive telescope with laser probe**, 1985, A&A, 152, 129;

Fried, D., **Statistics of geometric representation of wavefront distortion**, 1965, JOSA, 55, 1427;

Fugate, R. Q.,Fried, D. L., Ameer, G. A., Boeke, B. R., Browne, S. L., Roberts, P. H., Ruane, R. E., Tyler G. A., Wopat L. M., **Measurement of atmospheric wavefront distortion using scattered light from a laser guide-star**, 1991, Nature, 353, 144;

Fusco, T-, Conan, J.-M., Michau, V., Mugnier,L. M., Rousset, G., **Efficient phase estimation for large-field-of-view adaptive optics** , 1999, OPTICS LETTERS, 24, 21

Fusco, T., Nicolle, M., Rousset, G., Michau, V., Beuzit, J.-L., Mouillet, D., **Optimization of a Shack-Hartmann-based wavefront sensor for XAO systems**, 2004, SPIE, 5490, pp.1155-1166

Fusco, T.; Blanc, A.; Nicolle, M.; Beuzit, J.-L.; Michau, V.; Rousset, G.; Hubin, N., **Sky coverage estimation for multiconjugate adaptive optics systems: strategies and results**, 2006, MNRAS, 370, 174-184;

Ghez, A., Hornstein, S., Lu, J., Bouchez, A., Le Mignant, D., Van Dam, M, Wizinowich, P., Matthews, K., Morris, M., Becklin, E., Campbell, R., Chin, J., Hartman, S., Johansson, E., Lafon, R., Stomski, P., Summers D., T**he first Laser Guide Star Adaptive Optics observations of the Galactic Center: SGR A's infrared color and the extended red emission on its vicinity**, 2005, APJ, 635, 1087–1094

Gilmozzi, R., Monnet, G., Robinson, M., **FP7 E-ELT Preparation – Grant Agreement Funded by the European Commission is Underway**, 2008, The Messenger, 132

Gilmozzi, R. and Spyromilio, J., **The 42m European ELT: status**, 2008, SPIE, 7012, 701219

Gonzales, J., D'Odorico, S., **E-ELT interfaces for scientific instruments**, 2009, E-TRE-ESO-586-0252 Issue2

Happer, W., MacDonald, G., Max, C., Dyson, F., **Atmospheric-turbulence compensation by resonant optical backscattering from the sodium layer in the upper atmosphere**, 1994, JOSA, 11, 1

Hardy J. W., **Adaptive optics for astronomical telescopes**, 1998, Oxford University Press

Herriot, G.,Hickson, P., Ellerbroek, B., Véran, J.-P., Shed, C., Clare, R., Loozee, D., **Focus errors from tracking sodium layer altitude variations with laser guide star adaptive optics for the Thirty Meter Telescope**, 2006, SPIE, 6272

Herriot, G., Andersen, D., Atwood, J., Boyer, C., Beauvillier, A., Byrnes, P., Conan, R.; Ellerbroek, B., Fitzsimmons, J.; Gilles, L., Hickson, P., Hill, A.; Jackson, K., Lardière, O., Pazder, J., Pfrommer, T., Reshetov, V., Roberts, S., Véran, J.-P., Wang, L., Wevers, I., **NFIRAOS: TMT's facility adaptive optics system** 2010, SPIE, 7736, pp. 77360B-77360B-8

Hugot, E., Madec, F., Vives, S., Ferrari, M., Le Mignant, D.,; Cuby, J., **Toward high-dynamic active mirrors for LGS refocusing systems**, 2010, SPIE, 7739, pp. 773939

Ito, M., Hayano, Y., Saito, Y., Takami, H., Iye, M., Hattori, M., Oya, S., Watanabe, M., Akagawa, K., Colley, S. A., Golota, T. I., Guyon, O., **The characteristics of laser-transmission and guide star's brightness for Subaru LGS/AO188 system**, 2010, SPIE, 7736, pp. 773651-773651-7

Kolb, J., and Downing, M., **ELT Visible adaptive optics WFS Detector - Technical specifications**, 2008, ELT-SPE-ESO-09200-00005-3

Lombini, M., Schreiber, L., Foppiani, I., Diolaiti, E., **Optical solution to spot elongation in laser guide stars wavefront sensors**, in preparation

Malacara, D., **Optical Shop Testing**, 1978, Wiley Series in Pure and Applied Optics, John Wiley and Sons

Marchetti, E., B., Delabre, B., Donaldson, R., Fedrigo, E., Frank, C.,; Hubin, N., Kolb, J., Lizon, J.-L., Marchesi, M., Oberti, S., Reiss, R., Soenke, C., Tordo, S., Baruffolo, A.,; Bagnara, P., Amorim, A., L., **MAD on sky results in star oriented mode**, 2008, SPIE, 7015, pp. 70150F-70150F-1

Mazzoleni, R., Yaitskova, N., Noethe, L., **Disentangling between low order telescope aberrations and segmentation errors using a Shack-Hartmann sensor**, 2010, SPIE, 7012, 70123A

Neichel, B., Rigaut,F. ,Bec, M., Boccas, M., Daruich, F., D'Orgeville, C., Fesqueta, V., Galveza, R., Garcia-Rissmanna, A., Gausachsa, G., Lombini, M., Perez, G., Trancho, G., Upadhyaa, V., Vucina, T., **The Gemini MCAO System GeMS:nearing the end of a lab-story**, 2010, SPIE, 7736, 773606-1

Noll, R., **Zernike polynomials and atmospheric turbulence**, 1976, JOSA, 66, 207

Oberti, S., and Kolb, J., **EELT AO design inputs: relevant atmospheric parameters**, 2008, E-SPE-ESO-276-0206-Issue1

Orban de Xivry, G., Rabien, S., Barl, L., Esposito, S., Gaessler, W., Hart, M., Deysenroth, M., Gemperlein, H., Strüder, L., Ziegleder, J., **Wide field AO correction: the Large Wavefront Sensor Detector of ARGOS**, 2010, SPIE, 7736, pp. 77365C-77365C-10

Origlia, L.; Oliva, E.; Maiolino, R.; Gustafsson, B.; Piskunov, N.; Kochucov, O.; Vanzi, L.; Minniti, D.; Zoccali, M.; Hatzes, A.; Guenther, E., **SIMPLE: a high-resolution near-infrared spectrometer for the E-ELT**, 2010, SPIE, 7735, pp. 77352B-77352B-9

O'Sullivan,C., Redfern, R., Ageorges, N., Holstenberg, H.-C., Hackenberg, W., Ott, T., Rabien,S., Davies, R., Eckart, A., **Short timescale variability of the mesospheric sodium layer**, 2000, Experimental Astronomy, 10, 147

Pfrommer, T., Hickson, P., She, C.-Y., **A large-aperture sodium fluorescence lidar with very high resolution for mesopause dynamics and adaptive optics studies** 2009, Geophysical Research letters, 36, L15831

Ragazzoni, R., Farinato, J., and Marchetti, E., **Adaptive optics for 100-m-class telescopes: new challenges require new solutions**, 2000, SPIE, 4007, pp. 1076-1087

Ragazzoni, R. , **Pupil plane wavefront sensing with an oscillating prism**, 1996, J. Mod. Opt., 43, 289.

Ragazzoni, R., Marchetti, E., Valente, G., **Adaptive-optics corrections available for the whole sky**, 200, Nature, 403, 6765, pp. 54-56

Ragazzoni, R., Almomany, Y., Arcidiacono, C., Falomo, R., Farinato, J., Gullieuszik, M., Diolaiti, E., Lombini, M., Moretti, A., Piotto, G., Marchetti, E., Donaldson, R., Turolla, R., **Layer oriented: science with MAD and beyond**, 2008, SPIE, 7015, pp. 70150I-70150I-7

Riccardi, A., Bindi, N., Ragazzoni, R., Esposito, S., and Stefanini, P., **Laboratory characterization of a Foucault-like wavefront sensor for adaptive optics**, 1998, SPIE, 3353, pp. 941-951

Rigaut, F., Neichel, B., Bec, M., Boccas, M., Garcia-Rissmann, A., Gratadour, D., **Sample of GeMS Calibrations and Control Schemes**, 2010, 1st AO4ELT Conf., 08001

Rigaut, F., Ellerbroek, B., and Flicker, R., **Principles, limitations, and performance of multiconjugate adaptive optics**, 2000, SPIE, 4007, p. 1022

Rigaut, F., and Gendron E., **Tilt anisoplanatism and PSF retrieval in LGS MCAO using a predictive controller**, 1992, A&A, 261, pp.677-684

Robert, C., Conan, J.-M., Gratadour, D., Schreiber, L., Fusco, T., **Tomographic wavefront error using multi-LGS constellation sensed with Shack–Hartmann wavefront sensors**, 2010, JOSA A, 27, 11, pp. A201-A215

Robin, A., Reyle, C., Derriere, S., Picaud, S., **A synthetic view on structure and evolution of the Milky Way**, 2003, A&A, 409, pp.523-540

Roddier, F., 1999, in **Adaptive optics in astronomy**, Cambridge University Press

Rousset, G., 1999, in **Adaptive optics in astronomy**, Cambridge University Press

Sandler, D. and Sthal, S., **Adaptive optics for diffraction-limited infrared imaging with 8-m telescopes**, 1994, JOSA, 11, 2

Sawruck, N., Lee, I., Jalali, M., **System overview of 30w and 55w sodium guide stargazer systems**, 2010, SPIE, 7736, pp. 77361Y-77361Y-8

Shack, R. and Platt, B., **Production and Use of a Lenticular Hartmann Screen**, 1971, JOSA, 61, 656

Schreiber, L., Diolaiti, E., Foppiani, I., **MAORY Risk assessment**, 2009, MAORY TRE-TRE-INA-528-0002-2

Schreiber, L., Foppiani, I., Diolaiti, E.,Robert, C, Conan, J.-M., Lombini, M., **Laser guide stars for extremely large telescopes: efficient Shack–Hartmann wavefront sensor design using the weighted centre-of-gravity algorithm**, 2009, MNRAS, 396, 1513;

Schreiber, L., Lombini, M., Diolaiti, E., Robert, C, Foppiani, I., Cosentino, G., Bregoli, G. **MAORY Test report of the LGS WFS prototype**, 2010, 1513, EFP7-TRE-INA-09500-0004-1

Schreiber, L., Lombini, M., Diolaiti, E., Robert, C, Foppiani, I., Cosentino, G., Bregoli, G., Marchetti, E., **The Laser Guide Stars Wavefront Sensor prototype for the E-ELT: test results**, 2010, SPIE, 7736, 77365B-1

Schreiber, L., Diolaiti, E., Foppiani, I., Lombini, M., et al., **Calibration of SHWS response by dithered under-sampled LGS images**, in preparation

Schreiber, L., Diolaiti, E., Foppiani, I., Lombini, M., et al., **Performance simulations of the Pyramid WFS with LGS on 8 to 40m class telescopes**, in preparation

Shamir, J., Crove, D., Beletic, J., **Improved compensation of atmospheric turbulence effects by multiple adaptive mirror systems**, 1993, Applied Optics, 32, 24

Simakov, N., Hamilton, M., Veitch, P.,Jesper Munch, J., **A pulsed guide star laser can be the brightest**, 2010, SPIE, 7736, pp. 77364Z-1

Simard, L., Crampton, D., Ellerbroek, B., Boyer, C., **The TMT instrumentation program**, 2010, SPIE, 7735, pp. 773523-773523-12

Smith, W., **Modern Optical Engineering**, 2000, McGraw-Hill, third Edition

Strehl, K., **Uber Luftschlieren und Zonenfehler**, 1902, Zeitschrift fur Intrumentenkunde, 22, 214.

Tatarski, V. I., **Wave Propagation in a Turbulent Atmosphere**, 1961, Dover, New York

Thomas, C., **A simple turbulence simulator for adaptive optics** 2004, SPIE, 5490;

Thomas, S., Fusco, T., Tokovinin, A., Nicolle, M., Michau, V., Rousset, G., **Comparison of centroid computation algorithms in a Shack–Hartmann sensor**, 2006, MNRAS, 371, pp. 323–336

Thompson, L., Teare, S., Xiong, Y., Castle, R., Chakraborty, A.; Gruendl, R.; Leach, R., **UnISIS: Laser Guide Star and Natural Guide Star Adaptive Optics System**, 2009, PASP, 121, pp. 498–511

Vernet, E., Jochum, L., La Penna, P., Hubin, N., Muradore, R., Casalta, J., Kjelberg, I., Sinquin, J.-C., **The field stabilization and adaptive optics mirrors for the European Extremely Large Telescope** 2008, SPIE, 7015, 70150S-2

Wizinowich, P., Le Mignant, D., Bouchez, A., Campbell, R., Chin, J., Contos, A., van Dam, M., Hartman, S., Johansson, E., Lafon, R., Lewis, H., Stomski, P., Summers, D., Brown, C., Danforth, P., Max, C.;, Pennington, D. , **The W. M. Keck Observatory Laser Guide Star Adaptive Optics System: Overview**, 2006, PASP, 118, pp. 297-309

EELT Science cases - ESO web site
http://www.eso.org/sci/facilities/eelt/science/doc/eelt_sciencecase.pdf

Paranal Observatory seeing data - ESO web site
http://www.eso.org/gen-fac/pubs/astclim/paranal/seeing/

Sky background data - ESO web site
http://www.eso.org/sci/facilities/eelt/science/drm/tech_data/background/

EELT optical design - ESO web site
http://www.eso.org/sci/facilities/eelt/telescope/design/

LGS MCAO sky coverage - Gemini Observatory web site
http://www.gemini.edu/sciops/instruments/?q=node/10120